The Anisotropy of the Surface Energy and Photochemical Activity of Rutile

Jennifer B. Lowekamp
Department of Materials Science and Engineering
Carnegie Mellon University
Pittsburgh, PA 15213-3890

February 8, 1999

Advisor: Professor Gregory S. Rohrer

Submitted to Carnegie Institute of Technology in partial
fulfillment of the requirements for the degree of

Doctor of Philosophy
in
Materials Science and Engineering

Abstract

The relationship between the surface structure and photochemical activity of rutile was studied using atomic force microscopy (AFM) and electron backscattered diffraction (EBSD). Two types of specimens were used: sintered polycrystals, which provided a wide range of orientations, and thin films of low-index orientations, which provided macroscopically homogeneous samples. The amount of silver photoreduced by each crystallite surface from an aqueous $AgNO_3$ solution was used as a quantitative measure of relative reactivity. Because the neutral silver deposited on the surfaces as islands, the relative photochemical activity could be determined by direct microscopic observation. In all, more than 200 orientations were examined. The results obtained from the polycrystals were consistent with those obtained from the limited number of high-purity, low-index thin films.

The identification of facets on thermally etched surfaces of randomly oriented rutile crystallites enabled us to create orientation stability figures for two temperatures—1273 K and 1473 K. Assuming that local equilibrium was reached at the intersections between the low-index and complex facets, relative surface energies were calculated using the orientation stability figures. The results indicate that {011} is the most stable orientation at both temperatures. The relative energies of the remaining facets at 1273 K are $\tilde{a}_{\{110\}}/\gamma_{\{011\}} = 1.05 \pm 0.05$, $\gamma_{\{010\}}/\gamma_{\{011\}} = 1.09 \pm 0.03$, and $\gamma_{\{001\}}/\gamma_{\{011\}} = 1.13 \pm 0.02$. Based on these data, a qualitative equilibrium shape and its temperature dependence is described. The stable shape of rutile is not fully faceted at 1273 K or 1473 K, but more rutile orientations are unstable with respect to faceting at 1273 K than at 1473 K. For example, the range of orientations near {001} that are stable with respect of faceting is diminished at the lower temperature, and based on the faceted surfaces of the {001} oriented thin film specimens, this orientation is no longer part of the equilibrium shape at 998 K.

By correlating the orientation stability figures with the orientation dependence of the photocatalytic activity, it was concluded that the reduction of silver depends on the presence of {011} facets and not on anisotropic bulk processes. The amount of silver reduced on surfaces partially composed of {011} facets is much greater than the amount of silver reduced by other surfaces, implying that the photocatalytic activity of {011} rutile is high. Other possibilities for the large amount of silver on the crystallites with {011} facets, including preferential diffusion of neutral silver atoms to {011} facets and epitaxy between the {011} rutile surface and silver, were examined and discarded. The results from the photoreduction experiments on {001} oriented thin films, which have surfaces terminated by nanometer-scale {011} facets, suggest that the active sites for at least one of the photochemical reaction are on the intersections between {011} facets.

Acknowledgements

I would first like to thank my advisor, Greg Rohrer, for the opportunity to conduct this research. I would also like to thank my committee, Pat Morris Hotsenpiller, Brent Adams, and Paul Salvador, for their time and effort. I would especially like to thank Pat for the rutile thin films used in this thesis and for allowing me to spend two weeks using their facilities at DuPont for the silver photoreduction experiments. The financial support of the NSF and DuPont is also gratefully acknowledged, as well as the support of the staff and faculty in the MSE department.

I would also like to thank friends and colleagues in MSE for their help and support through the years. I am grateful for the help of Dave Saylor and Rich Smith in the synthesizing of ceramic polycrystals. I would also like to thank Bassem El-Dasher and Richard Wu for the help with the OIM. In addition, I would like to thank Jennifer Giocondi and Amy Bayer for listening when I needed someone to talk to.

I would like to thank my family for their love, support, and encouragement throughout my entire life. My mother and father have been a constant source of inspiration for me, and my grandmother has heaped more praise on me than any one person deserves.

Finally, I would like to thank my husband, Bruce, for his endless supply of love and encouragement. I would also like to acknowledge his help with writing the Java program I used to analyze facet orientations. Bruce, I couldn't have done it without you.

Table of Contents

Table of Figures

Table of Tables

Chapter 1

Introduction

1.1 Experimental Motivation

As environmental laws become more stringent, industry has become increasingly interested in cost-effective methods for removing toxic chemicals from waste streams. Current methods, such as incineration, chlorination, and activated carbon adsorption, are expensive, involve toxic chemicals themselves, or simply transfer toxins from one form to another. At least one state, California, has banned one popular method of waste purification, air stripping [1]. Many research groups have attempted to show that semiconductors can meet the need for reliable, cost-effective water and air purification by harnessing the sun's energy and acting as photocatalysts. Titania in one of two forms, anatase or rutile, is the most highly researched oxide photocatalyst because it is inexpensive, plentiful, and stable in almost all environments, forms few toxic intermediates, completely mineralizes almost all toxins, and is capable of using sunlight as an energy source and oxygen as an oxidant [2]. However, the oxidation or reduction of many toxins by TiO_2 is slow, and designing a reactor that allows for the separation of the catalyst from solution while maintaining a high surface area has been difficult. Because systematic structure/property relations for these materials have yet to be established, there are few guiding principles that can be applied to the selection or optimization of improved materials.

Several years ago, our collaborators at DuPont discovered that the photochemical properties of rutile are anisotropic [3]. This finding was based on experiments conducted on thin film samples with low-index orientations. In this thesis, the photochemical activity of rutile is determined for all possible orientations. The principal motivation for this work is the idea that knowledge of the relationship between surface structure and photocatalytic activity will allow optimum catalyst microstructures to be developed.

1.2 Experimental Objective

The objective of this thesis is to define the orientation dependence of the photochemical activity of rutile and to identify the surface with the highest reactivity. To meet this objective, several pieces of information were needed. First, an orientation stability figure was developed so that the facets present on any given orientation could be specified. Second, because we anticipated a relationship between the surface energy and photochemical activity, the relative surface energies of the stable facets were determined. Third, the photochemical activity was determined as a function of orientation. Finally, and most importantly, the observations of the facet structure and energy were combined with the photochemical reactivity so that specific structural features associated with high reactivity could be unambiguously identified.

1.3 Experimental Approach

Most photocatalytic studies are conducted using powders in order to approximate the conditions of practical importance. However, from such experiments, it is not possible to gain information about specific surfaces. In this study, both polycrystalline rutile formed by sintering and single crystal thin films of known orientation act as photocatalysts so that the surfaces used during the reaction are reproducible and well characterized.

The orientations of individual crystallites in the ceramic specimen are first determined using electron backscattered diffraction (EBSD). The distribution of characteristic microstructural features, such as facets, are then determined by atomic force microscopy (AFM). From the EBSD results and AFM images, the orientations of the facets on the surface are determined. These data are then compiled to form the orientation stability figure and to determine the relative energies of the stable surfaces.

The well-characterized surfaces are then used to photocatalytically reduce silver ions to silver metal, which deposits on the surfaces as islands. The number and distribution of silver islands are measured using AFM and used to determine the extent of the reaction and the relative photocatalytic activity of each surface. The data are analyzed by correlating the number of silver deposits with the orientations of the stable facets on the surface. The unique aspect of this method is that rather than examining a small number of low-index, single crystal surfaces, we compare the behavior of several hundred surfaces, spanning the range of possible orientations.

1.4 References

[1] N. Serpone, *Sol. Energy Mat. and Sol. Cells* **38** (1995) 369.
[2] N. Serpone, R. Terzian, C. Minero, and E. Pelizzetti *in* "Photosensitive Metal-Organic Systems: Mechanistic Principles and Applications", (C. Kutal and N. Serpone, Eds.), p281, American Chemical Society, Washington, D. C. (1993).
[3] P. Morris Hotsenpiller, W. Farneth and J. Bolt, private communication.

Chapter 2

Background

2.1 Photocatalysis

2.1.1 Ideal Photocatalytic Reactions

Heterogeneous photocatalysis occurs when a semiconductor, in the presence of light with energy greater than its bandgap, increases the rate and/or extent to which a chemical reaction occurs without being fundamentally changed by the reaction. Photons penetrate the surface of the semiconductor, are adsorbed, and raise electrons from the valence band to the conduction band (see Figure 2.1). As the electron and hole migrate to the surface, they can recombine, releasing heat or light, or become trapped at defect centers deep within the crystallite. If the hole and electron reach the surface, they can transfer across the bonds between the surface and molecules adsorbed to the surface, oxidizing or reducing the adsorbates, respectively [1], or they can be trapped [2]. Since recombination frequently occurs in a semiconductor with no adsorbates on the surface in a time-scale on the order of nanoseconds, it is important that adsorbates already exist on the surface at the time of the excitation or that other traps exist to prevent the holes and electrons from recombining [2].

In an ideal heterogeneous catalytic reaction, the catalyst is unaltered after the process is complete, the reaction is thermodynamically favorable and is only accelerated by the catalyst, the electrons and holes generated by the catalyst are needed in the reaction, and the reaction produces products which are different from those products produced in the presence of light without the catalyst [3]. TiO_2 is considered a nearly ideal heterogeneous photocatalyst; oxidation of hydrocarbons over TiO_2 produces only CO_2, H_2O, and mineral acids as final products [3].

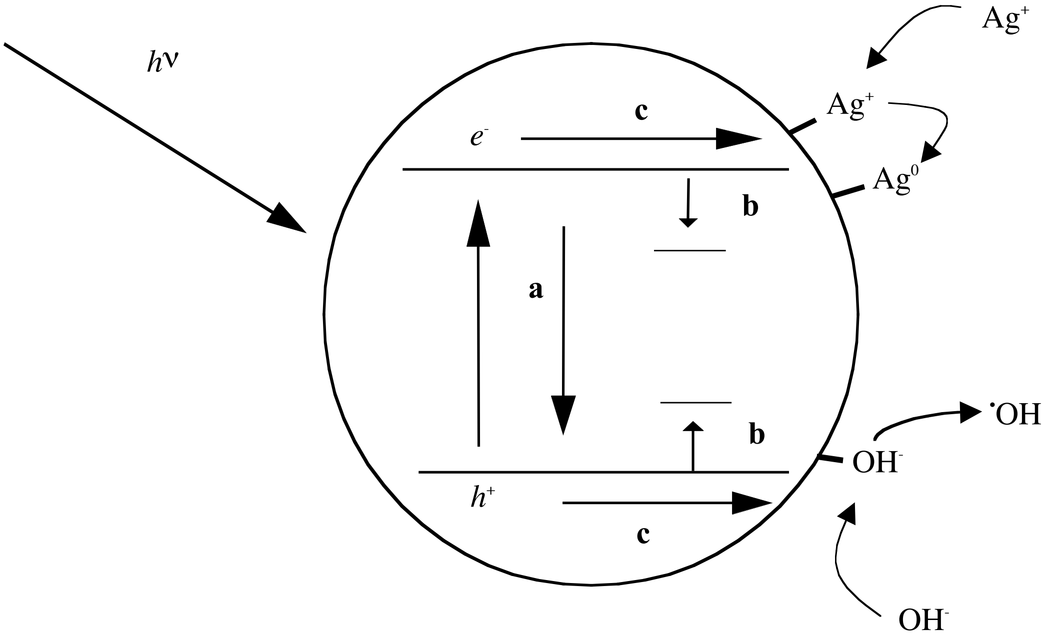

Figure 2.1—A schematic description of photocatalysis. After the excitation of the electron to the conduction band,
a) the electron and hole can recombine;
b) the electron and/or hole can become trapped in the crystallite;
c) the hole and/or electron can participate in oxidation/reduction reactions on the surface.

Although toxic by-products are sometimes produced in the short-term, they are eventually completely oxidized [4].

One possible mechanism for the photochemical oxidation of hydrocarbons involves free radicals produced on the surface of TiO_2 from water and O_2 [5–12]. The first step in the oxidation cycle is the adsorption of hydroxyl ions onto Ti^{4+} sites on the TiO_2 surface. A photogenerated hole can react with the hydroxyl ion to produce a hydroxyl radical which may desorb (Eq. 2.1).

$$h^+ + OH^-_{ads} \xrightarrow{TiO_2} {}^{\bullet}OH \tag{2.1}$$

A photogenerated electron can also reduce a surface Ti^{4+} to Ti^{3+}. Oxygen molecules in the atmosphere or dissolved in the water then adsorb onto the Ti^{3+} site. The electron is transferred from the Ti^{3+} site to the oxygen molecule. In high pH conditions, the charged oxygen molecule desorbs. In low pH conditions, the charged oxygen molecule can react with H^+ in the water to form a perhydroxyl radical, ${}^{\bullet}HO_2$ (Eq. 2.2) [3].

$$O^{-}_{2,ads} + H^{+} \xrightarrow{TiO_2} {}^{\bullet}OH_{2,ads} \tag{2.2}$$

The perhydroxyl radical then desorbs. Hydroxyl ions in the water adsorb to the now empty Ti^{4+} site to complete the reaction cycle. The perhydroxyl radicals and hydroxyl radicals produced on the TiO_2 surface are thought to be the active agents which oxidize hydrocarbons.

Other models propose that the oxidation and reduction reactions can occur on the surface of TiO_2 itself and not just through intermediaries such as hydroxyl and perhydroxyl radicals, especially when the concentration of organic material is high enough that adsorption of the organic molecules to the surface becomes competitive with the adsorption of water [12–14]. The mechanism is similar to that described above, except that the hole is localized on an oxygen ion adjacent to the hydroxyl group. Organic molecules then adsorb onto oxygen ions with the localized holes and, ideally, are eventually oxidized until only CO_2 and H_2O remain.

In this study, the reaction used to quantify the photochemical reactivity is the reduction of silver ions to silver metal on a rutile surface instead of the oxidation of hydrocarbons, leading to the following governing relations:

$$Ag^{+}_{ads} + e^{-} \xrightarrow{TiO_2} Ag^{0}_{ads} \tag{2.3}$$

$$H_2O_{ads} + h^{+} \xrightarrow{TiO_2} {}^{\bullet}OH + H^{+} \tag{2.4}$$

For each electron that is promoted to the conduction band, reaches the surface, and participates in the reduction reaction (Eq. 2.3), an atom of silver is produced which remains adsorbed onto the surface. The oxidation reaction (Eq. 2.4) must occur at the same rate as the reduction reaction in order to maintain charge neutrality in the rutile crystallite. Once a critical nucleus size is reached, the silver acts as an electron trap and facilitates the reduction reaction [15, 16]. For this reason, it is safe to assume that after neutral, solid silver is present on the surface, the oxidation reaction is rate limiting.

2.1.2 Measuring Photocatalytic Activity

Heterogeneous photocatalytic activity is measured in several different ways, none of which are ideal [17]. The most common method of gauging activity is the quantum yield, or the number of catalytic reactions per photon of light absorbed. Because it is difficult to measure the exact amount of light absorbed by the catalyst, the common assumption is that all of the light is absorbed. In these cases, the measure of activity is called the apparent quantum yield. This assumption is patently false in almost all cases since powder suspensions inevitably scatter most of the light entering them. The theoretical maximum ratio of photons that can be absorbed by TiO_2 is no more that about 65% [18]. Apparent quantum yield values for most reactions over TiO_2 are low due to scattering and high electron-hole recombination rates. Although apparent quantum yields as high as 30% have been measured for the oxidation of formic acid over a TiO_2 thin film [19], typical values range from 0.5% to 3%, depending on the reactant [20].

Another method for reporting photocatalytic activity is the turnover number, which is defined as the number of product molecules formed per active site on the catalyst [17]. The turnover number must be greater than one for the reaction to be catalytic. However, it is very difficult to accurately determine the number of active sites on a heterogeneous catalyst, especially since the number of active sites changes as photons are absorbed. Therefore, in most cases, total or specific surface area is substituted for the number of active sites. In other cases, the surface density of hydroxyl groups is used as the number of active sites. Similar methods of reporting activity are the turnover rate, which is the number of product molecules formed per active site per second, and the turnover frequency, which is the number of product molecules formed per second. However, these methods suffer from the same difficulties as the turnover number. The turnover number for TiO_2 is high [3], and in most studies, the number cannot be measured because the TiO_2 photocatalyst maintains a steady-state activity for as long as the experiment is run. Turnover frequencies are easily measured because there is no need to know the number of active sites. Turnover rates between 10^{13} m^{-2} s^{-1} and 10^{16} m^{-2} s^{-1} have been measured for a variety of forms of titania [4]. The smaller turnover rates were measured for amorphous titania, while crystalline anatase and rutile had turnover rates between 10^{15} m^{-2} s^{-1} and 10^{16} m^{-2} s^{-1}. Turnover frequencies of 10^{17} s^{-1} [21] and 10^{18} s^{-1} [19] have been measured for TiO_2, but turnover frequencies cannot be used to compare the activities of different photocatalysts because differences in surface area and/or numbers of active sites are not taken into account.

The work in this thesis used two methods for measuring photoactivity. Because the amount of light absorbed by the rutile thin films could be accurately measured, quantum yield was used to measure the photoactivity of thin film samples. The amount of light absorbed by the rutile polycrystals was not so easily measured, so relative turnover numbers were used as the measure of photoactivity. In this case, it is assumed that the surface area of each crystallite is proportional to the number of active sites.

2.2 Structure of TiO_2

2.2.1 Bulk

Figure 2.2 shows the crystal structure of both anatase and rutile, the two commonly available polymorphs of TiO_2. (See Table 2.1 for unit cell information.) Although the structures of these polymorphs appear very different, their building blocks, distorted TiO_6 octahedra, are similar [22–24]. In rutile, the distortion in the bonds is small; the Ti-O bonds in rutile along the [110] or $[1\bar{1}0]$ directions are approximately 2% longer than the other four bonds [25]. Although the distortions in the octahedra are

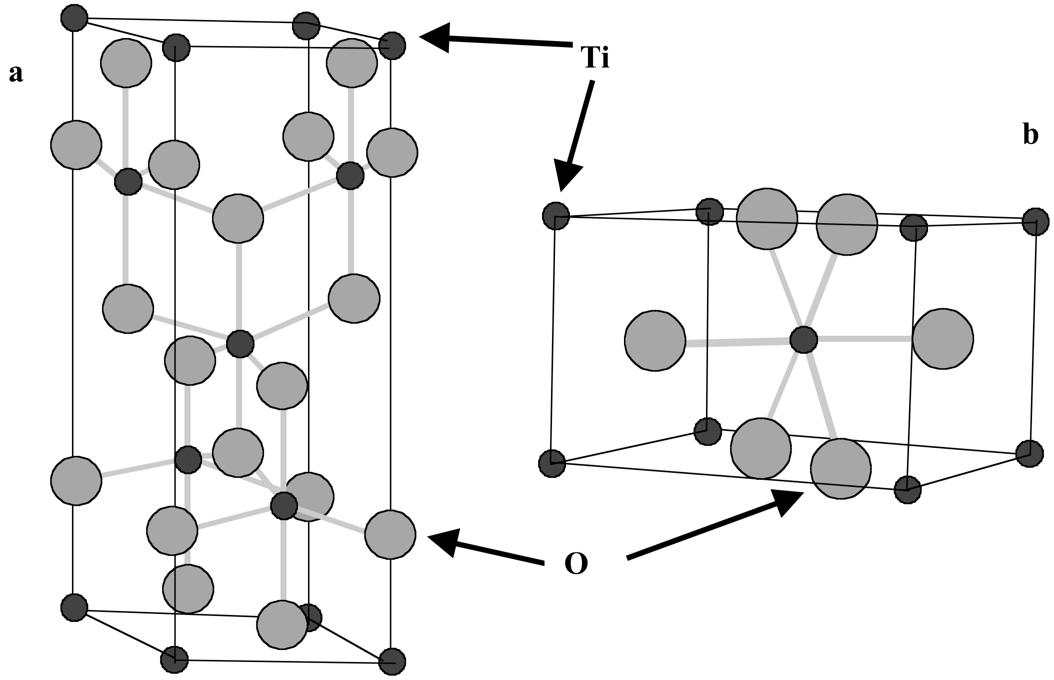

Figure 2.2—The crystal structures of a) anatase and b) rutile.

Table 2.1: Cell Dimensions and Atomic Positions for Rutile and Anatase

	a (Å)	**c (Å)**	**Space Group**	**Cell Contents**	**Atomic Positions**
rutile	4.594	2.958	P4$_2$/mnm (no.136)	2 formula units	Ti: 0,0,0 ½, ½, ½ O: 0.3, 0.3, 0 0.7, 0.7, 0 0.2, 0.8, ½ 0.8, 0.2, ½
anatase	3.785	9.514	I4$_1$/amd (no.141)	4 formula units	Ti: 0,0,0 (+ I) 0, ½, ¼ O: 0, 0, 0.2 0, 0, 0.8 0, ½, 0.45 0, ½, 0.05

greater in anatase than in rutile, it is mainly the pattern in which the octahedra are connected that differentiates the two polymorphs [23] (see Figure 2.3). In rutile, each octahedron is connected to ten other octahedra: two by edges and eight by corners. The chains of edge-sharing octahedra lie along the [001], and adjacent octahedra on different chains share corners [25]. In anatase, each octahedron is connected to eight other octahedra: four by edges and four by corners. Because of these similarities, anatase thin films have electronic structures that are similar to rutile [26].

One of the most commonly studied TiO_2 photocatalysts, Degussa P25, is comprised of amorphous material, anatase, and rutile. X-ray results from work by Bickley et al. [27] seem to indicate that there is approximately four times as much anatase as rutile in Degussa P25. However, diffuse reflectance measurements from this same group seem to indicate that the amounts of anatase and rutile are approximately equal. This contradiction may occur because the amorphous phase and the areas joining the different phases have optical properties similar to that of rutile. TEM studies have shown that a mixture of different particle types exists in Degussa P25. Some particles are mainly amorphous, others are composed of anatase covered with a thin layer of rutile, and still others are pure anatase or pure rutile [27]. While the real powdered photocatalyst is clearly a complex assembly of phases, this thesis concentrates on rutile.

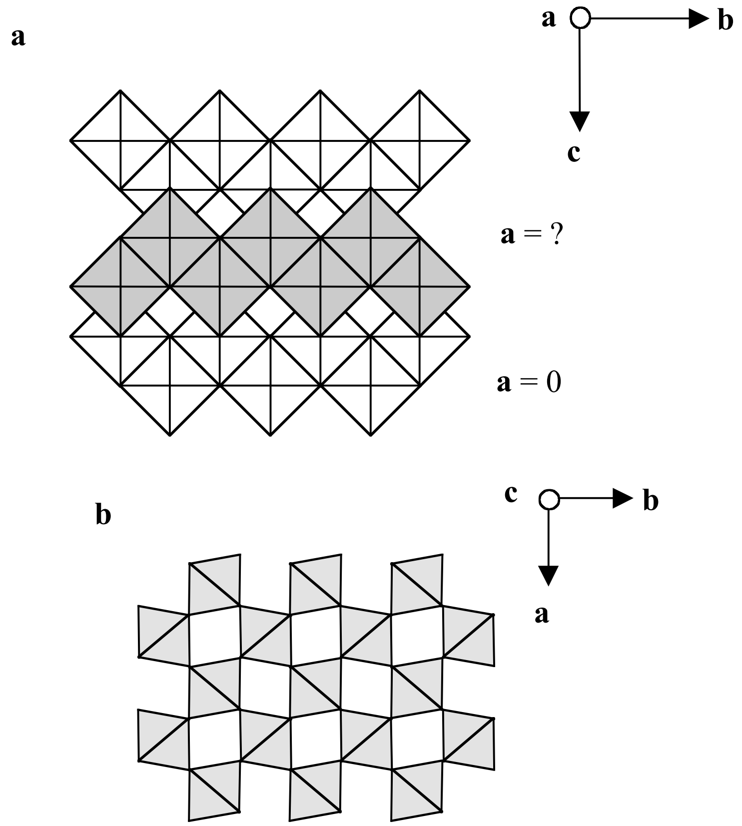

Figure 2.3—The idealized polyhedral representation of a) anatase and b) rutile.

2.2.2 Rutile Surface Studies

2.2.2.1 {110} Surface

The {110} surface, shown in Figure 2.4, is the most extensively studied of rutile's low-index planes. The {110} surface has the smallest density of dangling bonds of all the low-index planes; one-half of the titanium cations on this surface are five-fold coordinate, while the others are six-fold coordinate. This surface is observed to be stable against faceting and is frequently observed on growth forms. Both two-fold and three-fold coordinate oxygen atoms exist on the {110} surface [25]. The ideal {110} surface is not atomically flat because of rows of bridging oxygen ions that protrude from the surface [28]. The electronic structure of nearly perfect {110} TiO_2 surfaces is essentially

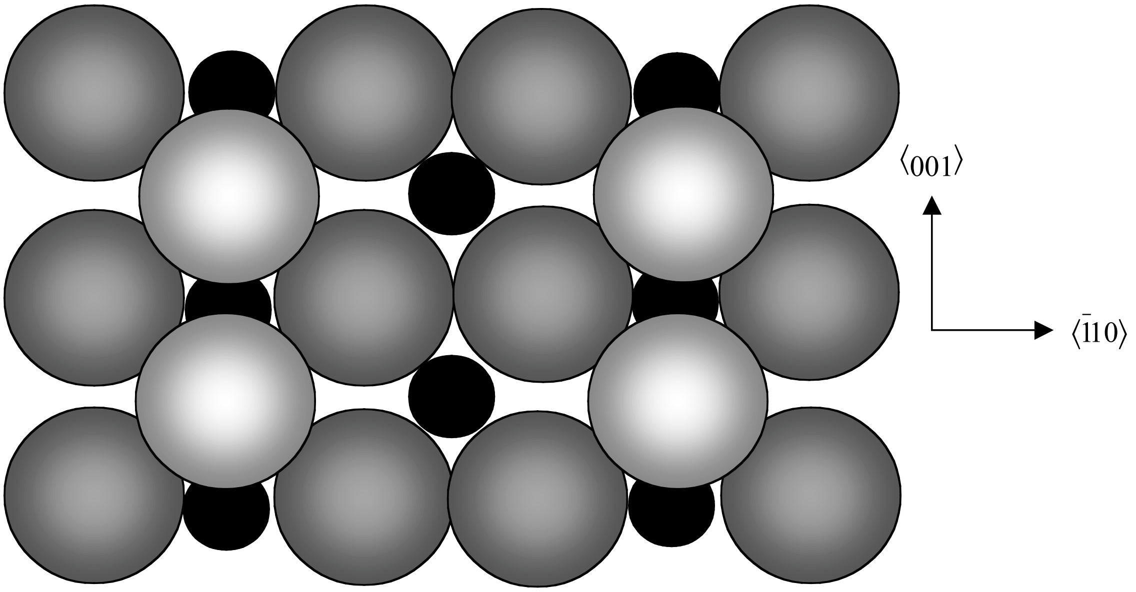

Figure 2.4—The surface ions of the {110} plane of rutile. The small ions are Ti while the larger ones are O. The lighter O ions are bridging O. The final coordinating oxygen for each Ti is not shown.

the same as the electronic structure of bulk rutile [29, 30], and full bulk bandgaps are retained [31].

Numerous ultra-high vacuum (UHV) studies have been completed on the atomic-scale structure of the {110} surface [25, 32–37]. In general, the results confirm the model presented in Figure 2.4 for the fully oxidized surface. However, because most of the results were obtained from reduced or non-stoichiometric surfaces, their applicability to fully oxidized surfaces in the ambient is questionable.

2.2.2.2 {010} Surface

The {010} rutile surface, shown in Figure 2.5, is also stable and does not facet upon heating to 1473 K [38]. The ideal {010} surface is not atomically flat [28] and is more corrugated that the {110} surface [25]. All titanium cations in the {010} surface are five-fold coordinate, and all oxygen anions are two-fold coordinate. The electronic structure of the {010} surface is not substantially different from the bulk [31].

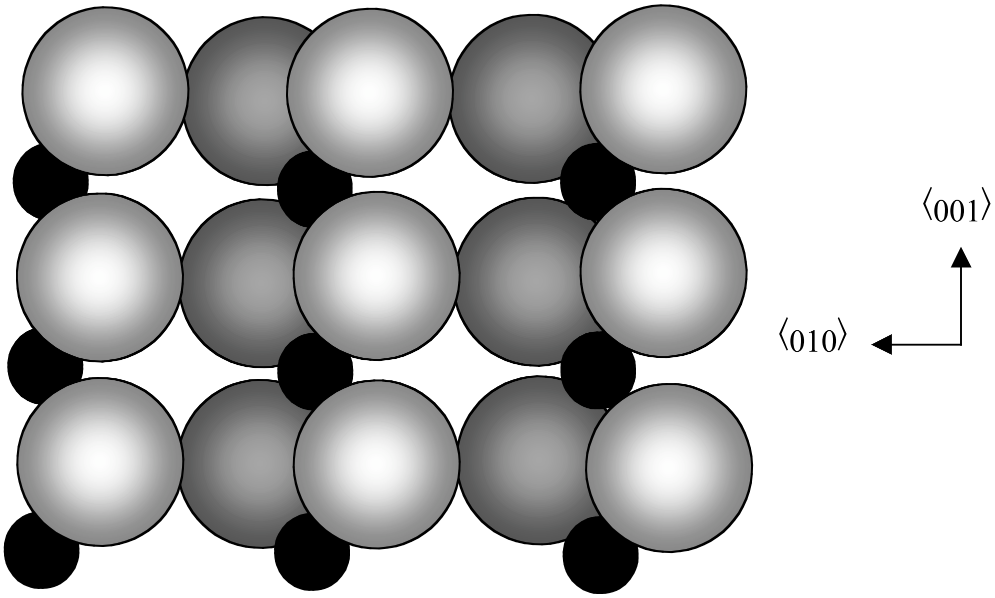

Figure 2.5—The surface ions of the {010} plane of rutile. The lighter O ions are slightly above the Ti plane, while the darker O ions are slightly below it. The fifth O ion coordinating the Ti is not shown.

Like the {110} surface, the {010} surface has been the subject of numerous UHV studies [29, 38–42], whose main results seem to indicate that the surface reconstructs due to O_2 loss when reduced. This reconstruction has been characterized as a microfaceting of the surface into {110} planes [42], indicating that the {010} may not be stable in all conditions. Again, care has been taken to ensure that the specimens used in the current study are fully oxidized, so the results obtained from reduced specimens should be applied with caution.

2.2.2.3 {001} Surface

The {001} rutile surface, shown in Figure 2.6, is the least stable of the low-index planes and facets in vacuum at temperatures from 773 K to above 1400 K [43–47]. Titanium cations on an unreconstructed {001} surface have only four nearest neighbors compared to the bulk value of six [25, 28], and oxygen anions are two-fold coordinate [25]. As expected by the low coordination of the ions on the unreconstructed {001}

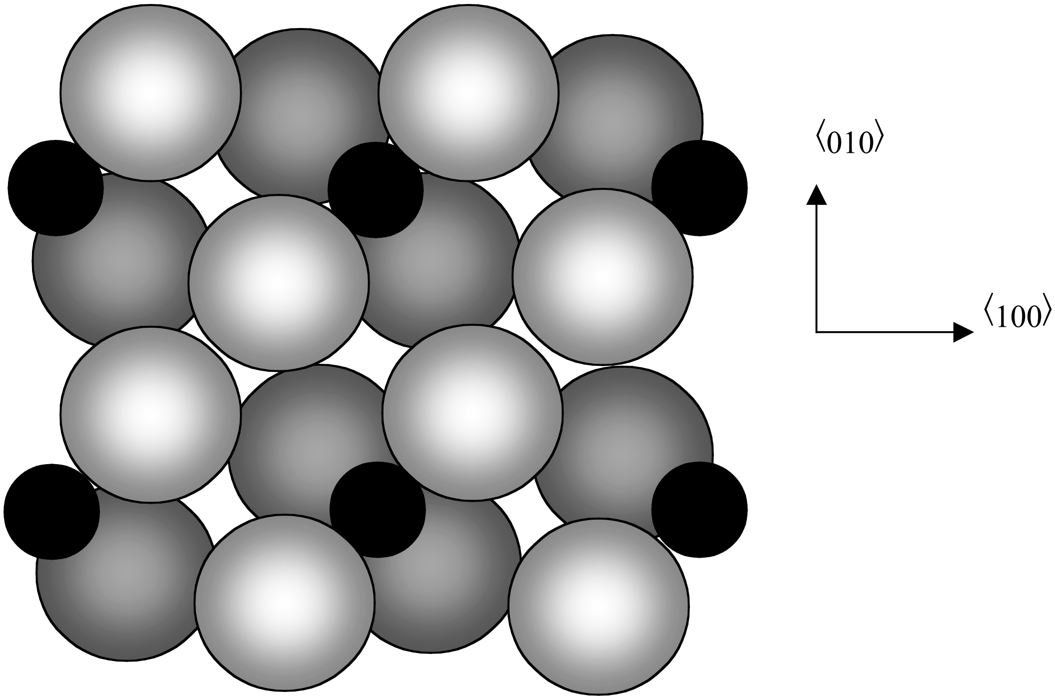

Figure 2.6—The surface ions of the {001} plane of rutile. The darker O ions are below the surface plane.

rutile surface, the surface is less stable than {100} or {110}. The unrelaxed {001} surface is very flat [25], and full bulk bandgaps are retained [31].

Although (1×1) surfaces have been produced in vacuum, they are not stable and facet at relatively low temperatures. Firment [43] observed that {001} surfaces facet into {011} planes when annealed in vacuum at temperatures less than 1300 K and into {114} planes when annealed in vacuum at temperatures greater than 1300 K. Wang et al. [47] also examined {001} rutile surfaces after they had been annealed at 1698 K in oxygen for 36 hours and determined that the surface was actually faceted into {124} planes instead of {114} planes. Using scanning tunneling microscopy (STM), Poirier et al. [44] determined that the predominant facet on {001} rutile annealed at 783 K is {011}. His group also found that {023}, {045}, {114}, {111}, and small {001} facets are present on {001} rutile as well.

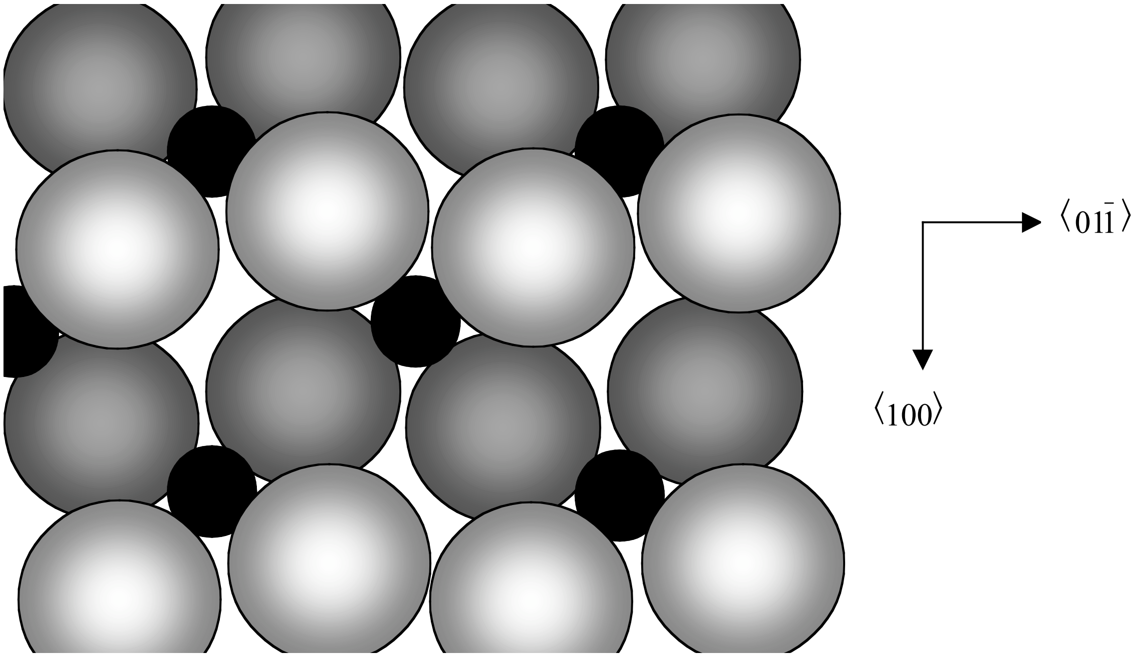

Figure 2.7—The surface ions of the {011} plane of rutile. Lighter O ions are slightly above the Ti plane, while darker O ions are slightly below the Ti plane. The fifth O ion coordinating the Ti is not shown.

2.2.2.4 {011} Surface

There have been no studies that closely examined the {011} TiO_2 rutile surface, shown in Figure 2.7. Theoretical calculations predict that the ideal {011} surface is more corrugated than the {110} surface [25]. The unit cell is centered rectangular, with unit cell axis along the $\langle 100\rangle$ and $\langle 01\bar{1}\rangle$. All titanium cations are five-fold coordinate, and oxygen anions are either two- or three-fold coordinate.

Studies on a reduced {011} rutile SnO_2 surface determined that the surface unit cell remained p(1x1) up to 573 K [48], indicating that it is stable with respect to faceting. Because rutile TiO_2 is isostructural to rutile SnO_2, this result is probably also indicative of the stability of the {011} TiO_2 surface as well.

2.3 Crystal Shape of TiO_2

Of the four low-index surfaces {110}, {010}, {011}, and {001}, theoretical calculations predict that the {110} has the lowest surface energy, followed by the {010}, the {011}, and the {001} [25]. The {110} surface is also the predominant facet in rutile samples of geological origin, although both {011} and {010} facets are also observed [28], with the surface area of the {110} facets being approximately three times the area of either the {011} or the {010} facets [49–51].

In 1994, Ramamoorthy et al. [25] used *ab initio* methods to calculate the surface energies listed in Table 2.2. Their results predicted relative surface energies that were consistent with experimental observation [49–51]. Based on these energies, they predicted the equilibrium crystal shape at 0 K shown in Figure 2.8. The form shown in Figure 2.8 is based on the assumption that the Wulff shape is composed of only {110}, {010}, {011}, and {001} facets. When only a small number of facets appear, the equilibrium shape can be determined by the following relationship [52]:

$$\frac{l_A}{l_B} = \frac{\gamma_A}{\gamma_B} \tag{2.5}$$

where l_A is the length of the radius from the center of the shape to the surface of facet A, l_B is the length of the radius from the center of the shape to the surface of facet B, γ_A is the surface energy of facet A, and γ_B is the surface area of facet B. In other words, the lower the surface energy of a facet, the closer the facet is to the center of the crystal and the greater the surface area of the facet. If the energy of a facet is too great, the length between it and the center of the crystal at its closest point is greater than the size of the crystal in that direction, and the facet does not appear in the Wulff shape. If the energy of

Table 2.2: Surface Energy vs. Orientation for Stoichiometric Rutile at 0 K [25]

Surface	Surface Ti Coordination	Surface O Coordination	Surface Energy (unrelaxed) J/m^2	Surface Energy (relaxed) J/m^2
{110}	5,6	2,3	1.751	0.889
{010}	5	2	1.928	1.118
{011}	5	2,3	2.104	1.392
{001}	4	2	2.931	1.648

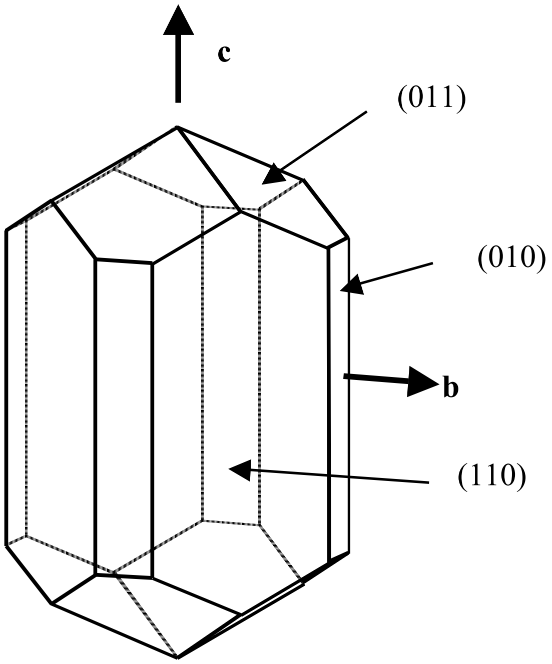

Figure 2.8—A schematic showing the equilibrium facet structure of rutile as proposed by Ramamoorthy et al. [25].

the facet is very small, the length between it and the center of the crystal is very small at its closest point. If there is a deep cusp in the surface energy around this facet, the area of the facet will be large in the Wulff construction. This occurs because even though the distance between the low-energy facet and the center of the crystal increases as the overall surface orientation moves away from the orientation of the facet, it still remains smaller than the distance between the higher-energy facets on either side and the center of the crystal at their closest points, creating missing orientations in the Wulff form. This implies that a surface with a general orientation may facet, or increase its total surface area, to decrease the total surface energy per area. Therefore, the Wulff construction provides a way to relate surface structure, i.e., the facets present on the surface, to surface orientation and energy.

As shown in the construction in Figure 2.8, the {001} facet was not predicted to appear in an equilibrated structure at 0 K, which supports recent experimental results conducted at higher temperatures in vacuum [43, 44, 47]. Some of the same experimental results predict that the {111} plane should also be stable at relatively low

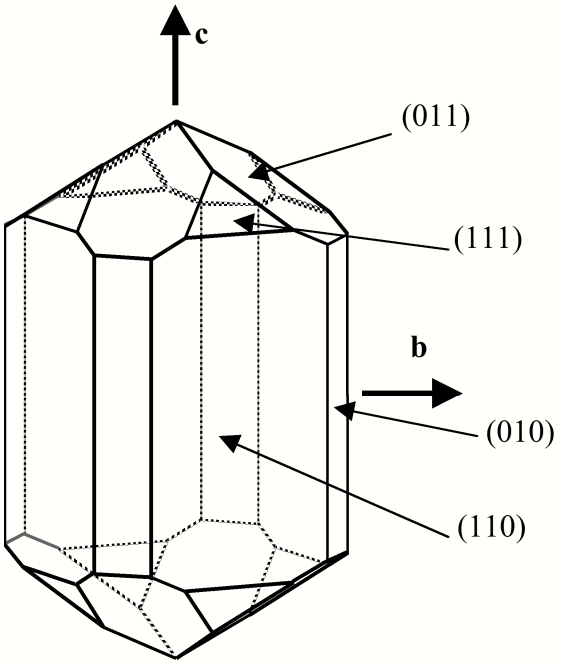

Figure 2.9—A schematic showing the proposed equilibrium facet structure of rutile at 0 K if {111} is considered stable.

temperatures [44], and Figure 2.9 shows a possible equilibrium shape for rutile at 0 K assuming that the {111} plane is stable.

2.4 Facet Structure of a Randomly Oriented Surface

The interpretation of the experiments described in this thesis depend on knowing the facet structure for any randomly oriented surface at relevant temperatures. If it were assumed that the construction shown in Figure 2.9 accurately represented the facet structure at temperatures between 1273 K and 1473 K, it could be used to identify the facets present on thermally etched surfaces. Table 2.3 lists the angles between all relevant planes in the first octant, and Figure 2.10 shows the angles between the various planes present on the equilibrium crystal. These angles could be compared to experimental values and used to help identify the faceting on randomly oriented grains.

Table 2.3: Relationships between Low-Index Planes

Planes	Angle	Line of Intersection
(110), (101)	157.5°	$[1\bar{1}\bar{1}]$
(110), (111)	137.7°	$[1\bar{1}0]$
(110), (100)	135.0°	[001]
(101), (011)	135.0°	$[\bar{1}\bar{1}1]$
(101), (111)	118.4°	$[\bar{1}01]$
(101), (100)	147.2°	[010]
(101), $(\bar{1}01)$	155.6°	$[0\bar{1}0]$

However, at the temperature increases, entropy plays an increasingly important role in determining the stability of surfaces and leads to a roughening of the Wulff shape. At higher temperatures, the Wulff shape will likely include some rounded corners and edges, together with facets of singular orientation. Figure 2.11 shows an example of a two-dimensional Wulff shape with rounded corners, singular facets, and missing orientations. The singular facets appear as flat areas in the Wulff shape, and the missing orientations appear as sharp changes in the slope of the surface of the Wulff shape. The Wulff shape can be used to predict the structure of a randomly oriented surface. For example, a surface with the exact orientation of the A facet in Figure 2.11, n_A, will be flat because it will be composed of a single facet, A. A surface with the orientation n_1, which lies between the points marked **c** and **d** in Figure 2.11, will also have a flat surface which is composed of a complex facet. The term complex facet is used to describe a high-index plane that is part of a continuously curved portion of the Wulff shape. This particular Wulff shape also has missing orientations between the curved corners and facet B, which means that there are orientations that have energies that are too high for the surface to be stable with respect to faceting. Therefore, a surface with an orientation in the missing range, such as n_2, will facet into two surfaces: one with the orientation labeled **c** in Figure 2.11 and the other with the orientation of facet B. If the orientation of the surface is only slightly different from the orientation of facet B, the surface will be composed of large facets of B separated by small steps with orientation **c**. Likewise, if the orientation of the surface is close to orientation **c**, the surface will be composed of large complex facets of orientation **c** separated by small steps of facet B.

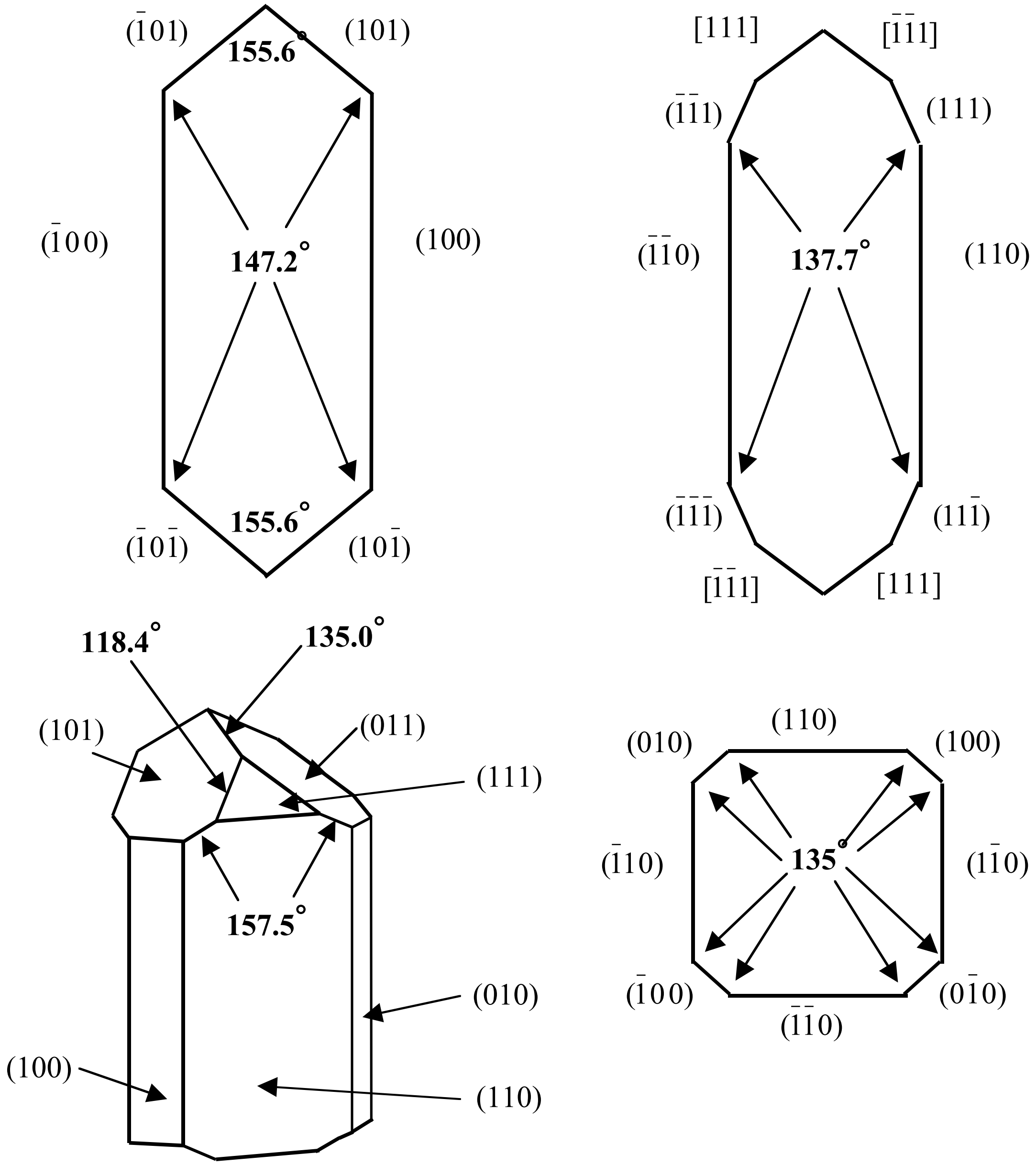

Figure 2.10—The angles between equilibrium facets at 0 K.

Another method for representing such a Wulff shape, described by Cahn and Handwerker in 1993 [53], takes advantage of the similarities between surface faceting and phase separation in ternary phase diagrams. This representation has been adopted for this thesis, and therefore, a short description follows. Curved surfaces, or those surfaces that are stable with respect to faceting, can be thought of as single-phase regions in a phase diagram. Surfaces composed of two distinct facets are analogous to two-phase

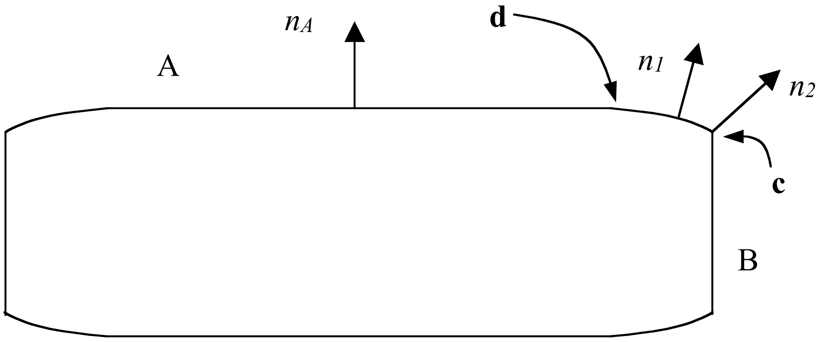

Figure 2.11—A hypothetical Wulff shape with complex facets and missing orientations.

regions in a phase diagram, and surfaces composed of three facets are analogous to three-phase regions in a phase diagram.

In more general terms, the surface normal, $\boldsymbol{n}$, is analogous to composition in the phase diagram, and the surface free energy for the i^{th} facet with respect to surface normal, $\gamma_i(\boldsymbol{n})$, corresponds to the free energy of a single phase in a phase diagram with respect to composition. Therefore, the surface free energy of each possible surface configuration can be drawn on a surface free energy versus surface orientation diagram, and the lowest

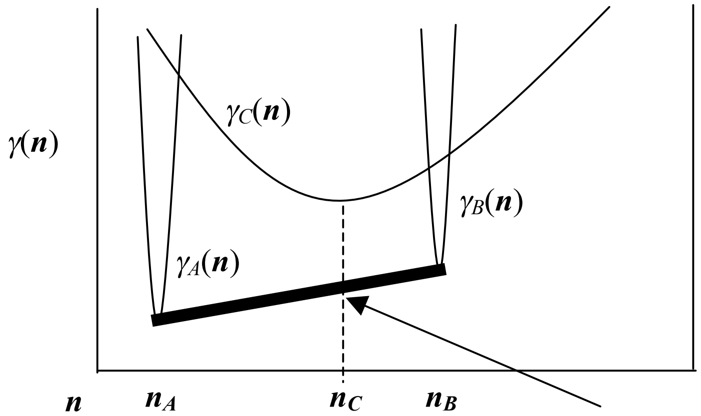

$(1 - k)\gamma_A(\boldsymbol{n}_A) + \mathrm{k}\gamma_B(\boldsymbol{n}_B) < \gamma_C(\boldsymbol{n}_C)$,

k is the fraction of surface B needed to maintain $\boldsymbol{n}_C$ as the surface orientation

Figure 2.12—The surface free energy as a function of orientation for three possible surfaces.

energy configuration can be determined in the same manner that the lowest energy combination of phases can be determined. For example, Figure 2.12 shows surface free energy functions for three surface configurations—A, B, and C—as they vary with surface normal. Surfaces A and B have the lowest surface free energy over a very narrow surface orientation range, while surface C has the lowest surface free energy over a much broader range. However, a surface with orientation $\boldsymbol{n_C}$, which lies in the orientation range where surface C has the lowest free energy, would have a lower energy if it faceted into two surfaces with orientations $\boldsymbol{n_A}$ and $\boldsymbol{n_B}$ than if it remained as a single surface, C.

In keeping with the idea that surface faceting is analogous to phase separation, an orientation stability figure can be constructed to summarize surface stability information for a given temperature. Figure 2.13 shows an example of an orientation stability figure for a hypothetical tetragonal material displayed using an inverse pole figure. The range of the inverse pole figure covers all of the unique orientations possible for this crystal structure. For a tetragonal material such as rutile, the orientations displayed in an inverse pole figure extend from {001} to {010} and {110}, as shown in Figure 2.13. A flat,

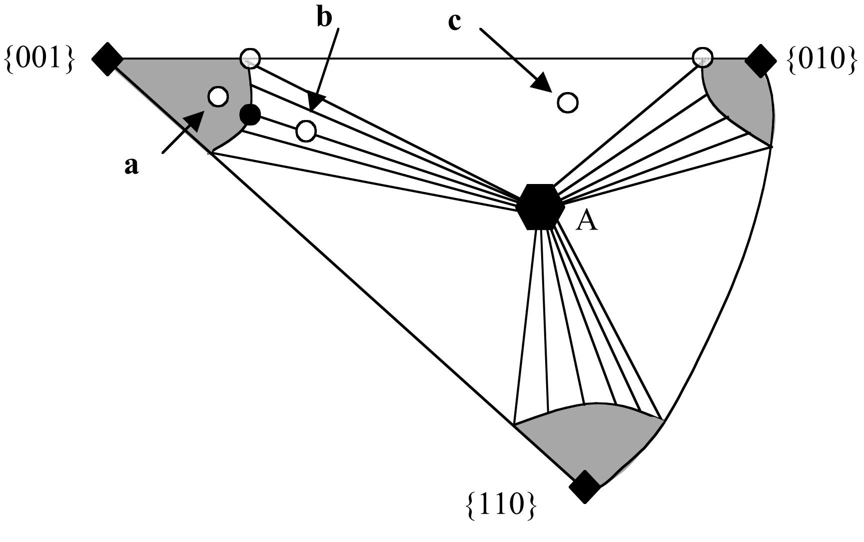

Figure 2.13—An orientation stability figure for a hypothetical tetragonal material.
a) Grey areas are stable with respect to faceting.
b) Lined areas facet into two facets, the orientations of which are at the end of the tie lines.
c) The white areas facet into three facets, the orientations of which are at the corners of the triangles.

planar facet is represented by a point in the orientation distribution diagram, such as the one labeled **A** in Figure 2.13. Ranges of orientations that are stable with respect to faceting are displayed in gray. Therefore, a surface with the orientation labeled **a** in Figure 2.12 is flat and unfaceted.

Orientations that facet into two distinct surfaces are displayed in the areas filled with tie lines, and the orientations of the two surfaces are found at the end of the tie line on which the overall surface orientation falls. For example, a surface with the orientation labeled **b** in Figure 2.13 will facet into two different surfaces: the orientation of one is shown by the black circle at the left end of the tie line and the orientation of the other is the surface labeled **A** on the right end of the tie line. The area of each of the two facets which are required to maintain the overall surface orientation can be calculated using the inverse lever rule, just as for binary phase diagrams.

Orientations that facet into three distinct surfaces are displayed in the white, unlined areas, and the orientations of the three surfaces are found at the corners of the triangle that bound the region. For example, a surface with the orientation labeled **c** in Figure 2.13 will facet into three different surfaces; the orientations of these surfaces are at the corners of the triangle bounding the region that contains **c**. One surface will have the orientation of facet A, and the orientations of the other two surfaces are indicated on the diagram by the small, patterned circles. The area of each facet needed to maintain the overall surface normal can be calculated in a manner similar to that used in the two-surface region. Figure 2.14 duplicates the area of interest in Figure 2.13. To determine the area of facet **A** on the surface, a line is drawn through the overall surface orientation

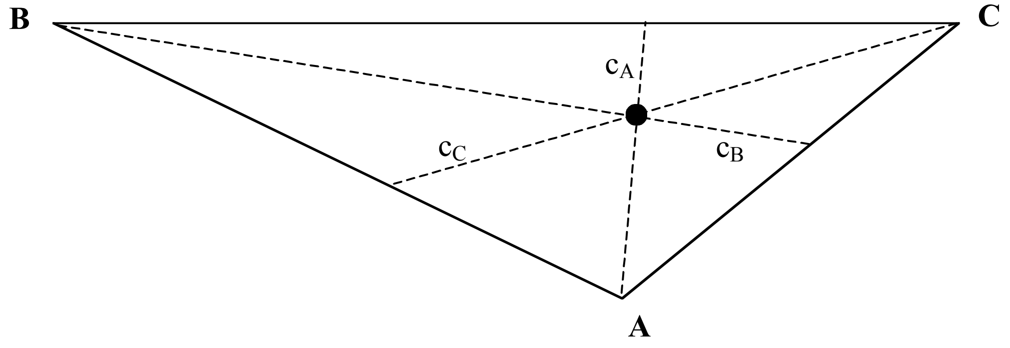

Figure 2.14—Determining the facet area in the three-facet region of the orientation stability figure.

extending from the orientation of facet **A** to the opposite tie line bounding the triangle, and c_A, the length of the line from the overall surface orientation to the tie line opposite facet **A**, is measured. Similarly, c_B and c_C are measured, and the area of the three surfaces can be computed as

$$\text{area of facet } \mathbf{A} = \frac{c_A}{c_A + c_B + c_C} \tag{2.6}$$

$$\text{area of facet } \mathbf{B} = \frac{c_B}{c_A + c_B + c_C}$$

$$\text{area of facet } \mathbf{C} = \frac{c_C}{c_A + c_B + c_C}$$

Although the identification of the facets on the surface of the rutile crystallites is an important goal, it is also important that the surface areas of the facets be calculated. The results can then be used to better correlate photochemical activity with the presence or absence of certain facets on the surface. For example, if photochemical activity increases with the area of a specific facet on the surface of the crystallites, it can be concluded that the active sites for both reduction and oxidation exist on a single surface. One of the goals of this work is the construction of an orientation stability figure for rutile so that the photochemical activity data can be analyzed in this manner.

2.5 General Faceting Theory

2.5.1 Surface Energy

As discussed in the previous section, the driving force behind faceting is a decrease in surface free energy. Assuming a fully faceted Wulff shape, Equation 2.5 can be used to determine the relative energies of the facets present on the Wulff shape [52]. If the Wulff shape is not fully faceted, the Herring equation [54] can be used to relate the angle between a singular facet and complex facet to the relative surface energies of the two facets. To use the Herring equation, the intersection between the complex and simple facet must be in local equilibrium; in other words, the angle between the complex and simple facets must be at equilibrium, although it is not necessary for the lateral scale

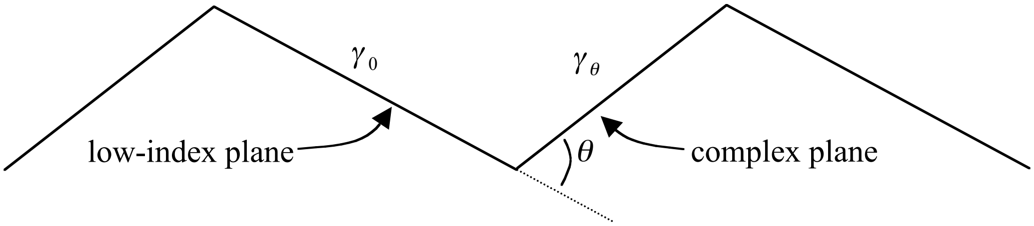

Figure 2.15—A schematic of a surface faceted into low-index and complex planes [55].

of the facets to be in equilibrium. For example, Figure 2.15 [55] shows a schematic of a surface that is faceted into a low-index plane and a complex plane. Applying the Herring equation to the intersection between the two facets, the ratio of surface energies is (Eq. 2.7) [54]

$$\frac{\gamma_0}{\gamma_\theta} = \cos\theta - \frac{1}{\gamma_\theta}\frac{\delta\gamma_\theta}{\delta\theta}\sin\theta \tag{2.7}$$

where γ_0 is the energy per unit area of the low-index plane, γ_θ is the energy per unit area of the complex plane, and θ is the angle between the low-index and complex planes as shown in Figure 2.15.

In 1958, Moore [55] measured θ for over 100 thermally faceted, silver crystallites. If one assumes that the torque term in Equation 2.7 ($\frac{1}{\gamma_\theta}\frac{\delta\gamma_\theta}{\delta\theta}\sin\theta$) is small, the ratio of the surface energies is

$$\frac{\gamma_0}{\gamma_\theta} = \cos\theta \tag{2.8}$$

Based on measurements of other fcc metals, this approximation appears to be justified [57]. Therefore, Moore [55] used Equation 2.8 to estimate the energies of the {111} and {100} surfaces of silver. In this thesis, Moore's [55] method of determining relative surface energies will be applied to rutile.

2.5.2 Kinetics

The kinetics of facet formation have not been studied, but there may be similarities between the equilibration of facets on a surface and the equilibration of small particle shapes on a substrate. In 1965, Nichols and Mullins [58] determined that the time for achieving shape equilibrium, τ, was

$$\tau = \frac{r^4 kT}{24\gamma D_s \nu \Omega^2} \tag{2.9}$$

where r is the radius of the particle, k is Boltzmann's constant, T is the temperature in Kelvin, γ is the surface energy, D_s is the surface diffusivity, ν is the number of surface atoms per unit area, and Ω is the atomic volume. In this thesis, we will make the assumption that facets on a randomly oriented surface evolve by surface diffusion and the kinetics resemble those of Equation 2.9. Therefore, if we use the facet width as the relevant length scale for Equation 2.9, the time-scale needed for the facets to reach an equilibrium shape can be estimated.

2.6 TiO_2 as a Photocatalyst

2.6.1 General Properties

Since 1971 when Fujishima and Honda [59] discovered that n-type TiO_2 can act as a photoelectrode for the splitting of water, there has been much interest in determining exactly how this property can be exploited. While the practical photocatalytic dissociation of water remains an elusive goal, TiO_2 coatings have recently been put to use both for their photocatalytic abilities as well as for their antifouling and antifogging capabilities [60–62]. Specifically, several research groups have been examining the ability of titania coatings on glass to avoid fogging and to remain clean in dirty environments. Wang et al. [62] determined that the reason for these behaviors is the ability of titania's surface to be both oleophilic and hydrophilic when exposed to ultraviolet light. The hydrophilic behavior means that the contact angle of water tends to 0°, preventing fog from forming on the surface. The dual oleophilic and hydrophilic behavior of the titania surfaces allows built up dirt and grime to be washed off by flowing water, such as rain. Although this behavior is not precisely photocatalytic, it is caused by the same phenomenon that creates photocatalysis. Wang et al. [62] hypothesized that Ti^{3+} sites, created by the adsorption of ultraviolet light, are hydrophilic while the rest of the surface remains oleophilic. The Ti^{3+} sites are so close together that the water spreads throughout the surface, leading to the overall hydrophilic behavior. A similar argument can be used to explain the overall oleophilic behavior. The antifogging, antifouling behavior of TiO_2 has already garnered some commercial interest, with certain car manufactures using titania coatings on the side view mirrors of their luxury cars for their antifogging capabilities [60].

Because of its low cost and chemical stability, titania is also the most promising of the photocatalysts for environmental clean-up [63]. Titania is one of the few photocatalysts that does not generate photocyclized intermediate products and that can completely oxidize almost all toxic wastes [3], including halocarbons [64–66], which are considered especially toxic and carcinogenic [67, 68]. Titania actually becomes more efficient at removing impurities from water if the water is contaminated with both organic materials and heavy metals [69] because organics are more easily oxidized than water and heavy metals are more easily reduced than oxygen. Titania mixed with activated carbon and Fe_2O_3 is also efficient at removing airborne pollutants in high-flow systems [70]. Titania coated on alumino-silicate hollow spheres has been used to oxidize crude oil floating on water with an estimated clean-up time of two to eight weeks [71]. Titania coatings have also been proposed for the inside of building windows to help remove irritants and contaminants from the air [61].

Titania is especially useful because the optimum quantum efficiency appears to occur at light intensities approximately equal to the sun's intensity [21]. At intensities greater than that of the sun, the extra light intensity decreases the quantum efficiency by increasing the efficiency of electron-hole recombination [19, 21]. To continue increasing the quantum efficiency as light intensity increases, an electron trap such as H_2O_2 must be added to the reaction solution [21].

Another major area of commercial interest is the reduction of the photochemical activity of titania in pigments. When a paint's polymer matrix degrades, the pigment is exposed as a white, chalky powder. Therefore, the degradation mechanism is called chalking. Research has shown that when exposed to light, the original titania pigments produce hydroxyl radicals, $^{\bullet}OH$, and perhydroxyl radicals, $^{\bullet}HO_2$ [5, 72]. These radicals are responsible for the destruction of the polymer matrix and the chalking process. Therefore, the production of improved, longer-lasting paints relies on suppressing titania's photoactivity.

As discussed in §2.1, the exact mechanism of the photocatalysis that occurs on titania's surface is not well understood. Some groups believe that hydroxyl radicals form on the surface and that they are responsible for the subsequent oxidation reactions [5–11]. According to research from other groups, holes directly oxidize adsorbed organic materials [13, 14], and adsorbed water acts only as an electron-hole recombination site and is therefore beneficial only when it is needed to remove radicals from the surface that could poison the reaction [14]. Still other groups have determined that both of the previously mentioned mechanisms can occur, depending on the concentration of the reactants in solution [12]. However, in spite of the many photocatalytic studies performed on TiO_2, few attempts have been made to link mechanisms with the details of the surface structure. Many of these studies were focused on identifying the active agent in the oxidation of organic compounds and did not relate the information they gained with surface orientations [5–14].

2.6.2 Modifications of TiO_2

In an effort to vary the photochemical properties of TiO_2, many modifications have been attempted, the most notable of which are doping and precious metal deposition.

Dopants have been added to TiO_2 in an attempt to improve photocatalytic properties. These studies have produced mixed and, in some cases, contradictory results. For instance, Mu et al. [73] determined that trivalent and pentavalent dopants have a detrimental effect on the photocatalytic activity of TiO_2, while studies by Karakitsou and Verykios [74] demonstrated that dopants with a valence higher than four enhanced the photoactivity of TiO_2. With the exception of doping with Cu(II) or Fe(III) [10, 70, 75–88], doping generally has deleterious effects on the photochemical properties [73, 80, 89–93].

Unlike doping, precious-metal deposition increases the photocatalytic activity of TiO_2 [16, 20, 94–102]. The most common explanation for this is that the noble metal acts as an electron scavenger, prevents the recombination of the electrons and holes, and increases the reduction rate of O_2, which would otherwise be the rate-limiting step in the reaction [15, 16]. Depositing a noble metal on the surface of TiO_2 can also make otherwise difficult or impossible reactions feasible [11, 103, 104], as well as change the reaction products in partial oxidation reactions [1, 98, 101, 105–109].

Not all modifications were aimed at increasing the photochemical activity of TiO_2. As mentioned in §2.4.1, the goal of numerous research projects was to reduce the photochemical activity of TiO_2 in order to produce more stable pigments. One such study examined the effects of metal acetate coatings [110]. The results of their study indicated that, of the 31 salts they examined, coatings of cerous acetate, zinc acetate, cobaltous acetate, and manganous acetate were the most effective, reducing the photoactivity by more than a factor of 50. Coatings of silver acetate, thallium acetate, and gallium acetate reduced the photoactivity by only ten percent. Further studies were completed using zinc acetate, and it was determined that one percent metal levels in the coating guaranteed the most effective deactivation of photoactivity.

2.6.3 Influence of Structure on the Reactivity of TiO_2

2.6.3.1 Bulk Structure

The photocatalytic properties of TiO_2 can be changed dramatically by varying the processing conditions. The two pure phases have different photoactivities for most reactions [111]. A multi-phase mixture called Degussa P25, commonly viewed as the standard for photocatalytic activity, has better photocatalytic properties than either pure phase in most cases [63]. Degussa P25 consists of a non-porous 70:30 anatase to rutile mixture with a BET surface area of 55±15 m^2/g and crystallite sizes of 30 nm in 0.1 mm aggregates [63].

Although it is commonly believed that anatase is the more active of the two commonly studied pure phases of TiO_2, there is no agreement about the reasons. Some studies actually seem to indicate that there should be little difference in the mechanisms for photocatalytic reactions on the two phases. Lusvardi et al. [112] tested the sensitivity of adsorption and catalytic reactions to the bulk structure of the catalyst. It was their hypothesis that because the cation coordination environments of both anatase and rutile are similar, there should be little difference in the products of catalytic reactions run on both polymorphs. This hypothesis was tested by exposing anatase and rutile powders to methanol, ethanol, and 2-propanol at room temperature. The results seemed to confirm their hypothesis. Although rutile adsorbed more of each alcohol, the ratio of methanol to ethanol to propanol adsorbed was the same on both oxides. High-temperature decomposition products were also identical on the two oxides, with a few minor differences in selectivity.

The study by Lusvardi et al. [112] decoupled the surface chemistry from the adsorption of light, which can be different for the two polymorphs. In a study by Riegel and Bolton [113], the pre-steady-state photoproduction of hydroxyl radicals was studied in a variety of rutile and anatase samples, and anatase was found to produce more hydroxyl radicals in all cases. Their hypothesis was that the slightly greater bandgap of anatase leads to a greater oxidative power. In other studies, Sangchakr et al. [94] and Tanaka et al. [114] found that commercial samples containing mainly anatase were more active than commercial samples containing mainly rutile in the degradation of sulfonated and chlorinated aromatics, even when the commercial samples containing mainly rutile were platinized. Results from a study by Weng et al. [115] indicate that anatase powder consisting of mainly {010} facets is more active than amorphous TiO_2, and that the same anatase powder is more active than rutile powder consisting of mainly {111} facets.

However, a study by Beck and Siegel [116] involving the dissociative adsorption of H_2S on nanophase TiO_2 in a H_2 environment determined that reduced nanophase rutile had the highest activity by a factor of approximately five. Of the other four powders tested in this study, the more active powders—calcined Degussa P25 and calcined $TiCl_4$—contained greater than 95% rutile, while the less active powders—Degussa P25 and calcined $Ti(OC_3H_7O)_4$—were mainly anatase. Only the reduced nanophase rutile showed significant activity after the first two hours of reaction; however, after the nanophase rutile particles were oxidized, the specific activity dropped somewhat, and all adsorption stopped after about two hours.

Other studies have produced equally varied results. Results from a study by Kenneke et al. [117] indicated that Degussa P25 has a higher activity than platinized anatase from Aldrich and that platinized anatase from Aldrich has a higher activity than un-platinized anatase from Aldrich in the destruction of trichloroethene. Results from a study by Ibusuki et al. [70] found that Degussa P25 is more active than amorphous TiO_2 in the oxidation of NO. This same study also determined that amorphous TiO_2 is more active than anatase and that rutile is inactive for this particular reaction. In a study by Domènech [118], several semiconductors, including Degussa P25, a TiO_2 powder consisting of 92% anatase, and a TiO_2 powder consisting of 89% rutile, were tested for their ability to degrade cyanide and Cr(VI). The 89% rutile powder was the best of the three and degraded 100% of the cyanide, compared with 64% degradation by Degussa P25 and 45% degradation by the 92% anatase powder. Only Degussa P25 showed appreciable activity in reducing Cr(VI) from solution primarily because it was the only form of TiO_2 stable in the Cr(VI) solution. An investigation by Mills and Sawunyama [4] compared the activity of amorphous TiO_2 to several commercial TiO_2 samples in the degradation of 4-chlorophenol. Although the amorphous TiO_2 had a very low photocatalytic activity, annealing it at temperatures less than 873 K increased its photoactivity, until eventually, the amorphous powder crystallized into a mixture of 70% anatase and 30% rutile. Although the annealed powder had a lower activity than any of the commercial powders examined, it did not produce the toxic intermediates that the commercial powders produced. The commercial powders were capable of degrading the toxic intermediates, but the degradation took much more time than the degradation of the 4-chlorophenol. In many cases, it rivaled the amount of time it took the annealed TiO_2 samples produced in the laboratory to totally mineralize the 4-chlorophenol.

These varied and contradictory results provide very clear evidence that material and surface properties that were not well characterized played an important role in determining the photocatalytic activity of the powders. Unfortunately, because very little characterization has been done to the TiO_2 powder surfaces beyond measuring specific surface area, there are very few theories that can explain the contradictory results. For example, although the level of sample oxidation or the presence of defects plays an important role in determining activity [116], very few research groups make any effort to determine the level of sample oxidation. Both impurities and minority phases are known to affect the activity of TiO_2. The minority phases can act as co-catalysts [70] or block active surface sites [119], and the impurities can have multiple effects. However, most studies that examine multiple samples simply use the commercial samples in their studies without testing for impurities or minority phases [70, 94, 113, 114, 117, 118]. Finally, it is difficult to make comparisons because few studies test more than one reaction and the reactions differ from study to study, but more meaningful comparisons could be done if the samples were better characterized and if an effort were made to use more uniform samples.

A few research groups have attempted to find reasons for the differences in activity between TiO_2 powders with different compositions. Bickley et al. [27] suggested that the enhancement of the space-charge potential in Degussa P25 due to the simultaneous presence of anatase, rutile, and amorphous TiO_2 may be the reason behind its enhanced photoactivity. The space charge potential acts to inhibit electron-hole recombination because the holes produced favor rutile while the electrons favor anatase.

Wang et al. [120] attempted to find a reason why anatase and rutile have different activities by studying the surface facet distribution of the two phases. In their investigation, a transmission electron microscope (TEM) was used to take selected area diffraction (SAD) patterns of both rutile and anatase samples. Thirty patterns per sample from different fields of view were taken and indexed, and all orientations occurring more than three times were analyzed. Wang et al. [120] determined that the exposed surfaces for anatase are mainly the {110}, {011}, {041}, {271}, {471}, and {064}; all but the {110} and the {011} are highly stepped. The exposed faces for rutile were mainly the {221}, {110}, {010}, {131}, and {113}. In general, these surfaces are not as highly stepped as the ones present on the anatase powders. Their hypothesis was that the more highly stepped surfaces of the anatase powders could produce more active sites on the surface, leading to the higher activity of anatase for many reactions. However, their research only pertains to pure anatase and rutile, not to the commonly available powders that are composed of both, and does not explain those cases where rutile has the higher activity.

One possibility that Wang et al. [120] overlooked is the presence of specific atomic arrangements on the surface of the common low-index surfaces of anatase that do not exist on the common low-index surfaces of rutile and might lead to the higher activity of the anatase powders. The fact that many of the high-index surfaces of anatase are highly stepped implies that they can be viewed as low-index planes connected by regular arrays of steps. Figure 2.16 shows the idealized surface structure of the two low-index planes found on the anatase particles examined by Wang et al. [120]. The anatase {110} plane, shown in Figure 2.16a, contains 4-coordinate Ti ions and 2-coordinate O-ions, similar to the {001} plane of rutile. The atomic structures on the two surfaces also appear similar, with each Ti ion on the surface flanked by two O ions in the surface plane and two more O ions in the plane immediately below. The anatase {011} surface, shown in Figure 2.16b, contains 5-fold coordinate Ti ions and 2- and 3-coordinate O ions, similar to the {011} plane in rutile. In this case, however, the atomic structures of the anatase {011} plane and the rutile {011} plane do not appear to be as similar as those of anatase {110} and rutile {001}.

As discussed in the next section, previous work on various surfaces of rutile have shown that activity and product distribution can depend on the surface upon which the reaction occurs. It is possible that the atomic structure of one or both of these surfaces contains sites that are favorable to photocatalysis and that these sites are responsible for the higher activity of the anatase powders and not the presence of steps on the high-index planes.

However, it is probably unreasonable to assume that the anatase {110} surface exists in its ideal state. The energy of the ideal rutile {001} surface is much higher than other low-index surfaces because of the low coordination of the Ti ions. It is expected that the energy of the ideal anatase {110} surfaces would also be higher than that of other low-index plane, such as {011}. It is possible that the {110} and {011} surfaces reconstruct in order to lower their energies and no longer appear like the ideal models in Figure 2.16. However, this does not preclude the presence of high activity sites on these surfaces.

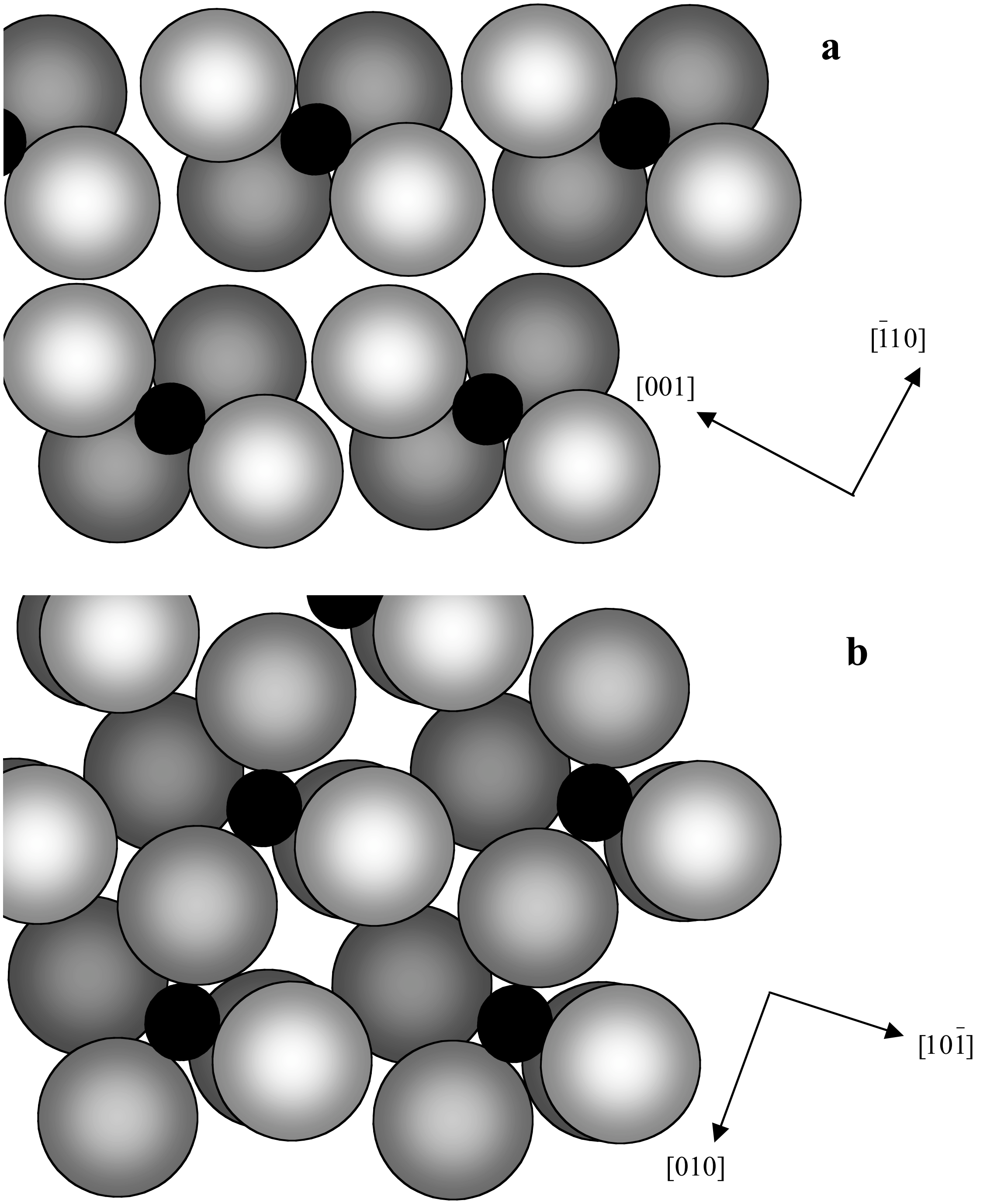

Figure 2.16—a) The surface ions of the {110} plane of anatase. Lighter O ions are slightly above the Ti plane, while darker O ions are slightly below the Ti plane.
b) The surface ions of the {011} plane of anatase. Light and medium gray O ions are above the Ti plane; the lightest ions are the highest. The darkest O ions are below the Ti plane.

2.6.3.2 Surface Chemistry

Although few experiments have examined the effect of surface structure on photocatalysis, many studies have examined the effect of surface structure on other chemical processes. For example, adsorption is frequently studied because it is the necessary precursor to photocatalysis. Determining the active sites for adsorption is equivalent to determining the active sites for photocatalysis. Table 2.4, which was compiled primarily by Henrich and Cox [28], lists the results of some of the adsorption studies, and these results seem to show that the adsorption of many substances is surface sensitive. Unfortunately, due to the difficulty of preparing reproducible surfaces, it is difficult to quantitatively compare results from different studies, so it is almost impossible to predict how a specific gas will adsorb to a specific surface under specific conditions.

Nowhere is that more of a problem than in studies which examine the adsorption of water on the different surfaces of TiO_2. As discussed in §2.1.1 and again in §2.6.1, most experimental results indicate that water adsorption is the first step of any photocatalytic cycle on TiO_2, especially in the presence of dilute contaminants [5–14].

Because water dissociation is the fundamental starting point of photocatalytic reactions, the adsorption of water has been examined by numerous research groups. However, each group's results seem to indicate different mechanisms for adsorption. The biggest differences seem to be the range of temperatures over which water exists molecularly on the surface, the extent of disassociation, and the role played by defects on each surface type. For the {110} surface, one group determined that a monolayer or less of molecularly adsorbed water remains on a nearly perfect surface until temperatures reach 250-300 K while multilayers desorb at 160 K [121]. Other groups determined that a monolayer or less of molecularly adsorbed water desorbs from a slightly defective surface when temperatures reach 170-190 K [122, 123]. At least two research groups report that the adsorption of water vapor at high enough pressures reduces the concentration of oxygen vacancies on the surface [124, 125], while one group found that the concentration of oxygen vacancies increases as water is adsorbed [123, 126].

Table 2.4: Surface Dependence of Adsorption on TiO_2 [compiled mainly by 28]

Molecule	Face	Surface Preparation	Adsorption Type	Comments	Source
H_2	{110}	UHV fractured	none	inert at 300 K	29
		P&A	II	H_2 is e^- donor	144
		P&A	II	$H_2 \rightarrow OH^-$; Ti-H at defects	145–148
	{010}	stoichiometric	none		148
		P&A, stoichiometric	II	H_2 is e^- donor	129
		P&A, reduced	II	H_2 is e^- acceptor at Ti(III) sites	129, 148
SO_2	{110}	P&A, stoichiometric	none	inert at 300 K	149–152
		stoichiometric		weak interaction	150, 153
		stoichiometric	I	molecular at 100 K; SO_4^{2-} at 300 K	154–156
		P&A	I	SO_3^{2-} at 300 K	149
		P&A, reduced	II	reacts at defect sites only	149–152
		reduced		oxidizes substrate	150, 151
			I	SO_3^{2-} at 300 K	149
	{441}	stepped	I and II	SO_3^{2-} and S_3^{2-} at 300 K	149
O_2	{110}	P&A, reduced	1st phase: II; 2nd phase: I	1st phase ends when defect states are depopulated	126, 146, 147, 157–159
		P&A, stoichiometric		weak at 300 K, probably at defects	126, 146, 147, 157–159
			I	O_2^-	148
		reduced		adsorbed on vacancy sites	126
		reduced	II(400K)	Ti(III) sites removed	123
			I(105K); II(400K)		160
		stoichiometric	none	none	126
	{010}	P&A, stoichiometric		weak at 300 K, probably at defects	129
		P&A, reduced	1st phase: II; 2nd phase: I	1st phase ends when defect states are depopulated	129
NH_3	{110}	stoichiometric	I	molecular at 300 K	161, 162
		highly defective	I	molecular at 300 K	161, 162
	{001}	P&A, faceted	I(300K); II(340K)	molecular at 300 K; some dissociation into NH_2 and OH^- at 340 K	163
CH_3OH	{110}	P&A	I	molecular at 300 K	149
	{441}	stepped	I	molecular at 300 K	149
	{001}	reduced	I and II	molecular and CH_3O^- at 300 K; desorbs as CH_3OH, CH_4, and CO	139
		faceted into {011}	II	CH_3O^- at 300 K; desorbs as CH_3OH, H_2O, CH_4, and HCHO	139
		faceted into {114}	II	CH_3O^- at 300 K; desorbs as CH_3OH, H_2O, CH_4, CH_3OCH_3, and HCHO	139

Table 2.4: Surface Dependence of Adsorption on TiO_2, cont'd.

Molecule	Face	Surface Preparation	Adsorption Type	Comments	Source
HCOOH	{110}	P&A	I	molecular at 300 K	149
	{441}	P&A	I	molecular at 300 K	149
	{001}	faceted to {011} and {114}	II	$HCOO^-$ at 300 K	164
CH_3COOH	{001}	faceted to {011}	I (200K); II(200K and 300K)	molecular and CH_3COO^- at 200 K; CH_3COO^- at 300 K; desorbs as H_2O, CO CH_3COOH, CH_2CO, and H_2	140
		faceted to {114}	I(200K); II(200K and 300K)	CH_3COO^- at 300 K; desorbs as H_2O, CO, CH_3COOH, CH_2CO CH_3COCH_3, and H_2	140
		reduced	II	mostly CH_3COO^- at 300 K; desorbs as H_2O, CO, CH_3COOH, CH_4, and CH_2CO	140
C_2H_5COOH	{001}	faceted to {011}	II	$C_2H_5COO^-$ at 300 K; desorbs as H_2O, CO, C_2H_5COOH, CH_3CHCO, and H_2	140
		faceted to {114}	II	$C_2H_5COO^-$ at 300 K; desorbs as H_2O, CO, C_2H_5COOH, H_2, $C_2H_5COC_2H_5$, and CH_3CHCO	140
HCHO	{110}	defective		CH_2=CH_2 at defect sites	124
	{010}	stoichiometric	II	methoxide and formate species	141
		reduced	II	adsorbed C, H, and O; desorbs CO, CO_2 and methoxide species	141
C_5H_5N	{110}	polished	I	molecular, via N atom to Ti	165
	{001}	polished	I	molecular, via N atom to Ti	165

I - molecular or non-dissociative adsorption
II - dissociative adsorption
P&A - polished and annealed

Similar confusion exists about the desorption state on the {010} surface. Henderson [127, 128] and Lo et al. [129] found that adsorbed water is less stable on reconstructed or reduced {010} surfaces. Muryn et al. [130, 131], however, concluded that water is equally stable on $TiO_2\{010\}(1\times1)$ and $TiO_2\{010\}(1\times3)$ surfaces. Other groups that have examined the effects of defects have found that defective surfaces are more active toward water dissociation [121, 126, 129, 132, 133] while others have found nearly identical behavior from defective and near-perfect surfaces [123, 130, 131, 134–138]. The two most recent studies indicate that approximately one-quarter of the water on the {110} surface adsorbs dissociatively [121], while approximately one-third of the water on the {010} surface adsorbs dissociatively [128].

The subject of this thesis is the structure sensitivity of the photocatalytic reactivity of rutile. At the start of this investigation, little data existed on this topic. The studies of Barteau and coworkers [139–141] on the thermal catalytic properties of rutile surfaces represent the most extensive investigation to date on the effect of the surface orientation of TiO_2 on catalytic reactions and are therefore worthy of special consideration. While TiO_2 can completely mineralize organic molecules when acting as a photocatalyst, it can also partially oxidize organic molecules in the absence of light. Barteau et al. [139, 140] demonstrated that the catalytic activity and selectivity of TiO_2 in partial oxidation reactions are related to surface structure. In their studies, three characteristic TiO_2\{001\} single crystal surfaces were used to catalyze the oxidation of methanol and carboxylic acid: the reduced surface, the {011}-faceted surface, and the {114}-faceted surface. The {114}-faceted surface produced additional products—dimethyl ether from methanol and 3-pentanone from carboxylic acid—that were not produced on the {011}-faceted surface. Barteau et al. [139, 140] hypothesized that these products were formed when two radicals attached to one four-coordinate titanium ion. Since only five-coordinate titanium ions are found on the {011}-faceted surface, the dimethyl ether and 3-pentanone could only form on the {114}-faceted surface, which does contain four-coordinate titanium ions.

Barteau et al. [141] also studied the decomposition of formaldehyde on the rutile {010} surface. On the reduced rutile {010} surfaces, formaldehyde decomposed to form C, H, and O, which react upon heating to form methoxide species, CO, and CO_2. On fully oxidized {010} rutile, however, formaldehyde molecules split to form methoxide and formate. Another study, which examined the decomposition of formaldehyde on a reduced TiO_2\{110\} surface, determined that the catalytic reaction produced ethylene [124]. Barteau et al. [142] also examined the reductive coupling of aldehydes to form olefins in the more general case and determined that the reaction requires a partially reduced rutile surface to occur.

An ultra-high vacuum study of the degradation of CH_3Cl on rutile {110} found that oxygen vacancies are also the active sites for the photocatalytic oxidation of CH_3Cl, which produces CO, HCl, formaldehyde, and water [111]. Wong et al. [143] examined degradation of CH_3Cl over a TiO_2 powder consisting of a mixture of rutile and anatase and found that the final products of the degradation were CO_2, H_2O and HCl; the CO and formaldehyde had been completely mineralized.

Although the previously mentioned studies pertain to thermal catalysis and not photocatalysis, the existence of surface structure sensitivity indicates that different mechanisms may be at work on different surfaces. Although the different mechanisms should not affect the final product distribution of photocatalysis—H_2O, CO_2, and mineral acids [3]—the different mechanisms may lead to less toxic intermediate products and permit the reaction to proceed faster on surfaces whose structure allows for a more efficient reaction pathway.

2.7 References

[1] A. Wold, *Chem. Mater.* **5** (1993) 280.
[2] G. Rothenberger, J. Moser, M. Grätzel, N. Serpone, and D. Sharma, *J. Am. Chem. Soc.* **107** (1985) 8054.
[3] N. Serpone, R. Terzian, C. Minero, and E. Pelizzetti, *in* "Photosensitive Metal-Organic Systems: Mechanistic Principles and Applications", (C. Kutal and N. Serpone, Eds.), p281, American Chemical Society, Washington, D.C. (1993).
[4] A. Mills and P. Sawunyama, *J. Photochem. Photobiol. A: Chem.* **84** (1994) 305.
[5] H. Völz, G. Kaempf, H. Fitzky, and A. Klaeren, *in* "Photodegradation and Photostabilization of Coatings", (S. Pappas and F. Wilson, Eds.), p163, American Chemical Society (1981).
[6] R. Matthews, *in* "Photochemical Conversion and Storage of Solar Energy", (E. Pelizzetti and M. Schiavello, Eds.), p427, Kluwer Academic, Dordrecht, Netherlands (1991).
[7] R. Matthews, *J. Chem. Soc. Faraday Trans.* **80** (1984) 457.
[8] I. Izumi, W. Dunn, K. Willbourn, F. Fan, and A. Bard, *J. Phys. Chem.* **84** (1980) 3207.
[9] I. Izumi, F. Fan, and A Bard, *J. Phys. Chem.* **85** (1981) 218.
[10] M. Fujihira, Y. Satoh, and T. Osa, *Bull. Chem. Soc. Jpn.* **55** (1982) 666.
[11] D. Ollis, E. Pelizzetti, and N. Serpone, *Environ. Sci. Technol.* **25** (1991) 1522.
[12] S. Goldstein, G. Czapski, and J. Rabani, *J. Phys. Chem.* **98** (1994) 6586.

[13] M. Anpo, K. Chiba, M. Tomonari, S. Coluccia, M. Che, and M. Fox, *Bull. Chem. Soc. Jpn.* **64** (1991) 543.

[14] O. Micic, Y. Zhang, K. Cromack, A. Trifunac, and M. Thurnauer, *J. Phys. Chem.* **97** (1993) 7277.

[15] H. Gerischer and A. Heller, *J. Phys. Chem.* **95** (1991) 5161.

[16] J. Kesselman, G. Shreve, M. Hoffman, and N. Lewis, *J. Phys. Chem.* **98** (1994) 13385.

[17] N. Serpone, R. Terzian, D. Lawless, P. Kennepohl, and G. Sauvé, *J. Photochem. Photobiol. A: Chem.* **73** (1993) 11.

[18] I. Rosenberg, J. Brock, and A. Heller, *J. Phys. Chem.* **96** (1992) 3423.

[19] M. Aguado, M. Anderson, and C. Hill, Jr., *J. Molecular Cat.* **89** (1994) 165.

[20] R. Suri, J. Liu, D. Hand, J. Crittenden, D. Perram, and M. Mullins, *Water Environ. Res.* **65** (1993) 665.

[21] R. Matthews, *in* “Photocatalytic Purification and Treatment of Water and Air”, (D. Ollis and H. Al-Ekabi, Eds.), p121, Elsevier, New York (1993).

[22] J. Burdett, *Inorg. Chem.* **24** (1985) 2244.

[23] J. Burdett, T. Hughbands, J. Gordon, J. Richardson, Jr., and J. Smith, *J. Am. Chem. Soc.* **109** (1987) 3639.

[24] A. Fahmi, C. Minot, B. Silvi, and M. Causa, *Phys. Rev. B* **47** (1993) 11717.

[25] M. Ramamoorthy, D. Vanderbilt, and R. King-Smith, *Phys. Rev. B* **49** (1994) 16721.

[26] R. Sanjines, H. Tang, H. Berger, G. Margaritondo, and F. Levy, *J. Appl. Phys.* **75** (1994) 2945.

[27] R. Bickley, T. Gonzalez-Carreno, J. Lees, L. Palmisano, and R. Tilley, *J. Solid State Chem.* **92** (1991) 178.

[28] V. Henrich and P. Cox, “The Surface Structure of Metal Oxides”, Cambridge University Press, Cambridge (1994).

[29] V. Henrich and R. Kurtz, *Phys. Rev. B* **23** (1981) 6280.

[30] V. Henrich, *Rep. Prog. Phys.* **48** (1985) 1481.

[31] V. Henrich, *Prog. in Surf. Sci.* **14** (1983) 175.

[32] A. Szabo and T. Engel, *Surf. Sci.* **329** (1995) 241.

[33] P. Murray, N. Condon, and G. Thornton, *Phys. Rev. B* **51** (1995) 10989.

[34] H. Onishi and Y. Iwasawa, *Surf. Sci*. **313** (1994) L783.

[35] M. Sander and T. Engel, *Surf. Sci.* **302** (1994) L263.

[36] G. Rohrer, V. Henrich, and D. Bonnell, *Surf. Sci.* **278** (1992) 146.

[37] S. Fischer, A. Munz, K. Schierbaum, and W. Göpel, *Surf. Sci.* **337** (1995) 17.

[38] W. Lo, Y. Chung, and G. Somorjai, *Surf. Sci.* **71** (1978) 199.

[39] P. Zschack, J. Cohen, and Y. Chung, *Surf. Sci.* **262** (1992) 395.

[40] G. Clark and L. Kesmodel, *Ultramicroscopy* **41** (1992) 77.

[41] P. Hardman, N. Prakash, C. Muryn, G. Raiker, A. Thomas, A. Prime, G. Thornton, and R. Blake, *Phys. Rev. B* **47** (1993) 16056.

[42] P. Murray, F. Leibsle, H. Fischer, C. Flipse, C. Muryn, and G. Thornton, *Phys. Rev. B* **46** (1992) 12877.

[43] L. Firment, *Surf. Sci.* **116** (1982) 205.
[44] G. Poirier, B. Hance, and J. White, *J. Vac. Sci. Technol. B* **10** (1992) 6.
[45] R. Tait and R. Kasowski, *Phys. Rev. B* **20** (1979) 5178.
[46] R. Kurtz, *Surf. Sci.* **177** (1986) 526.
[47] L. Wang, J. Liu, and J. Cowley, *Surf. Sci.* **302** (1994) 141.
[48] E. De Frésar, J. Darville, and J. Gilles, *Surf. Sci.* **126** (1983) 518.
[49] P. Jones and J. Hockey, *Trans. Faraday Soc.* **67** (1971) 2669.
[50] P. Jones and J. Hockey, *Trans. Faraday Soc.* **67** (1971) 2679.
[51] P. Jones and J. Hockey, *J. Chem. Soc. Faraday Trans.* **68** (1972) 907.
[52] G. Wulff, *Z. Kristallogr.* **34** (1901) 449.
[53] J. Cahn and C. Handwerker, *Mater. Sci. Eng. A* **162** (1993) 83.
[54] C. Herring *in* "Structure and Properties of Solid Surfaces", (Gomer and Smith, Eds.), p5, Chicago University Press, Chicago (1953).
[55] A. Moore *in* "Metal Surfaces: Structure, Energetics and Kinetics", (N. Gjostein and W. Robertson, Eds.) p155, American Society for Metals, Metals Park (1963).
[56] A. Moore, *Acta Met.* **6** (1958) 293.
[57] H. Mykura, *Acta Met.* **9** (1961) 570.
[58] F. Nichols and W. Mullins, *Trans. AIME* **233** (1965) 1840.
[59] A. Fujishima and K. Honda, *Bull. Chem. Soc. Jap.* **44** (1971) 1148.
[60] R. Dagani, *C&EN* (September 21, 1998) 70.
[61] H. Tada and M. Tanaka, *Langmuir* **13** (1997) 360.
[62] R. Wang, K. Hashimoto, A. Fujishima, M. Chikuni, E. Kojima, A. Kitamura, M. Shimohigoshi, and T. Watanabe, *Nature* **388** (1997) 431.
[63] M. Hoffman, S. Martin, W. Choi, and D. Bahnemann, *Chem. Rev.* **95** (1995) 69.
[64] A. Pruden and D. Ollis, *J. Catal.* **82** (1983) 404.
[65] D. Ollis, C. Hsiao, and C. Lee, *J. Catal.* **82** (1983) 418.
[66] D. Ollis, C. Hsiao, L. Budeman, and C. Lee, *J. Catal.* **88** (1984) 89.
[67] "Annual report on Carcinogenisis Bioassay of Chloroform," National Cancer Institute, Bethesda, MD (1976).
[68] M. Stein and F. Sansome, "Degradation of Chemical Carcinogens", Van Nostrand Reinhold, New York (1980).
[69] M. Praire, B. Stange, and L. Evans, *in* "Photocatalytic Purification and Treatment of Water and Air", (D. Ollis and H. Al-Ekabi, Eds.), p353, Elsevier, New York (1993).
[70] T. Ibusuki, S. Kutsuna, K. Takeuchi, K. Shin-kai, T. Sasamoto, and M. Miyamoto, *in* "Photocatalytic Purification and Treatment of Water and Air", (D. Ollis and H. Al-Ekabi, Eds.), p375, Elsevier, New York (1993).
[71] A. Heller, M. Nair, L. Davidson, Z. Luo, J. Schwitzgebel, J. Norrell, J. Brock, S. Lindquist, and J. Ekerdt, *in* "Photocatalytic Purification and Treatment of Water and Air", (D. Ollis and H. Al-Ekabi, Eds.), p139, Elsevier, New York (1993).
[72] S. Pappas and R. Fischer, *J. of Paint Tech.* **46** (1974) 65.
[73] W. Mu, J. Herrmann, and P. Pichat, *Catal. Lett.* **3** (1989) 73.
[74] K. Karakitsou and X. Verkios, *J. Phys Chem.* **97** (1993) 1184.

[75] D. Bahnemann, D. Bockelmann, R. Goslich, M. Hilgendorff, and D. Weichgrebe, *in* "Photocatalytic Purification and Treatment of Water and Air", (D. Ollis and H. Al-Ekabi, Eds.), p301, Elsevier, New York (1993).

[76] A. Milis, J. Peral, X. Domènech, and J. Navío, *J. Molecular Catal.* **87** (1994) 67.

[77] M. Litter and J. Navío, *J. Photochem. Photobiol. A: Chem.* **84** (1994) 183.

[78] S. Martin, H. Herrmann, W. Choi, and M. Hoffman, *Trans. Faraday Soc.* **90** (1994) 3315.

[79] S. Martin, H. Herrmann, and M. Hoffman, *Trans. Faraday Soc.* **90** (1994) 3323.

[80] T. Watanabe, A. Kitamura, E. Kojima, C. Nakayama, K. Hashimoto, and A. Fujishima, *in* "Photocatalytic Purification and Treatment of Water and Air", (D. Ollis and H. Al-Ekabi, Eds.), p747, Elsevier, New York (1993).

[81] E. Butler and A. Davis, *J. Photochem. Photobiol. A: Chem.* **70** (1993) 273.

[82] J. Moser, M. Grätzel, and R. Gallay, *Helv. Chim. Acta* **70** (1987) 1596.

[83] J. Soria, J. Conesa, V. Augugliaro, L. Palmisano, M. Schiavello, and A. Sclafani, *J. Phys. Chem.* **95** (1991) 274.

[84] A. Sclafani, L. Palmisano, and M. Schiavello, *Res. Chem. Intermed.* **18** (1992) 211.

[85] M. Schiavello and A Sclafani, *in* "Photoelectrochemistry, Photocatalysis and Photoreactor", (M. Schiavello, Ed.), p503, *NATO-ASI, Ser. C*, **146** (1985).

[86] R. Bickley and J. Navío, *in* "Photocatalytic Production of Energy-rich Compounds", (G. Grassi and D. Hall, Eds.), p105, Elsevier, (1985).

[87] V. Augugliaro and L. Palmisano, *in* "Photocatalysis and Environment", (M. Schiavello, Ed.), p425, Kluwer, Amsterdam (1988).

[88] M. Grätzel and R. Howe, *J. Phys. Chem.* **94** (1990) 2566.

[89] J. Herrmann, J. Disdier, and P. Pichat, *Chem. Phys. Lett.* **108** (1984) 618.

[90] E. Borgarello, J. Kiwi, M. Grätzel, E. Pelizzetti, and M. Visca, *J. Am. Chem. Soc.* **102** (1982) 2996.

[91] J. Kiwi and C. Morrison, *J. Phys. Chem.* **88** (1984) 6146.

[92] J. Kiwi and M. Grätzel, *J. Phys. Chem.* **90** (1986) 637.

[93] Z. Luo and Q. Gao, *J. Photochem. Photobiol. A: Chem.* **63** (1992) 367.

[94] B. Sangchakr, T. Hisanaga, and K. Tanaka, *J. Photochem. Photobiol. A: Chem.* **85** (1995) 187.

[95] E. Serpone, E. Borgarello, M. Barberi, and E. Pelizzetti, *Inorg. Chem. Acta* **90** (1984) 191.

[96] L. Childs and D. Ollis, *J. Catal.* **66** (1980) 383.

[97] W. Lee, Y. Gao, K. Dwight, and A. Wold, *Mater. Res. Bull.* **27** (1992) 685.

[98] M. Albert, Y. Gao, D. Toft, and K. Dwight, *Mater. Res. Bull.* **27** (1992) 961.

[99] Y. Gao, H. Shen, K. Dwight, and A. Wold, *Mater. Res. Bull.* **27** (1992) 1023.

[100] C. Wang, A. Heller, and H. Gerischer, *J. Am. Chem. Soc.* **114** (1992) 5230.

[101] A. Sclafani, M. Mozzanega, and P. Pichat, *J. Photochem. Photobiol. A: Chem.* **59** (1991) 181.

[102] X. Fu, W. Zeltner, and M. Anderson, *App. Catal. B: Environ.* **6** (1995) 209.

[103] S. Sato and J. White, *Chem. Phys. Lett.* **72** (1980) 83.

[104] T. Kutty and M. Avudaithai, *Mat. Res. Bull.* **23** (1988) 725.

[105] K. Tennakone, *Sol. Energy. Mat.* **10** (1984) 235.
[106] W. Rophael and M. Malati, *J. Chem. Soc., Chem. Commun.* (1987) 1418.
[107] O. Ishitani, C. Inoue, Y. Suzuki, and T. Ibusuki, *J. Photochem. Photobiol. A: Chem.* **72** (1993) 269.
[108] I. Inoue, A. Fujishima, S. Konishi, and K. Honda, *Nature* **277** (1979) 637.
[109] M. Trillas, J. Peral, and X. Domènech, *Appl. Catal. B: Environ.* **5** (1995) 377.
[110] G. Irick, Jr., G. Newland, and R. Wang *in* "Photodegradation and Photostabilization of Coatings", (M. Pappas and F. Wilson, Eds.), p147, American Chemical Society (1981).
[111] A. Linsebigler, G. Lu, and J. Yates, Jr., *Chem. Rev.* **95** (1995) 735.
[112] V. Lusvardi, M. Barteau, and W. Farneth, *J. Catal.* **153** (1995) 41.
[113] G. Riegel and J. Bolton, *J. Phys. Chem.* **99** (1995) 4215.
[114] K. Tanaka, T. Hisanaga, and A. Rivera, *in* "Photocatalytic Purification and Treatment of Water and Air", (D. Ollis and H. Al-Ekabi, Eds.), p169, Elsevier, New York (1993).
[115] Y. Weng, F. Wang, L. Lin, and R. Xie, *in* "Photocatalytic Purification and Treatment of Water and Air, (D. Ollis and H. Al-Ekabi, Eds.), p713, Elsevier, New York (1993).
[116] D. Beck, and R. Siegel, *J. Mater. Res.* **7** (1992) 2840.
[117] J. Kenneke, J. Ferry, and W. Glaze, *in* "Photocatalytic Purification and Treatment of Water and Air", (D. Ollis and H. Al-Ekabi, Eds.), p179, Elsevier, New York (1993).
[118] X. Domènech, *in* "Photocatalytic Purification and Treatment of Water and Air", (D. Ollis and H. Al-Ekabi, Eds.), p337, Elsevier, New York (1993).
[119] J. Navío, M. Macías, M. González-Catalán, and A. Justo, *J. Mat. Sci.* **27** (1992) 3036.
[120] F. Wang, Y. Weng, L. Lin, *in* "Photocatalytic Purification and Treatment of Water and Air", (D. Ollis and H. Al-Ekabi, Eds.), p753, Elsevier, New York (1993).
[121] M. Hugenschmidt, L. Gamble, and C. Campbell, *Surf. Sci.* **302** (1994) 329.
[122] V. Henrich, G. Dresselhaus, and H. Zeiger, *Solid State Commun.* **24** (1977) 623.
[123] R. Kurtz, R. Stockbauer, T. Madey, and E. Román, J. de Segovia, *Surf. Sci.* **218** (1989) 178.
[124] G. Lu, A. Linsebigler, and J. Yates, Jr., *J. Phys. Chem.* **98** (1994) 11733.
[125] L. Wang, D. Baer, and M. Engelhard, *in* "Materials Research Society Symposium Proceedings Volume 357: Structure and Properties of Interfaces in Ceramics", (D. Bonnell, M. Rühle, and U. Chowdhry, Eds.), p97, Materials Research Society, Pittsburgh (1995).
[126] J. Pan, B. Maschhoff, U. Diebold, and T. Madey, *J. Vac. Sci. Technol. A* **10** (1992) 2470.
[127] M. Henderson, *in* "Materials Research Society Symposium Proceedings Volume 357: Structure and Properties of Interfaces in Ceramics", (D. Bonnell, M. Rühle, and U. Chowdhry, Eds.), p91, Materials Research Society, Pittsburgh (1995).
[128] M. Henderson, *Surf. Sci.* **319** (1994) 315.

[129] W. Lo, Y. Chung, and G. Somorjai, *Surf. Sci.* **71** (1978) 199.

[130] C. Muryn, G. Tirvengadum, J. Crouch, D. Warburton, G. Raiker, G. Thornton, and D. Law, *J. Phys. Condens. Matter* **1** (1989) SB127.

[131] C. Muryn, P. Hardman, J. Crouch, G. Raiker, G. Thornton, and D. Law, *Surf. Sci.* **251/252** (1991) 747.

[132] S. Bourgeois, F. Jomard, and M. Perdereau, *Surf. Sci.* **279** (1992) 349.

[133] S. Eriksen, P. Naylor, and R. Egdell, *Spectrochim. Acta* **43A** (1987) 1535.

[134] T. Sham and M. Lazarus, *Chem. Phys. Lett.* **68** (1979) 426.

[135] M. Lazarus and T. Sham, *Chem. Phys. Lett.* **92** (1982) 670.

[136] P. Smith and S. Bernasek, *Surf. Sci.* **188** (1987) 241.

[137] F. Bustillo, E. Román , and J. de Segovia, *Vacuum* **39** (1989) 659.

[138] F. Bustillo, E. Román , and J. de Segovia, *Vacuum* **41** (1990) 19.

[139] K. Kim and M. Barteau, *Surf. Sci.* **223** (1989) 13.

[140] K. Kim and M. Barteau, *J. Catal.* **125** (1990) 353.

[141] H. Idriss, K. Kim, and M. Barteau, *Surf. Sci.* **262** (1992) 113.

[142] H. Idriss, K. Pierce, and M. Barteau, *J. Am. Chem. Soc.* **113** (1991) 715.

[143] J. Wong, A. Linsebigler, G. Lu, J. Fan, and J. Yates, Jr., *J. Phys. Chem.* **99** (1995) 335.

[144] G. Rocker and W. Göpel, *Surf. Sci.* **175** (1980) L675.

[145] G. Rocker, J. Schaefer, and W. Göpel, *Phys. Rev. B* **30** (1984) 3704.

[146] G. Göpel, U. Kirner, H. Wiehöfer, and G. Rocker, *Solid State Ionics* **28-30** (1988) 1423.

[147] W. Göpel, *Prog. Surf. Sci.* **20** (1985) 9.

[148] W. Göpel, G. Rocker, and R. Feierabend, *Phys. Rev. B* **28** (1983) 3427.

[149] H. Onishi, T. Aruga, C. Egawa, and Y. Iwasawa, *Surf. Sci.* **193** (1988) 33.

[150] K. Smith, J. Mackay, and V. Henrich, *Phys. Rev. B* **35** (1987) 5822.

[151] K. Smith and V. Henrich, *J. Vac. Sci. Technol. A* **7** (1989) 1967.

[152] K. Smith, J. Mackay, and V. Henrich, *J. Vac. Sci. Technol. A* **5** (1987) 689.

[153] K. Smith and V. Henrich, *Phys Rev.* B **32** (1985) 5384.

[154] G. Thornton, *J. Phys.: Condens. Matter* **1** (1989) SB111.

[155] C. Muryn, D. Purdie, P. Hardman, A. Johnson, N. Prakash, G. Raiker, G. Thornton, and D. Law, *Faraday Disc. Chem. Soc.* **89** (1990) 77.

[156] D. Warburton, D. Purdie, C. Muryn, K. Prabhakaran. P. Wincott, and G. Thornton, *Surf. Sci.* **269/270** (1992) 305.

[157] V. Henrich, G. Dresselhaus, and H. Zeiger, *Phys. Rev. Lett.* **36** (1976) 1335.

[158] V. Henrich, G. Dresselhaus, and H. Zeiger, *J. Vac. Sci. Technol.* **15** (1978) 534.

[159] M. Knotek, *in* "Electrode Materials and Processes for Energy Conversion and Storage", (Eds.), p234, Electrochemical Society, Princeton (1977).

[160] G. Lu, A. Linsebigler, and J. Yates, Jr., *J. Chem. Phys.* **102** (1995) 1005.

[161] U. Diebold and T. Madey, *J. Vac. Sci. Technol.* **10** (1992) 2327.

[162] E. Román, J. de Segovia, R. Kurtz, R. Stockbauer, and T. Madey, *Surf. Sci.* **273** (1992) 40.

[163] E. Román and J. de Segovia, *Surf. Sci.* **251/252** (1991) 742.

[164] K. Kim and M. Barteau, *Langmuir* **6** (1990) 1485.
[165] H. Yamada and Y. Yamamoto, *Surf. Sci.* **134** (1983) 71.

Chapter 3

Experimental Procedure

3.1 Sample Preparation

3.1.1 Thin Film Preparation

All rutile single crystal thin films were grown at DuPont by Morris Hotsenpiller [1] using an ion-beam sputtering system developed to produce complex-oxide thin films. All substrates were epitaxially polished by the supplier and were rinsed with high-purity methanol prior to being introduced into the reaction chamber. MgO substrates were kept under vacuum in order to prevent the formation of hydroxides on the surface. All substrates were kept in dryboxes prior to use. The growth chamber was evacuated to 10^{-7} Torr. Substrates were introduced into the chamber using a load-lock. The substrate stage was heated with halogen lamps, and the temperature was monitored with a thermocouple and an infrared pyrometer. A high-purity (99.995%) titanium target was struck with a Xe ion beam from a 3 cm Kauffman-type ion source. The ion beam current and energy were 20 mA and 1000 eV, respectively. The growth atmosphere was 10^{-4} Torr of Xe and 10^{-4} Torr of O_2. Films were grown at either 873 K or 1023 K with a growth rate between 3 Å/min and 7 Å/min. Table 3.1 identifies the growth conditions of specific films. The titanium to oxygen ratios of the films were measured using Rutherford backscattered diffractometry, and phase identification was accomplished using x-ray diffraction.

Table 3.1: Growth Parameters of Rutile Thin Films [1]

Film	Substrate	Growth Temperature(K)	Thickness (Å)
{010}	{0001}Al_2O_3	998	700 2200 4500
{011}	$\{11\bar{2}0\}$ Al_2O_3	998	700 2200 4500
{001}	$\{10\bar{1}0\}$ Al_2O_3	998	700 2200
{110}	{110}MgO	873	700 2200

3.1.2 Polycrystalline Rutile Preparation

3.1.2.1 Ceramic Synthesis

All polycrystalline samples were prepared in-house. The amount of iron, silicon, and aluminum impurities in the starting rutile powder was analyzed using flame pyrolysis and found to be 13 ppm aluminum, 40 ppm silicon, and less than 10 ppm iron. The rutile powder without milling was placed in a graphite mold with an approximate inside diameter of 11 mm and compacted in a uniaxial press at 140 MPa pressure to form a disk approximately 2.5 mm thick. The pellet was then removed from the mold, encased in latex, and compacted in a hydrostatic press at 280 MPa. The green pellet was placed in an alumina crucible and surrounded by loose rutile powder from the same source as the starting powder. The alumina crucible containing 10 pellets and loose rutile powder was then covered with an alumina plate, and the pellets were sintered in air by heating to 1873 K at one atmosphere at a rate of 5 K/min, holding at that temperature for 24 hours, and then cooling at a rate of 5 K/min to room temperature. The grains in the fired pellets were equiaxed with no texture, and the average final grain size was approximately 50 μm with sizes ranging from approximately 5 μm to more than 200 μm. All of the results described in this thesis are derived from one of 10 pellets produced in a single heat.

3.1.2.2 Polishing

Samples were ground on SiC impregnated papers at grits ranging from 240 to 600. Initially, samples were then polished in alumina slurries ranging from 1 μm to 0.05 μm. However, it was discovered that ensuring the removal of all the alumina powder from the surface after polishing was difficult. After generating inconsistent results in subsequent experiments designed to measure photocatalytic activity, it was hypothesized that the rutile samples were being contaminated with alumina. Therefore, later samples were polished using a series of diamond pastes with particle sizes of 6 μm, 3 μm, 1 μm, and 0.25 μm. The samples were rinsed in distilled water after each grinding and polishing step. After the final step, the rutile samples were rinsed in distilled water, cleaned ultrasonically in distilled water, rinsed one final time in distilled water, and dried in air at 393 K.

3.1.2.3 Etching

Grain boundary grooving and faceting were accomplished initially by thermally etching the polished surfaces in air at 1473 K for four or eight hours. Polished pellets were placed on a thick bed of rutile powder from the same source as the starting powder on the alumina plate used for the initial sintering. The polished pellet was then covered with the alumina crucible used in the initial sintering before being placed in the furnace. The ramp rate both up to 1473 K and down to room temperature was 5 K/min. Samples were ultrasonically cleaned in distilled water after the thermal etch to remove any loose surface particles. After the thermal etch, the aluminum concentration in the pellet remained unchanged at 11 ppm, the iron concentration in the pellet remained less than 10 ppm, and the silicon concentration in the pellet had increased to 100 ppm.

3.2 Photocatalytic Silver Reduction

As discussed in §2.1.1, rutile is capable of catalyzing chemical reactions when in the presence of light with energy greater than its bandgap. In this thesis, we are using the reduction of silver ions to silver metal (Eq. 3.1) to measure rutile photochemical activity.

$$\mathrm{Ag^+_{ads}} + \mathrm{e^-} \xrightarrow{\mathrm{TiO_2}} \mathrm{Ag^0_{ads}} \tag{3.1}$$

The oxidation of water (Eq. 3.2) is the complementary oxidation reaction.

$$\mathrm{H_2O_{ads}} + \mathrm{h^+} \xrightarrow{\mathrm{TiO_2}} {}^{\bullet}\mathrm{OH} + \mathrm{H^+} \tag{3.2}$$

The samples are immersed in an aqueous $AgNO_3$ solution, which acts as a reservoir for the reactants in Equations 3.1 and 3.2. As the silver deposits on the surface, the surface visibly darkens, leading to a reduction in the amount of light transmitted through the thin films or reflected from the polycrystalline samples [2].

3.2.1 Experimental Setup at DuPont

At DuPont, the photochemical activity and reaction rates were measured using a procedure first described by Fleischauer et al. [2]. The procedure at DuPont differed from the original procedure described by Fleischauer et al. [2] because it was performed in a microscope instead of a UV-visible spectrophotometer. The sample was placed on a glass microscope slide with the side to be tested facing up. The sample was then covered with a solution of 0.1 N $AgNO_3$ contained by an O-ring and a glass cover slip. This was placed on the microscope stage in the field of view, and the top surface of the sample was put into focus. UV illumination was provided by an unfiltered, 100 W high-pressure mercury lamp mounted above the sample. The formation of silver was monitored by 550 nm light from a 100 W tungsten lamp, which reflected from the sample surface or was transmitted through the sample to reach a photodetector. Because the UV illumination was dark field, the reflected light from the mercury lamp did not reach the photodetector [3, 4].

3.2.2 Experimental Setup at CMU

Samples were placed in a shallow dish with the side to be tested facing up. The sample was then covered with 0.115 M $AgNO_3$. A tungsten fiber-optic light was placed above the sample and focused to form a spot approximately 5 mm in diameter for times ranging from 5 minutes to one hour. The experimental setup was shielded from other sources of light to prevent reactions from occurring on the portion of the samples that were no directly illuminated by the fiber optic light.

3.2.3 Thin Film Rutile

The $TiO_2\{011\}$, $TiO_2\{010\}$, and $TiO_2\{001\}$ thin films were tested for photocatalytic activity both at CMU and at DuPont.

Two separate experiments were done at CMU. In the first experiment, part of the {001} oriented rutile thin film was masked before the experiment. The film remained illuminated in 0.115 M $AgNO_3$ for 47 minutes. In the second experiment, the {011} and {010} oriented thin films were broken into several pieces. A piece of each film acted as a control and was submerged in 0.115 M $AgNO_3$ with no illumination. Another piece of each film was submerged in 0.115 M $AgNO_3$ with illumination. All films remained in solution for 40 minutes. After being taken out of solution, the four films were ultrasonically cleaned in distilled water for 30 minutes and dried in air at 393 K.

The experiments on thin films at DuPont followed the procedure outlined in §3.2.1. The thin film samples were covered in a 2.5 mm deep solution of 0.1 N $AgNO_3$ contained by an O-ring and a glass cover slip. The formation of the silver was monitored by 550 nm light from a 100 W tungsten lamp that was passed through the sample from the bottom without the use of a condenser lens, through the 20× objective lens, and then through a second 550 nm interference filter before impinging on the photodetector. The transmitted light was recorded at 0.1 s intervals, and data collection was continued until the transmittance dropped to 98%. These data were converted to optical density (OD) versus time using Equation 3.3:

$$\mathrm{OD} = -\log\left(\frac{\mathrm{T}}{\mathrm{T}_0}\right) \tag{3.3}$$

where T is the current transmittance and T_0 is the initial transmittance. The relative photochemical reaction rates were calculated as the slope of the OD versus time plot for the time interval necessary to reach 99% transmittance. For each sample, at least two different areas of the TiO_2 surface were used to determine the photochemical reaction rate.

The quantum yield was calculated as the number of silver atoms produced by Ag^+ photoreduction divided by the total number of photons absorbed. The total number of photons absorbed was calculated by multiplying the number of photons absorbed per second by the exposure time. The number of photons absorbed per second was calculated using the absorption coefficients of the applicable rutile orientations, the film thickness, and the incident light intensity. Corrections were made for the reflectance from the cover glass-air and TiO_2-water interface.

The total volume of silver reduced on the films was calculated from the size and distribution of silver particles on the TiO_2 surfaces, measured using atomic force microscopy (AFM). The volume was measured in three to five different areas on each sample, and it was assumed that that these observations were representative of the entire surface. The dimensions of 5–10 representative silver islands in each area were measured and used to compute an average volume under the assumption that the islands were right cylinders or parallelepipeds with right angles, depending on the surface. Finally, the total amount of silver deposited was determined by assuming that each island had the density of silver metal.

3.2.4 Polycrystalline Rutile

All polycrystalline results in this thesis are from polycrystals tested at DuPont. The experiments at DuPont followed the procedure outlined in §3.2.1. Polycrystalline samples were covered in a 5 mm deep solution of 0.1 N $AgNO_3$ contained by an O-ring and a glass cover slip. The formation of the silver was monitored by 550 nm light from a 100 W tungsten lamp that was reflected from the top of the sample through the 20× objective lens, and then through a second 550 nm interference filter before impinging on the photodetector. The reflected light was recorded at 1 s intervals, and data collection was continued until the reflectance dropped by 6–8%. The formation of metallic silver was apparent by a darkening of the exposed area. Following this treatment, the samples were rinsed in distilled water and dried. All pellets were stored in desiccators before and after reduction experiments.

Before an experiment could be repeated, previously deposited silver had to be removed by heating the pellets to 473 K for four hours to oxidize the silver. The silver oxide was then removed by dissolving it in 0.5 M NaOH. Soaking the pellet for four hours in 0.5 M NaOH in an ultrasound removed the visible silver but had no other visible effect on the surface.

The amount and distribution of silver on polycrystalline samples were determined using AFM by counting silver particles in a 4–25 μm^2 area.

3.3 Sample Characterization

3.3.1 Backscattered Laue Diffractometry

The relationship between the thin film orientation and the substrate orientation was determined at DuPont using x-ray diffraction [5]. Laue patterns of samples tested at CMU were used to determine the substrate orientation. The thin film orientations were then inferred based on the previous work [5]. The experimental Laue patterns were indexed by comparing them to calculated patterns produced by the commercial software application Desktop Microscopist by Virtual Laboratories, Inc. Table 3.2 lists the epitaxial relationships needed to orient the rutile films, and Figure 3.1 shows representative experimental and calculated Laue diffraction patterns for $Al_2O_3\{0001\}$.

Table 3.2: Epitaxial Relationships for Rutile Thin Films on Sapphire [5]

Rutile Film	Al_2O_3 Substrate	Epitaxial Relationships	Lattice Mismatch
(010)	(0001)	$[100] \parallel [\bar{2}110]$	3.76%
		$[001] \parallel [01\bar{1}0]$	7.27%
(011)	$(11\bar{2}0)$	$[0\bar{1}1] \parallel [\bar{1}100]$	0.91%
		$[100] \parallel [0001]$	5.78%
(001)	$(10\bar{1}0)$	$[100] \parallel [1\bar{2}10]$	3.6%
		$[010] \parallel [0001]$	5.72%

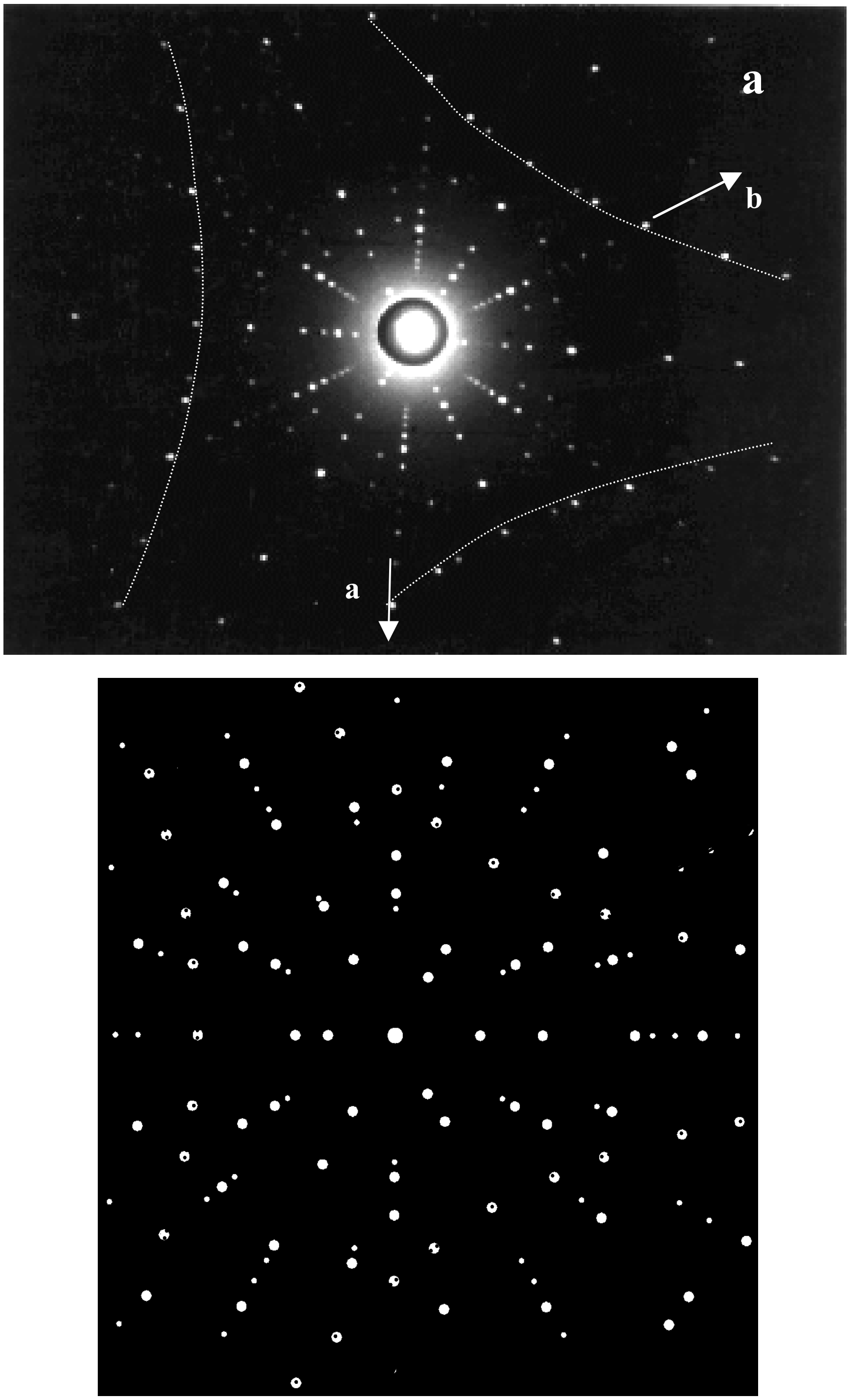

Figure 3.1—a) A backscattered Laue pattern from {010} rutile grown on Al_2O_3{0001}. The pattern shows the symmetry of the underlying substrate.
b) A calculated backscattered Laue pattern of Al_2O_3{0001}.
The two patterns are oriented identically; however, there is not a one-to-one correspondence between the spots in each because of limitations in the computer program to show faint diffraction spots. The dotted arcs in each image indicate the positions of the hyperbolas and clearly illustrate the 3-fold symmetry.

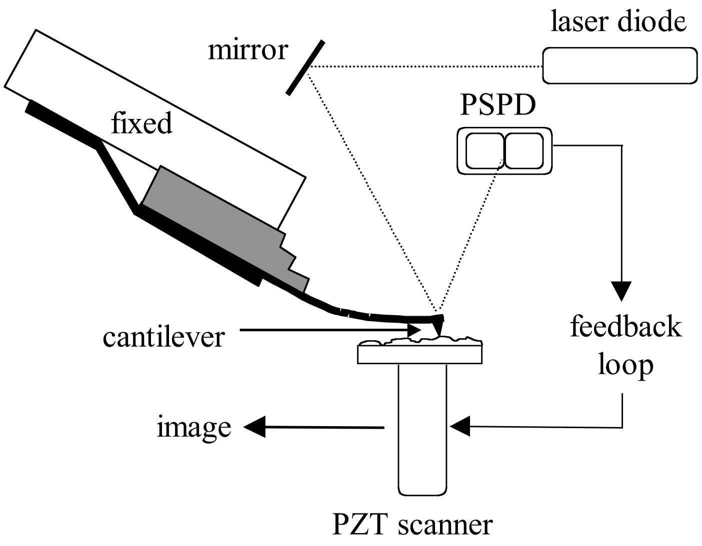

Figure 3.2—A schematic of an atomic force microscope (AFM) [6].

3.3.2 Atomic Force Microscopy (AFM)

Atomic force microscopy (AFM) was used in this thesis to measure the size and general shape of the crystallites in the polycrystals, to map the facet structure of the rutile thin films and the individual crystallites in the polycrystal, and to measure the number of silver deposits on the surfaces of the thin films and the crystallites in the polycrystal.

3.3.2.1 Theory and Basis of Operation

The atomic force microscope (AFM) (see Figure 3.2) records surface topography by rastering a small probe across the surface [6]. The probe is either a sharp Si cone or Si_3N_4 pyramid with a radius of curvature less than 250 Å and is attached to a cantilever of the same material; the cantilever has a low force constant (0.07 N/m to 0.47 N/m) to avoid damaging the sample [7]. Therefore, the small forces felt by the probe deflect the cantilever. The deflection is sensed by monitoring changes in the position at which a laser beam, reflected from the back side of the cantilever, illuminates a position-sensitive photodetector (PSPD). The changing positions of the reflected beam on the detector lead to changing outputs from different segments of the PSPD. In constant force mode, the vertical position of the sample is continuously adjusted to maintain a constant output from the PSPD, i.e. to maintain a constant beam deflection or force, so the probe maintains a constant height above the local topography. In constant height mode, best used in atomic-scale imaging of very flat surfaces, the change in the PSPD output, or beam deflection, is used as a direct measure of topographical features, so the height of the cantilever with respect to the stage is kept constant regardless of the height of the topographical features being scanned. Images presented in this thesis were obtained in constant force mode.

Constant force AFM images are displayed as topographs. Feature heights are displayed as a gray scale with white features being the highest and dark features being the lowest. The gray scale is distributed uniformly over the height range in the image, which mutes small-scale variations in height when very tall or deep features are present on the surface. To better see these small-scale height variations, it is possible to simultaneously record the difference between the set-point deflection and the actual deflection experienced by the cantilever while recording a topograph. This error, or deflection, image emphasizes changes in topography rather than absolute heights. Although the computer adjusts the height of the sample to maintain the deflection at the set-point in constant height mode, there is still an error signal because of the finite time that exists between the deflection and the correction. Unlike topographs, the deflection image shows sudden changes in height as black (for decreases in height) and white (for increases in height) areas while the majority of the image is gray. Deflection images provide evidence of the existence of small-scale features by showing the sudden change in height which occurs when the cantilever comes into contact with the features; they do not provide quantitative information about the heights of surface features. However, deflection images in conjunction with topographic images can provide almost all the accessible topographic information about the surface.

3.3.2.2 Non-Contact AFM (NC-AFM)

Non-contact AFM provides similar information to contact AFM; however, the surface is imaged using the attractive part of the Van der Waals force instead of the repulsive part. In NC-AFM, the cantilever is vibrated with a frequency slightly higher than its natural resonance frequency [7]. When the cantilever is close enough to the surface of the material being examined, the attractive force between the probe and the surface changes the resonance frequency of the cantilever, causing a large decrease in the vibrational amplitude. The feedback mechanism, similar to that used in contact AFM, now detects changes in vibrational amplitude instead of changes in deflection and modifies the height of the sample in order to maintain constant vibrational amplitude. The changes in height needed to maintain a constant vibrational amplitude are used to generate a topograph.

The cantilevers used in NC-AFM have different properties than those used in contact AFM [7]. In contact AFM, ideal cantilevers are long and thin so that smaller forces are required to deflect the cantilevers, causing less damage to the surface. Longer cantilevers also allow the heights of smaller features to be recorded more accurately because the deflections are more exaggerated than with short cantilevers. In NC-AFM, however, short, thick cantilevers with high force constants (9–25 N/m) are preferred in order to prevent the probe from contacting the surface. Contact occurs when the Van der Waals forces are stronger than the cantilever can withstand, causing the probe to hit the surface and generating sharp, triangular-shaped spikes in the images. Stiffer cantilevers with high force constants also have a higher resonance frequency than softer ones, producing more stable images.

3.3.2.3 Interpretation of Images

In almost all ways, the interpretation of large-scale contact AFM and NC-AFM images is straightforward. However, caution is required if the features being imaged are the same size as or smaller than the radius of the probe. If the feature protrudes from the surface, it can image the probe, and although the placement of the features will be consistent with the true surface, the imaged shape will reflect the shape of the probe, not the shape of the feature. If the feature is a small, deep void or hole, its depth cannot be accurately measured because the probe is wider than the hole. In general, the sides of steep features cannot be measured accurately because the finite aspect ratio (ratio of probe length to width) prevents the tip of the probe from touching the sides of steep features before the probe's sides do. These probe-surface convolution effects potentially influence several of the experiments described in this thesis. The possible impact of probe-surface convolutions will be described on a case-by-case basis in the relevant parts of this thesis.

3.3.2.4 Experimental Equipment and Procedure

Contact and NC-AFM measurements were made under ambient conditions with a Park Scientific Instruments (PSI) Autoprobe CP. Gold coated Si cantilevers with conical Si probes with radii of curvature less than 100 Å were used for both contact and NC-AFM. The cantilevers used for contact AFM have a force constant of approximately 0.16 N/m while the cantilevers used for NC-AFM have a force constant of approximately 18 N/m and a resonance frequency of approximately 360 kHz.

Initially, contact AFM with moderate forces was used for all thin film and polycrystalline sample images. However, after silver reduction experiments began, it was discovered that the force exerted by the probe was removing the silver oxide layer which formed on the silver particles. As time elapsed and more of the silver was oxidized, whole silver particles were being gradually scraped from the surface, making it impossible to accurately determine the amount and distribution of silver on the surface. Since the smaller particles were completely oxidizing within two or three hours, images could not be made quickly enough to allow contact AFM to be used unless very low forces were used. However, it was found that if the force were minimized, silver particles could be imaged reproducibly without degradation. Therefore, all recent images were made using contact AFM with the minimum necessary contact force.

3.3.2.5 Errors in Geometric Measurements

The error in measuring distances in the x- and y-direction was determined to be approximately 5% based on measuring the distances between grid lines known to be 10 μm apart and using a 20 μm scan with the same scan parameters as the data. The error in measuring distances in the z-direction is known to less precision but is less than 10%.

3.3.3 Orientation Imaging Microscopy (OIM)

Orientation imaging microscopy was used to index the orientations of the crystallites in the polycrystals.

3.3.3.1 Theory and Basis for Operation

Orientation imaging microscopy (OIM) automatically indexes electron backscattered diffraction (EBSD) patterns obtained using a scanning electron microscope [8]. As the schematic in Figure 3.3 shows, a finely polished sample is held at a steep angle to the electron beam. As the electrons penetrate the sample, they are diffracted, or backscattered, from the planes that meet the Bragg condition. Because the electrons scatter inelastically from the crystal, a wide range of wavelengths are available, and all planes meet the Bragg condition. The backscattered electrons strike a phosphor screen connected to a high gain intensified silicon, intensified target (ISIT) video camera, creating a diffraction pattern similar to a Kikuchi pattern in which the bands represent planes and the intersections of two or more bands represent zone axes. The image is digitized, and background noise, in the form of a backscattered electron pattern taken over many grains, is subtracted from the image. A Hough transform of the image is then used to automatically locate the band edges. The angles between bands are calculated and compared to a database including unit cell and diffraction intensity data for the material being examined. The angles are then used to identify the normal to the surface being examined. The beam is then moved to the next location, and the procedure is repeated. Orientations can be determined within approximately 5° for undeformed materials, while misorientations can be determined within approximately 1° for undeformed materials. Grain boundaries were delineated when changes in orientation greater than 5° occur.

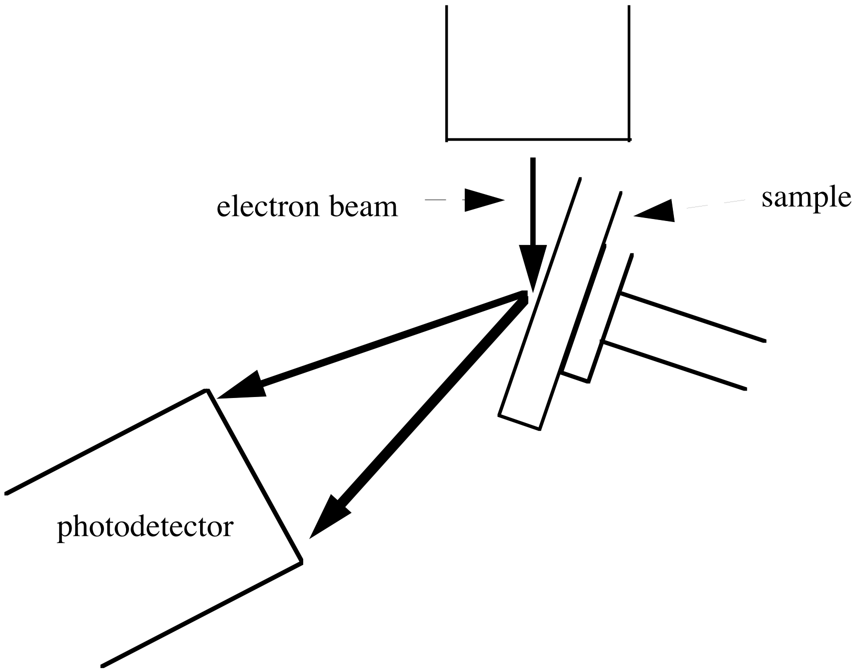

Figure 3.3—Schematic of orientation imaging microscope (OIM).

Figure 3.4a shows several representative images of diffraction patterns from single crystals of rutile. These images form a map of the orientation space for rutile near {001}. Unfortunately, because of the aspherical distortions caused by attempting to map a curved surface onto a flat plane, a clear map of the irreducible portion of orientation space cannot be achieved with these images. Therefore, the schematic drawn in Figure 3.4b shows a much clearer picture of how the major poles are connected in orientation space, although the angles between the bands are not correct. Knowing approximately how different orientations should appear in an EBSD pattern provides a means of double checking the orientations calculated by the OIM.

3.3.3.2 Experimental Details

All OIM data were taken on a Philips XL40FEG SEM controlled by a PC and SGI workstation. The patterns were indexed using the programs OIM2.2 and OIM2.5 written by TSL. The reflections used to index the EBSD patterns are (002), (200), $(1\bar{1}2)$, $(01\bar{1})$, $(21\bar{1})$, $(30\bar{1})$, $(10\bar{1})$, (110), (111), and (310). Accelerating voltages ranged from

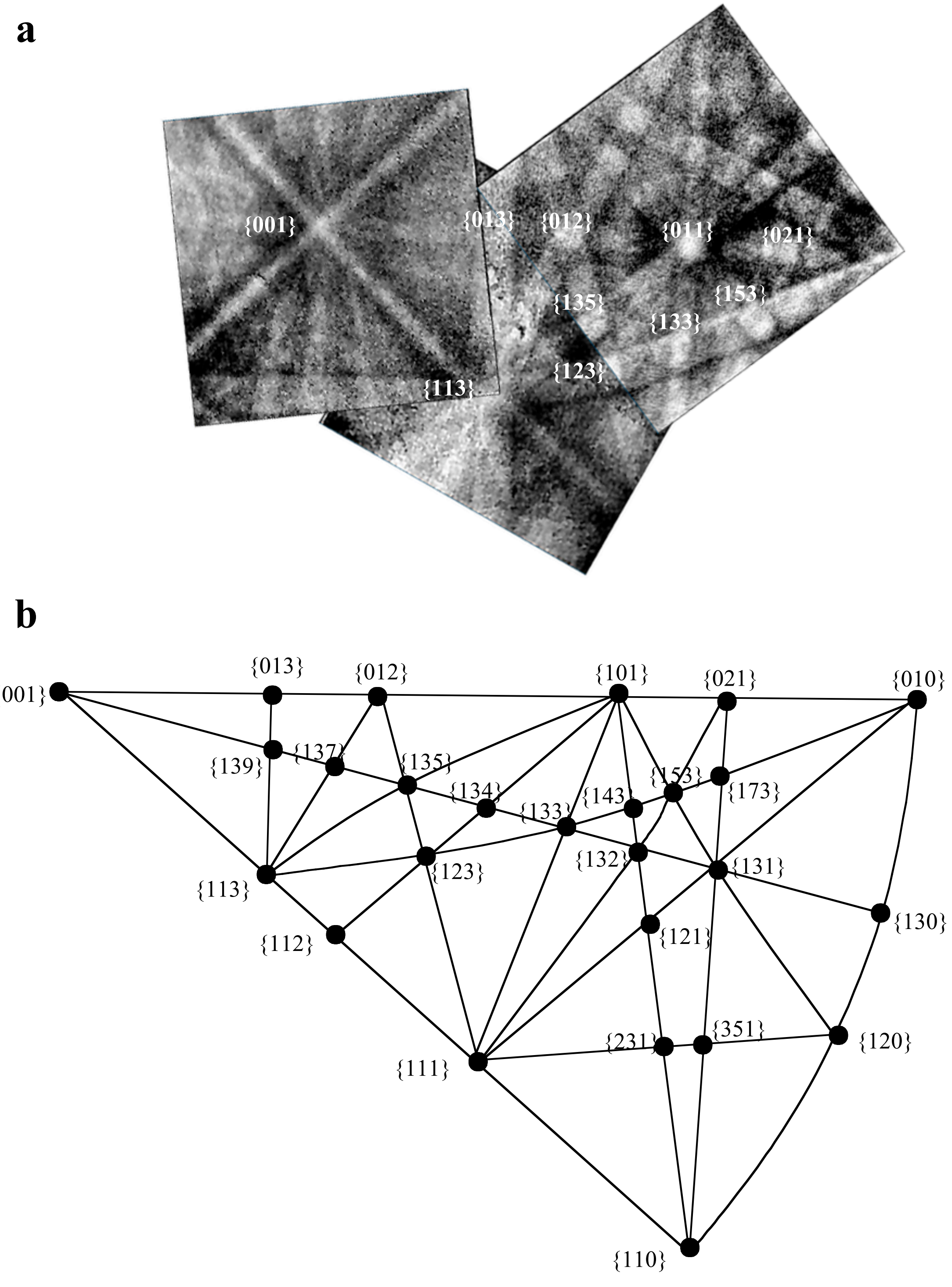

Figure 3.4—a) A map of orientation space near rutile {001} from EBSD patterns. Slight mismatches along the edges of the images are due to aspherical distortions.
b) A schematic of EBSD patterns for the unique portion of orientation space. Several longer bands are curved to make up for spherical distortions.

5–15 kV, and scans were taken with either 16 or 32 frame averaging, a spot size of 5 or 6, and 1–2 μm step sizes.

To reduce the amount of surface charging, the samples were attached to mounts with silver paste. In addition, automatic scans were done only when the number of crystallites to be indexed was fewer than 20. When the number of crystallites to be indexed was greater than 20, the beam was manually placed on each crystallite.

3.3.4 Auger Electron Spectroscopy (AES)

Auger electron spectroscopy was used to measure the surface composition of the rutile polycrystals.

3.3.4.1 Theory and Basis for Operation

Auger electron spectroscopy (AES) measures the composition of a surface on a sub-monolayer level by measuring the characteristic energies of escaping electrons [9]. In an AES experiment, an electron beam strikes the surface of the sample and knocks out core electrons from surface and near-surface atoms. In each atom, an electron from a higher energy band fills the hole, releasing energy equal to the difference between the electron's initial energy level and the ejected electron's initial energy level. In the Auger process, shown in Figure 3.5, the excess energy is released by ejecting a second electron, called an Auger electron, from the atom. The kinetic energy of the Auger electron depends only on the difference between the Auger electron's energy level in the atom, labeled E_2 in Figure 3.5, and the energy released when the core hole was filled, or E_1 - E_c in Figure 3.5, where E_1 is the original energy of the electron that fills the core hole and E_c is the energy of the core electron that was ejected. Because the kinetic energy of the Auger electron depends only on the energy level of the atom from which it escaped, it can be used to identify the atomic species from which it came.

The biggest advantage of AES over other techniques is its sensitivity to submonolayer levels of impurities and its surface specificity. The minimum in the mean free path curve is around 80 eV with a mean free path of approximately 5 Å, and the

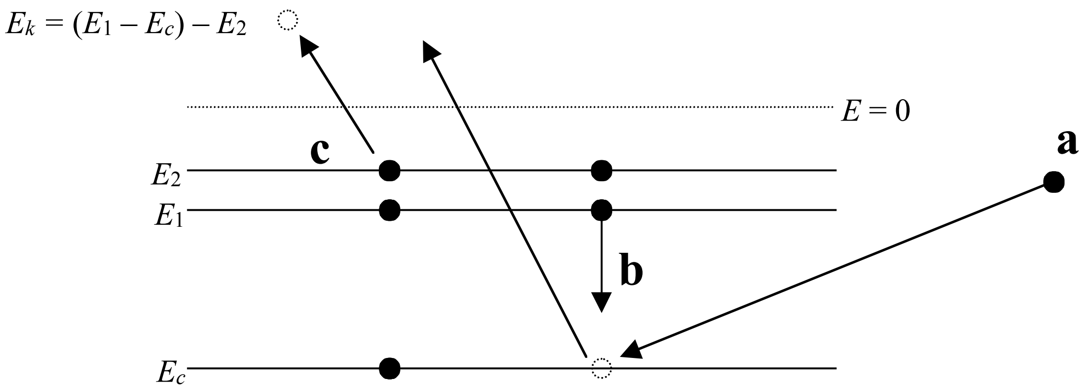

Figure 3.5—A schematic of the Auger process.
a) An electron from the electron beam knocks a core electron out of a surface or near-surface atom.
b) A second electron with higher energy fills the hole left in electron band, releasing energy E_1 - E_c.
c) The excess energy is used to eject a second electron from the atom, which leaves with kinetic energy $E_k = (E_1 - E_c) - E_2$.

mean free path is less than 100 Å for electron energies as great at 10 keV [10]. All Auger transitions of interest yield Auger electrons with energies well below 3 keV [11] and mean free paths below 10 Å [10]. Even greater surface specificity can be gained by only looking at the low energy transitions for atoms with multiple transitions.

3.3.4.2 Experimental Details

All AES data were taken on a Perkin-Elmer PHI 600 Scanning Auger Multiprobe controlled by a Digital pdp11/04 computer with a RX02 disk drive. All spectra were taken with an accelerating voltage of 3 kV. The samples were tilted 50° to the beam direction. To reduce charging, spectra were taken with Ar^+ flowing over the sample.

AES spectra were taken for three photochemically active crystallites and three photochemically inactive crystallites. Figure 3.6 shows the orientations of the 6 crystallites in an inverse pole figure. Photochemically active crystallites are represented as solid circles, while photochemically inactive crystallites are represented as hollow circles. The only impurities detected on each surface were silicon and calcium. A rough comparison of the amounts of silicon and calcium on each of the surfaces can be made

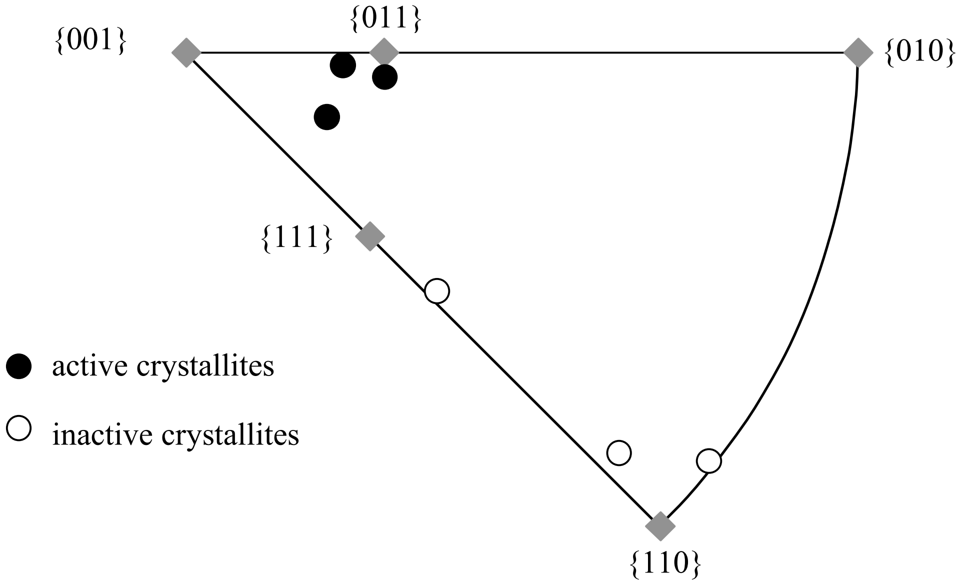

Figure 3.6—The orientations of the six crystallites examined with AES.

using the ratios of the silicon peak height and calcium peak height to titanium peak height, respectively. Table 3.3 lists the average ratios of silicon and calcium peak heights to titanium peak height for the active and inactive crystallites with orientations shown in Figure 3.6. The results indicate that more silicon and calcium exist on the surfaces of the inactive crystallites than the surfaces of the active crystallites. From secondary electron images, it was clear that the calcium and silicon were not distributed evenly across the surface but were concentrated in small particles.

Table 3.3: Relative Amounts of Si and Ca on Active and Inactive Rutile Crystallites

	Si/Ti peak height	**Ca/Ti peak height**
inactive crystallites	0.14±0.02	0.18±0.05
active crystallites	0.05±0.03	0.052±0.009

3.3.5 Energy Dispersive X-Ray Spectroscopy (EDX)

3.3.5.1 Theory and Basis for Operation

The presence of silver on the surface was verified experimentally using energy-dispersive x-ray spectroscopy (EDX). The principles of EDX are almost identical to those of AES [12]. A beam of electrons strikes a sample and removes core electrons from atoms both near the surface and in the interior of the sample. A higher-energy electron in the now ionized atom fills the hole, releasing energy equal to the difference between its original energy and the original energy of the ejected electron. However, instead of the energy being used to eject a second electron, as in the Auger process, the excess energy is emitted as x-rays. As was the case for the Auger electron, the energy of the x-rays depends only on the energy levels of the atom which originally lost the electron, and can therefore be used to identify the species of atoms in the sample.

Because x-rays have longer mean-free paths than electrons, EDX is not a surface specific technique. However, it can be used to identify the silver on the surface of the rutile polycrystals because there is no silver in the bulk of the polycrystals, so any silver signal must be generated from silver reduced on the surface. Figure 3.7a shows a secondary electron image of several rutile crystallites, and Figure 3.7b is a map of the same area formed by EDX showing the locations of high concentrations of silver. It is clear from the secondary electron image that deposits exist on certain crystallites, and these deposits are identified as silver on the map. Figure 3.7c is a plot produced from an analysis of a spot on a crystallite with many deposits, showing the presence of both silver and silicon, while Figure 3.7d is a similar plot from a crystallite with few deposits, showing neither silver nor silicon.

The presence of silicon in the active crystallites and not in the inactive crystallites contradicts the results from the AES experiments, which indicated a higher concentration of impurities on the surface of the inactive crystallites. One possible explanation is that the AES measurements and EDX measurements were taken on different crystallites, which could explain the differences in the silicon concentration measured by the two techniques. The differences could also be due to the different sensitivities of the two techniques to surface contamination. AES is more sensitive to surface composition than

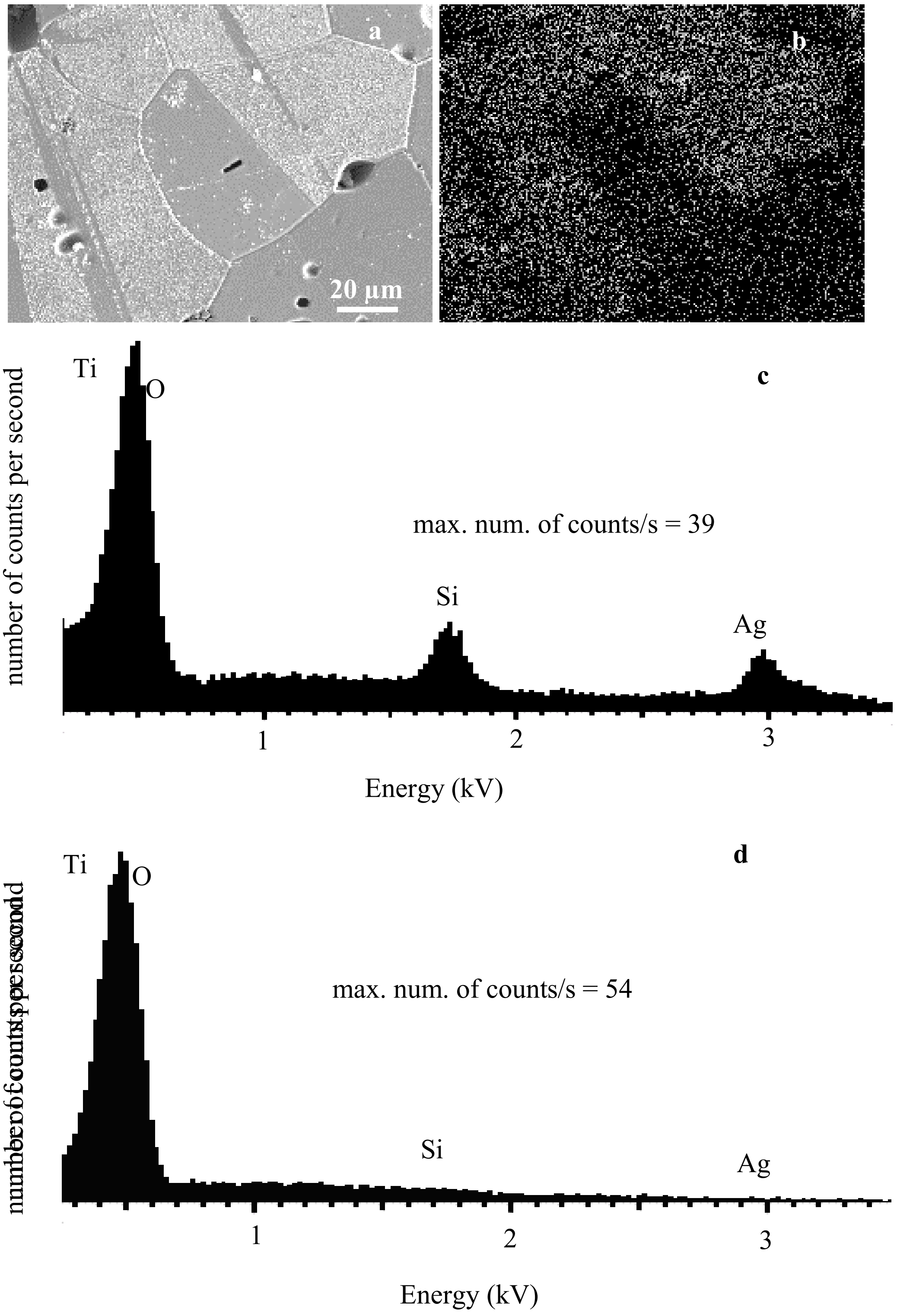

Figure 3.7—a) A secondary electron image of several rutile crystallites.
b) A map of the same area formed by EDX showing the location of high amounts of Ag.
c) A plot produced from an analysis of a spot on an active crystallite, showing Ag and Si.
d) A plot produced from an analysis of a spot on an inactive crystallite, showing neither Ag nor Si.

is EDX, so the AES measurements could reflect a higher surface concentration of silicon and calcium on the inactive crystallites, while the EDX measurements reflect a higher bulk concentration of silicon in the active crystallites. The concentration of silicon in the rutile powder is approximately 40 ppm, while the concentration of silicon in the sintered polycrystals is approximately 100 ppm. This increase in silicon after sintering suggests that the silicon is diffusing into the samples from the furnace. Therefore, assuming that the differences in the results from the two techniques are due to differences in the surface sensitivity, the increased amount of silicon in the bulk of the active crystallites could reflect higher diffusivities along the surface normal for the active crystallites than for the inactive crystallites.

3.3.5.2 Experimental Details

All EDX data were taken on a Philips XL30FEG SEM controlled by two PC's. The accelerating voltage used was 10kV. The data were analyzed using Link ISIS Suite Revision 3.1 written by Oxford Instruments plc.

3.4 Identification of Facet Planes

The orientation of each crystallite can be defined relative to the sample reference system using the three Bunge Euler angles: ϕ_1, Φ, and ϕ_2 [13]. To determine these angles, the sample coordinate system, with axes labeled **X**, **Y**, and **Z**, first lies parallel to the crystallite coordinate system, with axes labeled **a**, **b**, and **c**. The crystal coordinate system is rotated counter-clockwise about **Z** or **c** through the angle ϕ_1. The crystal coordinate system is then rotated counter-clockwise about **a** in its new position through the angle Φ. Finally, the crystal coordinate system is rotated counter-clockwise about **c** in its new position through the angle ϕ_2, leaving the crystallite in its true orientation. The normal to the crystallite's surface depends only on Φ and ϕ_2 while the angle ϕ_1 determines the final in-plane orientations.

Each of the coordinate transformations can be represented as a matrix, and multiplication of the three matrices gives the following matrix which takes a vector defined in the sample coordinate system and transforms it into the crystallite coordinate system:

$$g(\phi_1\Phi\phi_2) = \begin{bmatrix} \cos\phi_1\cos\phi_2 - \sin\phi_1\sin\phi_2\cos\Phi & \sin\phi_1\cos\phi_2 + \cos\phi_1\sin\phi_2\cos\Phi & \sin\phi_2\sin\Phi \\ -\cos\phi_1\sin\phi_2 - \sin\phi_1\cos\phi_2\cos\Phi & -\sin\phi_1\sin\phi_2 + \cos\phi_1\cos\phi_2\cos\Phi & \cos\phi_2\sin\Phi \\ \sin\phi_1\sin\Phi & -\cos\phi_1\sin\Phi & \cos\Phi \end{bmatrix} \tag{3.4}$$

For example, the normal to a crystallite is (001) in the sample coordinate system. To determine (*hkl*), (001) is multiplied by $g(\phi_1\Phi\phi_2)$ to obtain:

$$h = \sin\phi_2 \sin\Phi \tag{3.5}$$

$$k = \cos\phi_2 \sin\Phi \tag{3.6}$$

$$l = \cos\Phi \tag{3.7}$$

These equations yield a unit vector from which the Miller Indices can be easily calculated. For example, in the tetragonal crystal system, Equations 3.5 and 3.6 are multiplied by the *a* lattice parameter, and Equation 3.7 is multiplied by the *c* lattice parameter. After being converted to integers, the resulting (*hkl*) are the Miller indices of the surface normal.

To determine the orientations of a facets on a surface, the normals with respect to the sample coordinate system for every point are calculated for every point on the surface using linear regression. Assuming the standard equation for a plane

$$A(x - x_0) + B(y - y_0) + C(z - z_0) = 0 \tag{3.8}$$

where (x, y, z) are all points on the plane, (x_0, y_0, z_0) is a known point on the plane, and A, B, and C are scalars, the unit normal is defined as

$$\vec{\mathbf{n}} = \frac{(A, B, C)}{\sqrt{A^2 + B^2 + C^2}} \tag{3.9}$$

Rearranging terms and solving for *z*, the height, we get:

$$z = mx + py + q \tag{3.10}$$

where

$$m = \frac{-A}{C} \tag{3.11}$$

$$p = \frac{-B}{C} \tag{3.12}$$

$$q = \frac{Ax_0}{C} + \frac{By_0}{C} + z_0 \tag{3.13}$$

The normal to the plane in terms of *m* and *p* is:

$$\vec{\mathbf{n}} = \frac{(-m, -p, 1)}{\sqrt{m^2 + p^2 + 1}} \tag{3.14}$$

Using the standard linear regression techniques outlined in Appendix A on a three-by-three grid surrounding the point of interest on the surface:

$$m = \frac{\sum_{i=1}^{9} x_i z_i}{6S^2} \tag{3.15}$$

$$p = \frac{\sum_{i=1}^{9} y_i z_i}{6S^2} \tag{3.16}$$

where *S* is the distance between adjacent data points in the x-and y-direction, *i* is the index of the data point in the three-by-three grid, and (x_i, y_i, z_i) are the coordinates of the i^{th} point on the surface, assuming that (0, 0, z_0) are the coordinates of the center point of the grid.

Equations 3.15 and 3.16 combined with Equation 3.14 can be used determine the facet's unit normal defined relative to the sample coordinate system.

$$\vec{\mathbf{n}} = \frac{\left(-\sum_{i=1}^{9} x_i z_i, -\sum_{i=1}^{9} y_i z_i, 6S^2\right)}{\sqrt{\left(\sum_{i=1}^{9} x_i z_i\right)^2 + \left(\sum_{i=1}^{9} y_i z_i\right)^2 + 6S^2}} \tag{3.17}$$

The result from Equation 3.17 is then multiplied by Equation 3.4 to obtain the orientation of the facet's unit normal with respect to the crystal coordinate system. If it is necessary to determine the Bunge Euler angles of the facet, Equations 3.2, 3.3, and 3.4 can be used. These equations were programmed in Java and used to solve for the orientations of all the facets. The program's input is an AFM image and the Euler angles for the surface. All AFM images input into the Java program consisted of 512×512 pixels in order to maximize the amount of data available for analysis, although images with different resolutions may be used.. The program then outputs the Euler angles of any facet the user chooses on the surface. Figure 3.8 shows an example of an AFM image entered into

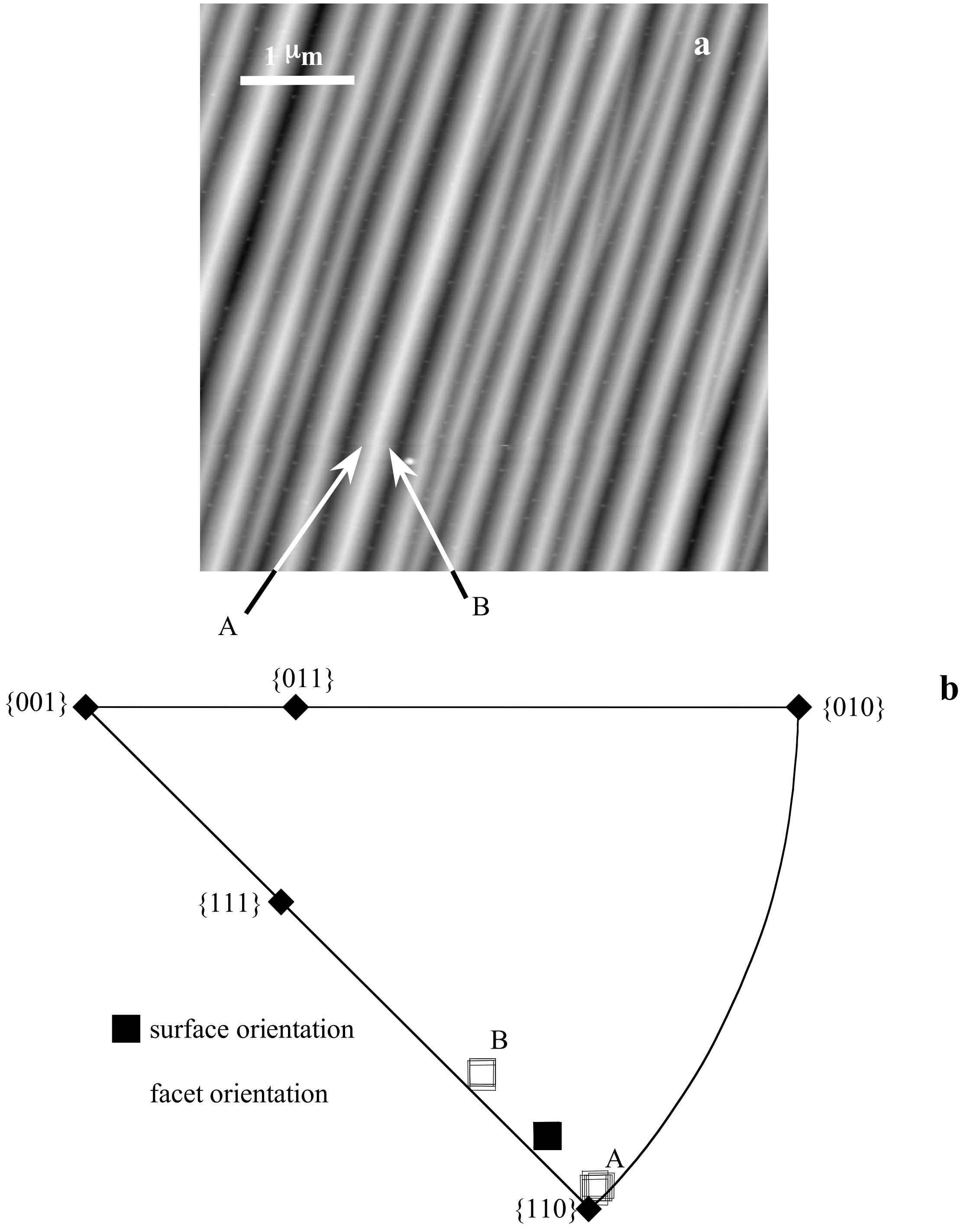

Figure 3.8—a) AFM image of a crystallite annealed at 1273 K for 24 hours.
b) The orientations of the two facets on the surface shown in the AFM image in a).

the computer program and the output of the program once it has been graphed. The surface is oriented approximately 7.4° from {110}, and the orientations of the two facets labeled A and B in Figure 3.8a are shown in the inverse pole figure in Figure 3.8b. There are multiple markers for each facet in Figure 3.8b because of small variations in the slopes of the facets as measured by AFM. As mentioned in §3.3.2.3, probe-surface convolutions, especially near facet intersections, can affect the data recorded by the AFM, and the linear regression technique used to calculate the slopes is sensitive to small changes in pixel position. For this reason, slopes were calculated for all facets at multiple points. The complete program written in Java can be found in Appendix B.

3.5 References

[1] P. Morris Hotsenpiller, G. Wilson, A. Roshko, J. Rothman, and G. Rohrer, *J. Crystal Growth* **166** (1996) 779.

[2] P. Fleischauer, H. Kan, and J. Shepherd, *J. Am. Chem. Soc.* **94** (1972) 283.

[3] J. Lowekamp, G. Rohrer, P. Morris Hotsenpiller, J. Holt, and W. Farnath, *J. Phys. Chem. B* **102** (1998) 7323.

[4] P. Morris Hotsenpiller, J. Bolt, W. Farnath, J. Lowekamp, and G. Rohrer, *J. Phys. Chem. B* **102** (1998) 3216.

[5] P. Morris Hotsenpiller, A. Roshko, J. Lowekamp, and G. Rohrer, *J. Crystal Growth*, **174** (1997) 424.

[6] R. Howland and M. Kirk *in* "Encyclopedia of Materials Characterization: Surfaces, Interfaces, Thin Films", (C. Brundle, C. Evans, Jr., and S. Wilson, Eds.), p85, Butterworth-Heinemann, Boston (1992).

[7] Park Scientific Instruments, AutoProbe CP manual (1995).

[8] S. Wright and B. Adams, *Met. Trans. A*, **23A** (1992) 759.

[9] R. Masel, "Principles of Adsorption and Reaction on Solid Surfaces", John Wiley & Sons, Inc., New York (1996).

[10] C. Brundle *in* "Encyclopedia of Materials Characterization: Surfaces, Interfaces, Thin Films", (C. Brundle, C. Evans, Jr., and S. Wilson, Eds.), p282, Butterworth-Heinemann, Boston (1992).

[11] Y. Strausser *in* "Encyclopedia of Materials Characterization: Surfaces, Interfaces, Thin Films", (C. Brundle, C. Evans, Jr., and S. Wilson, Eds.), p310, Butterworth-Heinemann, Boston (1992).

[12] R. Geiss *in* "Encyclopedia of Materials Characterization: Surfaces, Interfaces, Thin Films", (C. Brundle, C. Evans, Jr., and S. Wilson, Eds.), p120, Butterworth-Heinemann, Boston (1992).

[13] H. Bunge, "Texture Analysis in Materials Science: Mathematical Methods" (translated by P. R. Morris), Butterworths, London (1982).

Chapter 4

Rutile Surface Stability

The surface of a polished ceramic polycrystal with randomly-oriented grains consists of many distinct, high-index surfaces with a high density of broken and distorted bonds. If the energy of the flat surface is much higher than the energy of nearby orientations, the crystallites can facet to increase the coordination of surface ions and to reduce the surface energy. By identifying the facets on the surfaces of crystallites with a wide range of orientations, it is possible to determine the relative stability of different surface planes [1]. In this chapter, the observation of surface facets is used to map the stability of TiO_2 surface orientations at 1473 K and 1273 K.

4.1 Stable Surfaces at 1473 K

Contact AFM was used to examine the facet structure of more than 200 crystallites annealed at 1473 K for five hours. Two types of surfaces were identified as stable with respect to faceting. The first type, an example of which is shown in Figure 4.1, shows no regular surface features and appears flat. The white spots, the largest of which is 127 Å high, are believed to be surface contamination. The second type, an example of which is shown in Figure 4.2a, has a regular array of small surface steps. Such surfaces are vicinal with respect to a stable facet and are also classified as flat. Because there is a continuous distribution of observable step heights from approximately 2 Å to 1 μm, we were forced to make an arbitrary distinction between stepped, vicinal surfaces and faceted surfaces. We selected a critical height at $5\times a_o$, or 23 Å, as the point which separates faceted and stepped, or flat, surfaces. Considering the fact that steps as close as 50 nm are routinely resolved, this implies that orientations within approximately

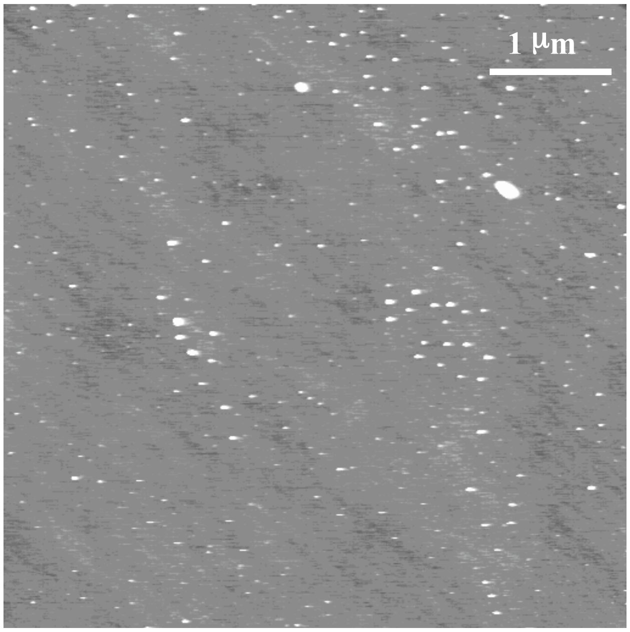

Figure 4.1—An AFM image of a flat surface. The black-to-white range is 30 Å.

3° of a stable orientation may be considered flat. Figure 4.2b shows a line trace perpendicular to the steps on the surface shown in Figure 4.2a. It is clear from this line trace that the maximum step height is less than 20 Å, indicating that, according to the above definitions, this surface is stable with respect to faceting. Figure 4.3 summarizes the information gathered on the stability of the surfaces of 200 crystallites with respect to faceting. In general, surfaces with orientations near {001}, {111}, and {010} appear flat or stepped, signifying that these orientations are stable with respect to faceting. There is also a large region of orientation space, labeled A in Figure 4.3, that is not near any low-index planes but is also stable with respect to faceting.

It is possible that some of the apparently stable regions are flat due to slow kinetics. Although we believe that the kinetics of faceting should be approximately the same for all surfaces, intrinsic anisotropic surface diffusivities or anisotropic surface impurity concentrations may have led to large differences in the kinetics of faceting for surfaces with different orientations. This could have caused surfaces to remain flat that would have faceted if they were annealed for a longer period of time.

There are additional surfaces that are stable with respect to faceting, but these can only be identified by indexing the facets found on the surfaces of crystallites with

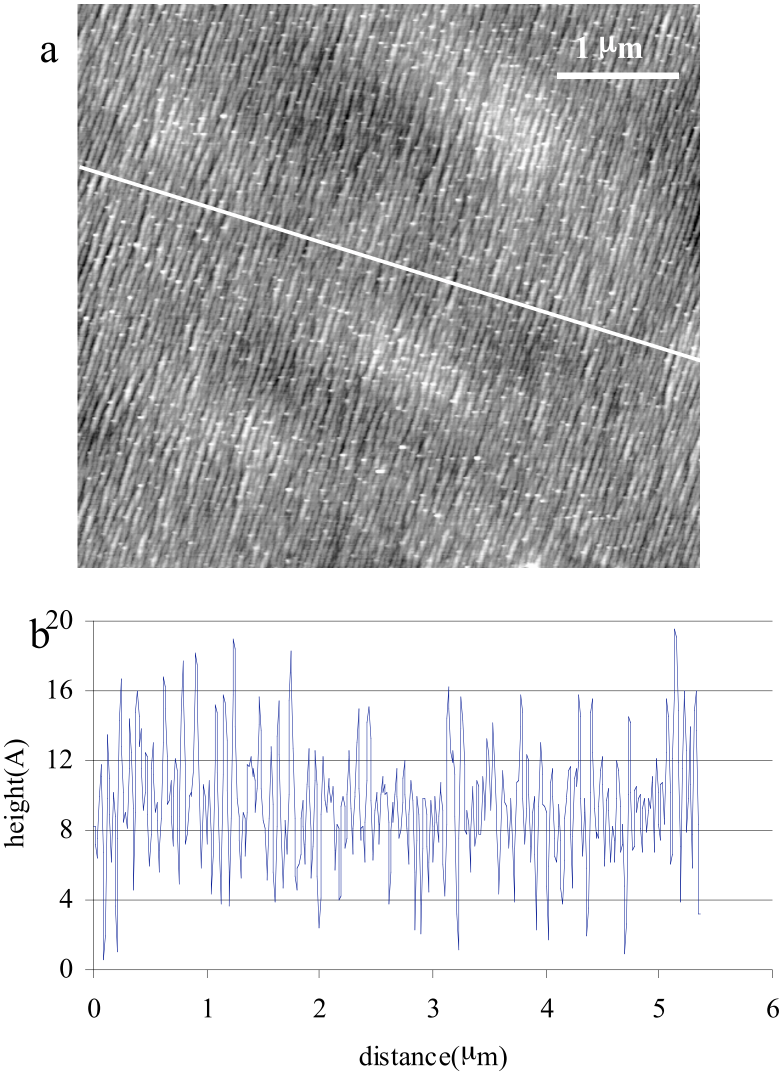

Figure 4.2—a) An AFM image of a stepped surface. The black-to-white range is approximately 30 Å.
b) The height profile of the white line shown in a).

unstable orientations. There is, however, some error introduced by this process. For example, note that while the flat and faceted observations are well-segregated, there is some overlap which is indicative of either limited experimental resolution or possibly non-equilibrium effects. One such limitation is resolution of the procedure used to determine the orientations of the crystallites themselves. As mentioned in §3.3.3.1, the accuracy of the OIM is approximately 5°, so some of the scatter in the data could be due to small errors in measuring the crystallite orientation. The accuracy of the AFM is between 5% and 10%, leading to additional scatter in the data.

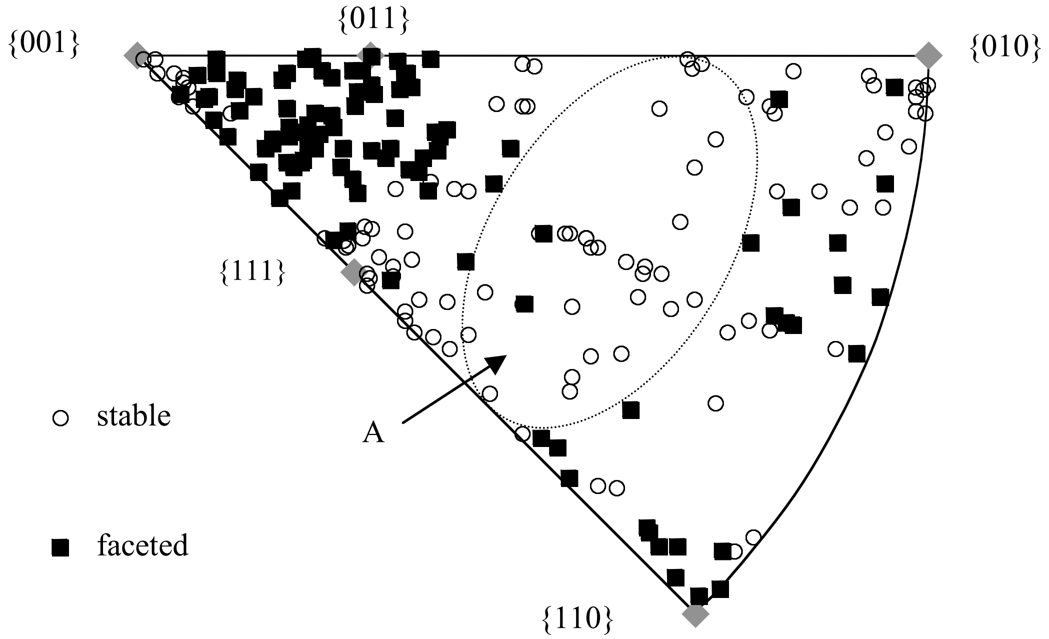

Figure 4.3—An inverse pole figure showing surface stability versus orientation at 1473 K.

Another limitation of the AFM is that it cannot accurately image angles that facets make with the surface if the angles are large. For example, if a feature on the surface is almost normal to the surface, the side of the probe will strike the top of the feature before the probe tip strikes the bottom of the feature, and the angle will reflect the slope of the probe instead of the slope of the surface feature. There are also problems when attempting to image surfaces that are sharply pointed. If the included angle between the planes is sharper than the included angle of the probe, which is 70°, the probe will be imaged by the surface instead of vice versa. In this case, the existence of the facets will be clear, but their shape and included angle will reflect that of the probe. In addition, AFM cannot accurately image three or more facets meeting in an upward point, or pyramid, whose dimensions are approximately the same as the probe's dimensions. In this situation, the tops of the pyramids and the valleys between them will appear rounded. If the sides of the pyramid are large enough, accurate slopes can still be recorded. Otherwise, the data are omitted from future analysis. Finally, in the cases where the presence or absence of faceting on a crystallite surface was different than other crystallites with similar orientations, we assume that the orientation of the outlying crystallite was recorded incorrectly. The data from crystallites that are clearly outliers are omitted from the analysis.

The facets present on the surfaces of the crystallites with unstable orientations were identified using the procedure described in §3.4. By identifying facets in this manner, we found that the {011}, {110}, and a facet with the orientation labeled I in Figure 4.4a were stable in addition to the {001}, {010}, and {111}. Based on the observations, the orientation stability figure shown in Figure 4.4a was constructed following the method originally outlined by Cahn and Handwerker [2]. Considering the definition of a flat surface proposed previously together with the experimental error involved in both EBSP and AFM measurements, the positions of boundaries in Figure 4.4a are expected to be accurate to approximately 5°.

As described in §2.3, the gray areas of Figure 4.4a represent the orientations that are stable with respect to faceting. The diagram clearly shows small areas that are stable with respect to faceting near {111}, {110}, and {001} and a large area that is stable with respect to faceting in the center of the diagram, marked A in Figure 4.3. Unlike Figure 4.3, Figure 4.4a extends over twice the minimum angular range needed to describe all of the unique orientations in a tetragonal system. This extension better shows the presence of the two types of {011} facets on surfaces with orientations near {001}. Figure 4.4b shows one-half of the orientation stability figure together with the individual data points first shown in Figure 4.3 so that the relationship between the experimental data and the experimentally derived orientation stability figure is more obvious. This presentation is intended to illustrate the compromises made when selecting the positions of the boundaries.

A small region is drawn around {011} to represent the orientations that we expect would be flat according to the previous definition of a flat surface. However, we did not find any flat crystallites with orientations near {011} although the data clearly indicate that the {011} surface is stable. The characteristic facet width, defined as the separation between the facet intersection peaks, is approximately 0.2±0.1 μm regardless of the angular separation between the {011} and the crystallite surface. This indicates that the surface steps cluster within the time frame of the experiment instead of remaining widely separated and small. This seems to indicate that the {011} surface is a singular facet; that

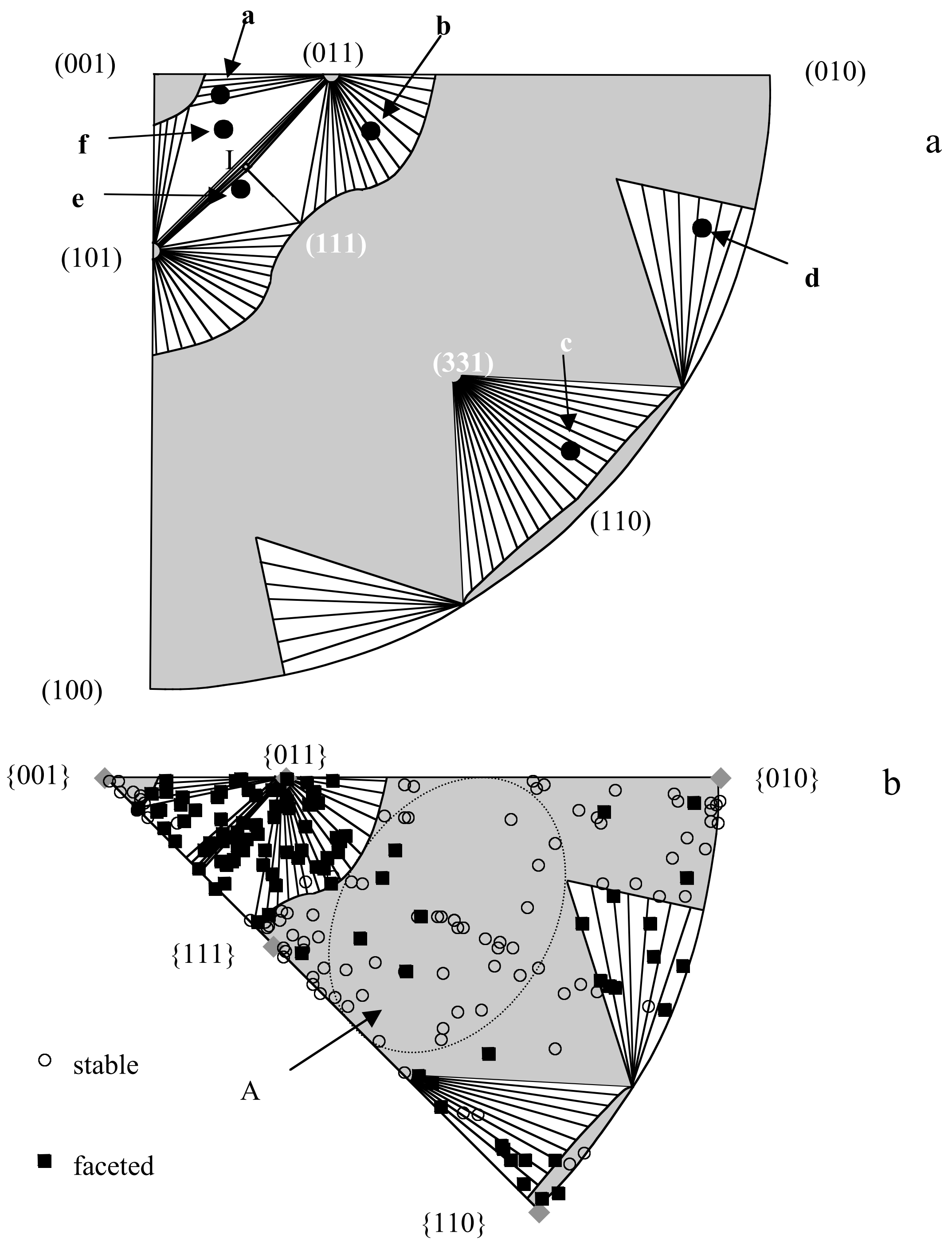

Figure 4.4—a) The orientation stability figure at 1473 K.
b) One-half of the orientation stability figure at 1473 K overlaid with the data used to develop it.

is, all surfaces with orientations close to {011} facet to {011} surfaces, even when the angular separation is small.

No flat surfaces with orientations near I were observed either. The existence of this orientation as a stable surface is somewhat problematic. Previous work by Firment [3] and Poirier et al. [4] found evidence of the stability of {114} at temperatures above 1300 K using low energy electron diffraction (LEED). Using reflection high energy electron diffraction (RHEED), Wang et al. [5] determined that {124} and not {114} was stable after annealing at 1698 K in an oxygen atmosphere. However, the orientation labeled I is much closer to {112} than to either {114} or {124}. Based on nine experimental measurements, the orientation I is only 6±2° from {112}, while it is 15±3° from {114}, 11±3° from {113}, and 10±3° from {124}. Therefore, it is unlikely that experimental error has led to a misidentification of this facet. Assuming that orientation I is a low-index facet, the experimental evidence indicates that it should be indexed as {112}. However, a difference of 6±2° is slightly greater than the error that we expect in the data, so we should consider the possibility that it is a complex facet near {112}.

Unlike the {011} surface, the {110} surface may not be a singular. Surfaces tilted away from {110} in the ⟨001⟩ direction facet into {110} surfaces with only a few degrees of angular separation between the surface normal and {110}. However, based on the orientations of facets that we believe are on the edge of the stability region around {110}, approximately 17° of tilt in the ⟨010⟩ direction are required before faceting occurs. The second facet present on surfaces tilted away from the {110} in the ⟨001⟩ direction has an orientation near {331}.

Surfaces within the same region of the orientation stability figure generally have similar morphologies. Figures 4.5–4.10 show typical examples of morphologies of surfaces from many of the regions in the orientation stability figure. With each of the images is a schematic of the facets and a portion of the orientation stability figure rotated to better match the in-plane orientation of the surface.

Figures 4.5–4.8 show representative images of crystallites with surfaces that consist of two facets. Figure 4.5 shows an AFM image of the surface structure of a crystallite with the orientation labeled **a** in Figure 4.4a. From the schematics next to the AFM image, the orientation of the facet on the left is a complex facet near {001}, and the

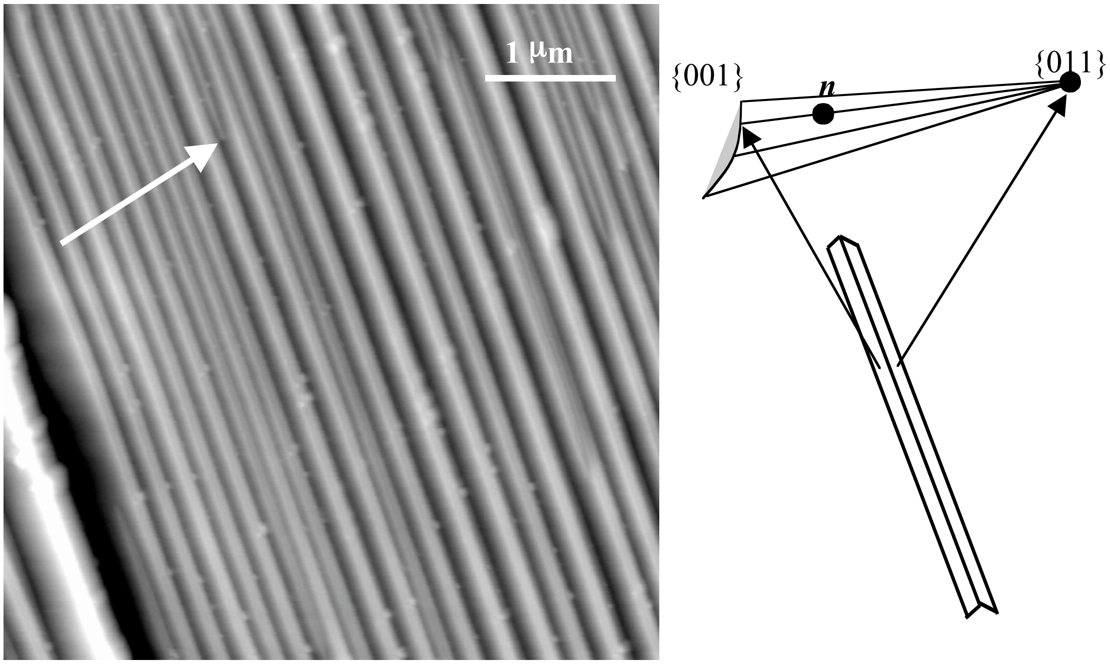

Figure 4.5—An AFM image of the surface with the orientation labeled **a** in Figure 4.4a. The black-to-white range is 600 Å. The arrow points to a facet that disappears into the surface.

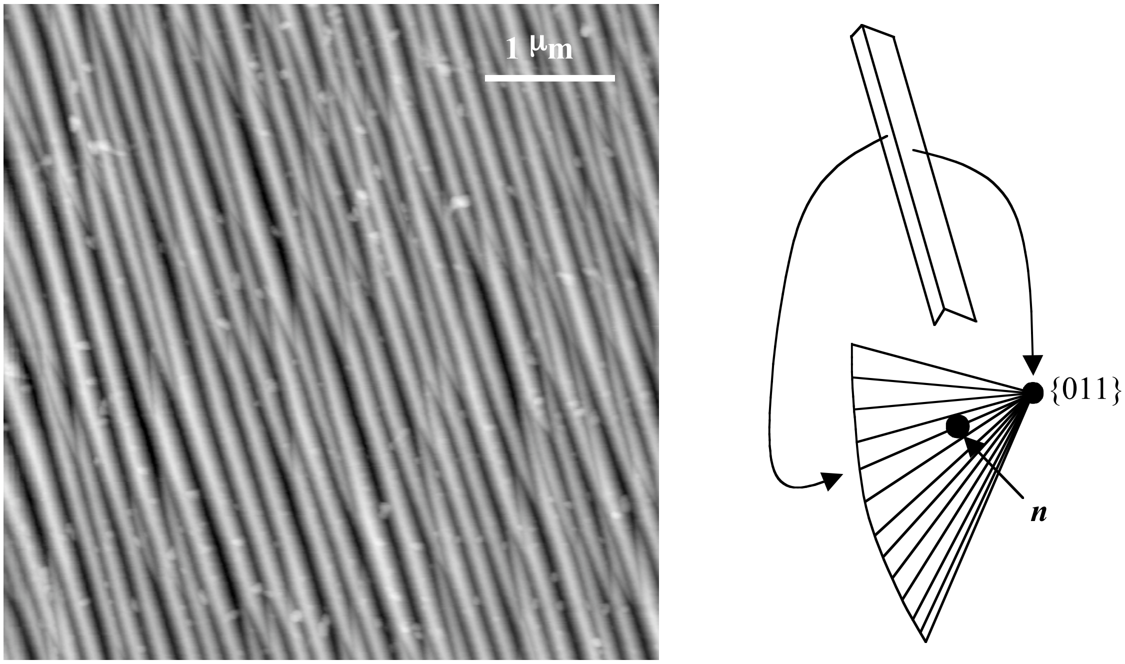

Figure 4.6—An AFM image of the surface with the orientation labeled **b** in Figure 4.4a. The black-to-white range is 370 Å.

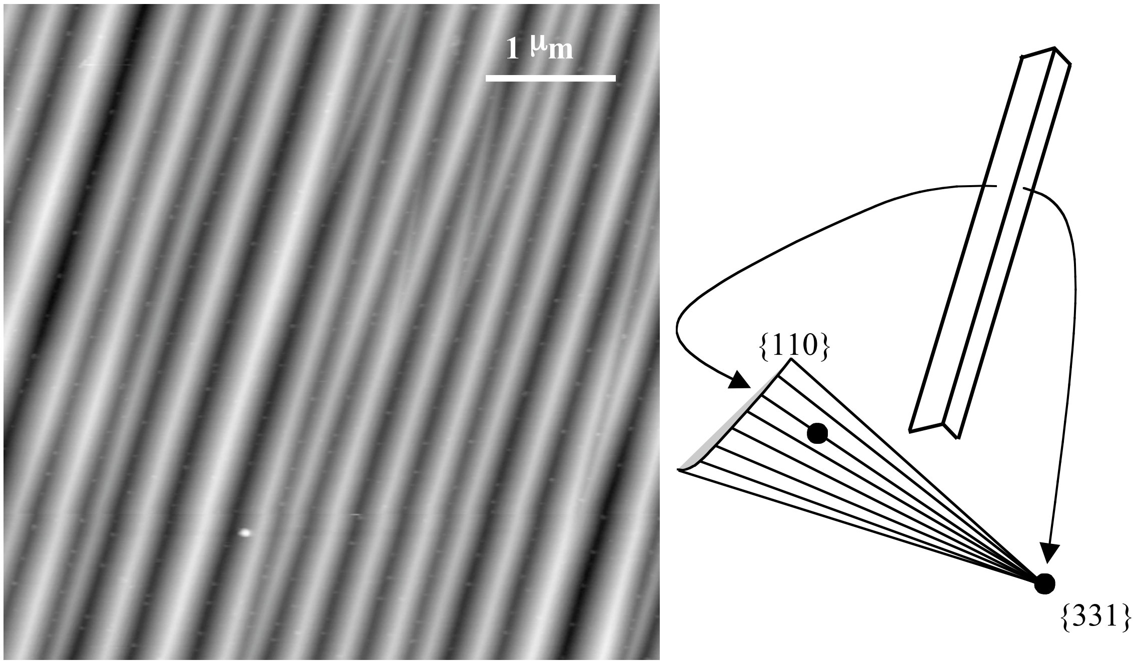

Figure 4.7—An AFM image of the surface with the orientation labeled **c** in Figure 4.4a. The black-to-white range is 486 Å.

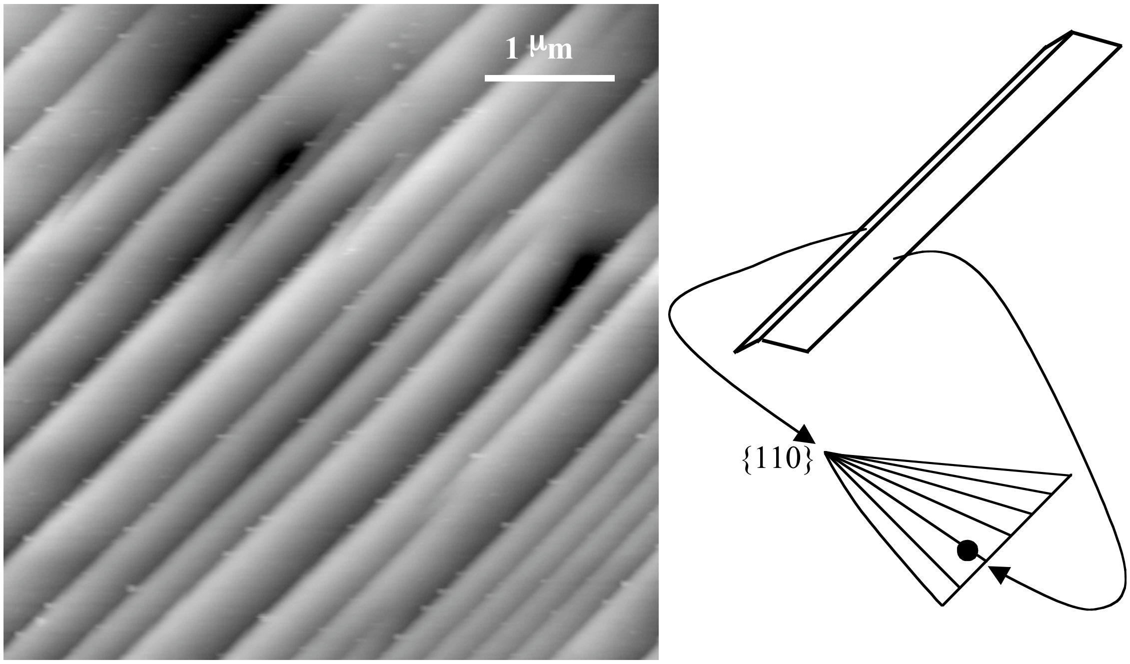

Figure 4.8—An AFM image of the surface with the orientation labeled **d** in Figure 4.4a. The black-to-white range is 355 Å.

orientation of the facet on the right is {011}. Figure 4.6 shows an AFM image of the surface structure of a crystallite with the orientation labeled **b** in Figure 4.4a. As seen in the schematic next to the AFM image, the orientation of the facet whose normal points toward the upper right of the image is {011}, and the orientation of the second facet is complex and lies on the line that defines the stability of {011}. Figure 4.7 shows an AFM image of the surface structure of a crystallite with the orientation labeled **c** in Figure 4.4a. The orientation of the majority facet, whose normal points toward the upper left of the image, is {110}, and the orientation of the minority facet is close to {331}. Figure 4.8 shows an AFM image of the surface structure of a crystallite with the orientation labeled **d** in Figure 4.4a. In this image, the orientation of the facet whose normal points toward the upper left of the image is {110}, and the orientation of the other facet is complex and lies along the line that defines the stability of {110}.

In general, the facets on surfaces that are composed of two facets end by narrowing to a point that disappears into the surface, an example of which is indicated by the arrow in Figure 4.5. The area of each facet on the surface is determined by the overall orientation of the surface. Therefore, if a crystallite's orientation is nearer to the orientation of one of the stable facets than to the other, the area of the facet with the orientation nearest the overall orientation of the crystallite will be greater than the area of the other facet. This effect, if large enough, can be seen with AFM as well as with more precise methods. For example, in Figure 4.8, the area of the complex facet is clearly greater than the area of the {110} facet because the orientation of the surface is much closer to that of the complex facet than to {110}. On the other hand, the width of the facets does not depend directly on the overall surface orientation. While the mechanisms and kinetics of facet formation are incompletely understood, the lateral length scale of the facets will ultimately be limited by the rate of diffusion across the different surfaces, assuming that they form by surface diffusion. Therefore, systematic differences in the facet widths between the different regions of the orientation stability figure where two facets are stable might reveal information about how the surface diffusion coefficient varies with orientation. A close examination of the data, summarized in Table 4.1, shows no trends and therefore suggests that, at this temperature, either the surface diffusivity is

Table 4.1: Facet Widths at 1473 K

area of orientation stability diagram	step width (μm)	number of observations
a	0.3±0.2	5
b	0.3±0.2	14
c	0.3±0.2	7
d	0.3±0.1	4

isotropic within the resolution of currently available data or the morphological evolution is limited by a process other than diffusion.

Figure 4.9 shows an AFM image of the surface structure of a crystallite with the orientation labeled **e** in Figure 4.4a. This surface structure is composed of three facets. The orientations of the three facets are identified in the schematics next to the AFM image. The orientation of the facet whose normal points toward the upper left of the image is the {101}, the orientation of the facet whose normal points to the lower right is the orientation labeled **I**, or {112} in Figure 4.4a, and the orientation of the small facet at the end of each pair is {111}. The orientation of this surface is much further from the orientation of one of the facets that make up the surface, {111}, than from the orientations of the other two, leading to a surface morphology composed of two long,

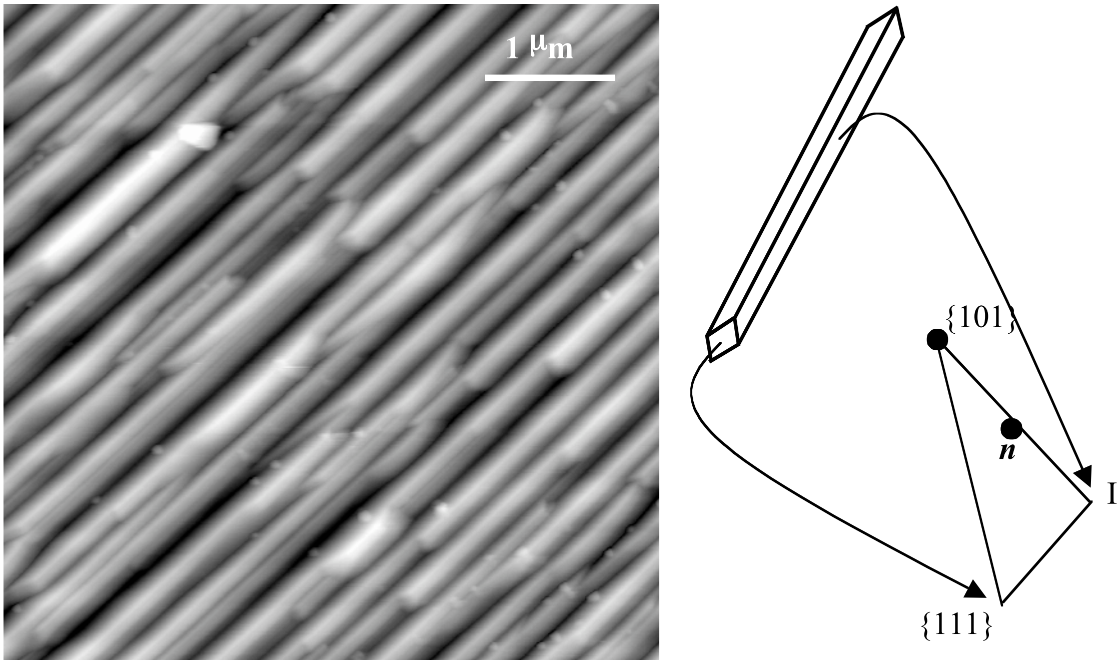

Figure 4.9—An AFM image of the surface with the orientation labeled **e** in Figure 4.4a. The black-to-white range is 516 Å.

narrow facets capped with a third, much smaller facet with the orientation furthest from the orientation of the surface. Similar morphologies are expected for any surface which is significantly closer to two of the three stable facets.

Figure 4.10 shows an AFM image of the surface structure of a crystallite with the orientation labeled **f** in Figure 4.4a. Part of the surface has a faceted structure, consisting of three distinct facets, while the portion of the surface on the left of the AFM image remains flat. The incomplete faceting after eight hours at 1473 K indicates that the approach to equilibrium for some crystallites is slow. Although this is the only image shown with incomplete faceting, the incomplete faceting was not limited to surfaces composed of three facets, nor did all surfaces composed of three facets fail to completely facet. The schematics next to the AFM image exhibit the orientations of the three facets. The facet whose normal points toward the bottom of the image is a complex facet near {001}, and the orientations of the other two facets are {011}. Unlike the crystallite shown in Figure 4.9, the orientation of the crystallite is nearly equidistant from the orientations of the stable facets that make up the surface, leading to a more equiaxed surface structure consisting of upward-pointing pyramids.

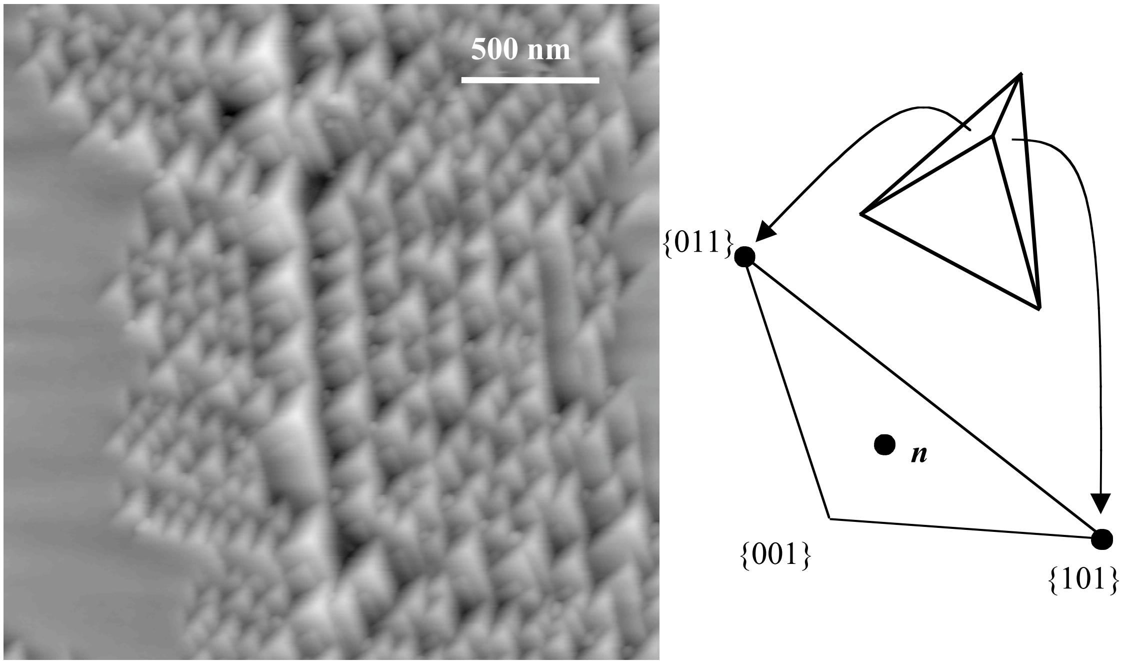

Figure 4.10—An AFM image of the surface with the orientation labeled **f** in Figure 4.4a. The black-to-white range is 567 Å.

4.2 Stable Surfaces at 1273 K

Contact AFM was used to examine the facet structure of 101 crystallites annealed at 1273 K for 24 hours. Figure 4.11 summarizes the information gathered on the stability of the various surfaces with respect to faceting. There are two main places where these observations differ from those at 1473 K. First, surfaces within approximately 5° of {010} that were stable at 1473 K faceted at 1273 K. Second, orientations near {001} that were stable at 1473 K also faceted at 1273 K.

After identifying the orientations of the facets on the surfaces of the crystallites, an orientation stability figure was created for 1273 K, shown in Figure 4.12a. Figure 4.12b shows one-half of the orientation stability figure overlaid with the data from Figure 4.11. The orientation stability figure is similar to the orientation stability figure created at 1473 K. The {011} surface remains a singular facet, and its stability increases somewhat as the orientation is tilted away from {011} toward {010} and {110}. A slightly smaller region around {111} is stable with respect to faceting.

The orientation between {001} and {111}, which was labeled I in Figure 4.4a and was stable with respect to faceting at 1473 K, was not consistently observed at 1273 K. The appropriate region of orientation space is shown enlarged in Figure 4.13. At 1473 K,

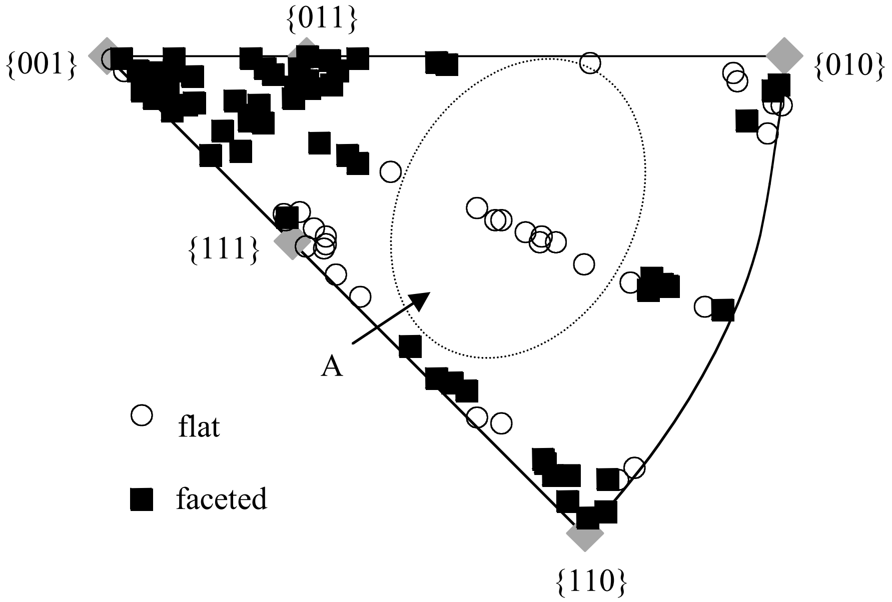

Figure 4.11—Inverse pole figure showing surface stability versus orientation at 1273 K.

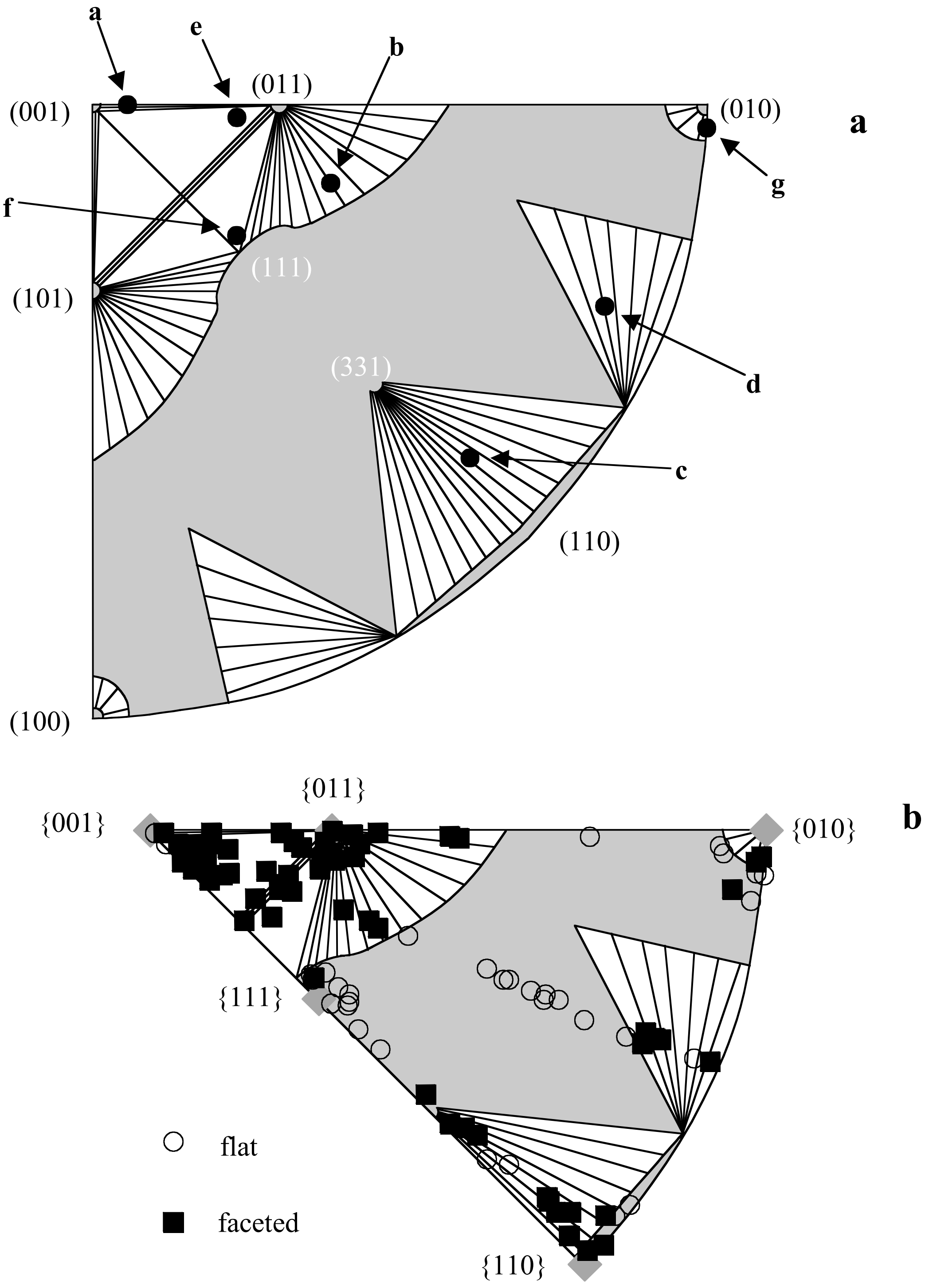

Figure 4.12—a) The orientation stability figure at 1273 K.
b) One-half of the orientation stability figure at 1273 K overlaid with the data used to develop it.

all crystallites in this region are composed of facets with the orientations {011}, {111} and I. At 1273 K, however, only those crystallites with orientations in the white region of Figure 4.13 form facets with an orientation near I. The crystallites with orientations in the gray region, which actually contains orientation I, form facets with the orientations {111}, {101} and {011}. One possible explanation is that (101) facets on a surface with an orientation close to (011) are so small that they cannot be accurately imaged with AFM. As was discussed in §4.1, imaging with AFM has several limitations, one of which is that it cannot accurately image angles that facets make with the surface if the angles are too large. In the range of orientations where the facet with the orientation labeled I seems to appear, the angle between the surface normal and the further {011} plane is generally greater than the angle of the tip's slope, which is about 55° from the plane of the surface. This will lead to measurement errors that could cause the appearance of an extra facet that does not really exist. Since this facet appears on all surfaces at 1473 K, it seems likely that it is either stable or metastable at that temperature and disappears when the temperature is lowered to 1273 K. Whether orientation I is truly stable with respect to faceting at 1473 K or is merely a transition to a more stable state cannot be determined from the present observations.

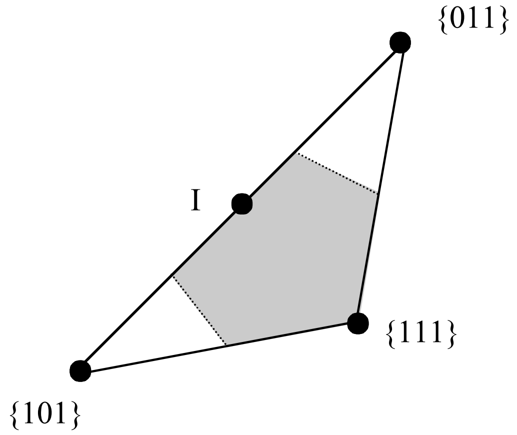

Figure 4.13—The region of the orientation stability figure containing the stability region of facet I at 1473 K. Facets with the orientation I appear in the unshaded regions of the orientation stability figure at 1273 K but not in the shaded regions.

Figures 4.14–4.19 show examples of surface morphologies for orientations from characteristic regions in the orientation stability figure. Next to each image is a schematic of the facets and the portion of the orientation stability figure rotated to better match the in-plane orientation of the surface.

Figures 4.14–4.17 show representative images of crystallites with surfaces that consist of two facets. Figure 4.14 shows an AFM image of the surface structure of a crystallite with the orientation labeled **a** in Figure 4.12a. The schematics next to the AFM image clearly show the orientations of the two facets: the majority facet, whose normal points toward the lower left, is a complex facet near {001}, and the orientation of the minority facet, whose normal points toward the upper right, is {011}. Figure 4.15 shows an AFM image of the surface structure of a crystallite with the orientation labeled **b** in Figure 4.12a. As seen in the schematic next to the AFM image, the orientation of the majority facet, whose normal points toward the lower right of the image, is complex and lies on the line that defines the stability of {011}, and the orientation of the minority facet

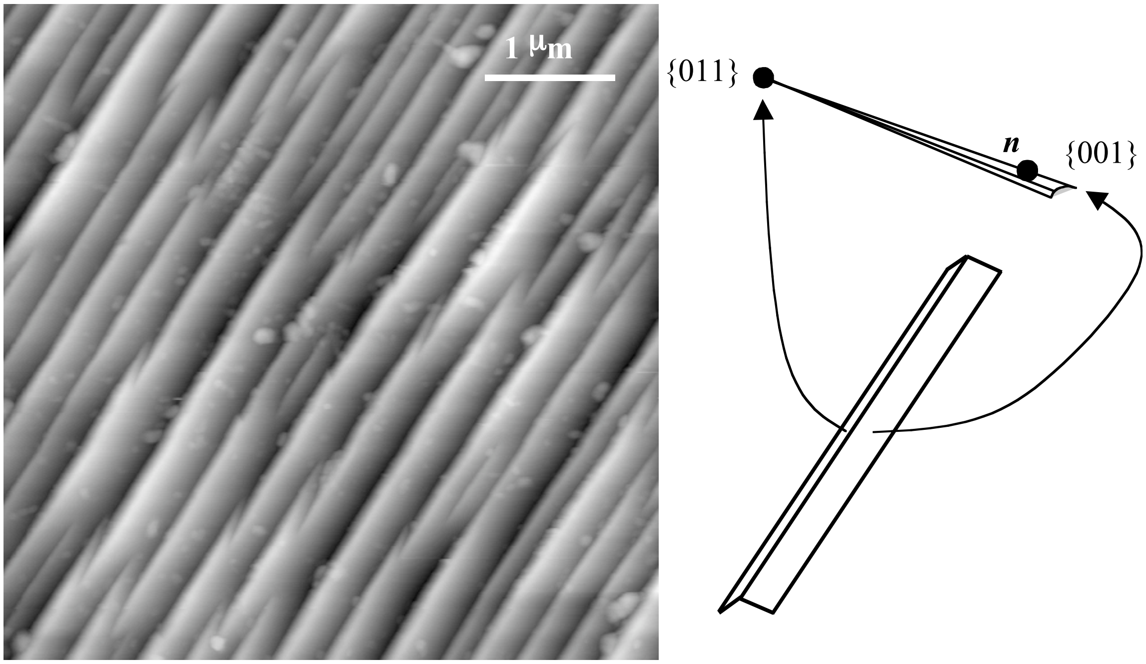

Figure 4.14—An AFM image of the surface with the orientation labeled **a** in Figure 4.12a. The black-to-white range is 670 Å.

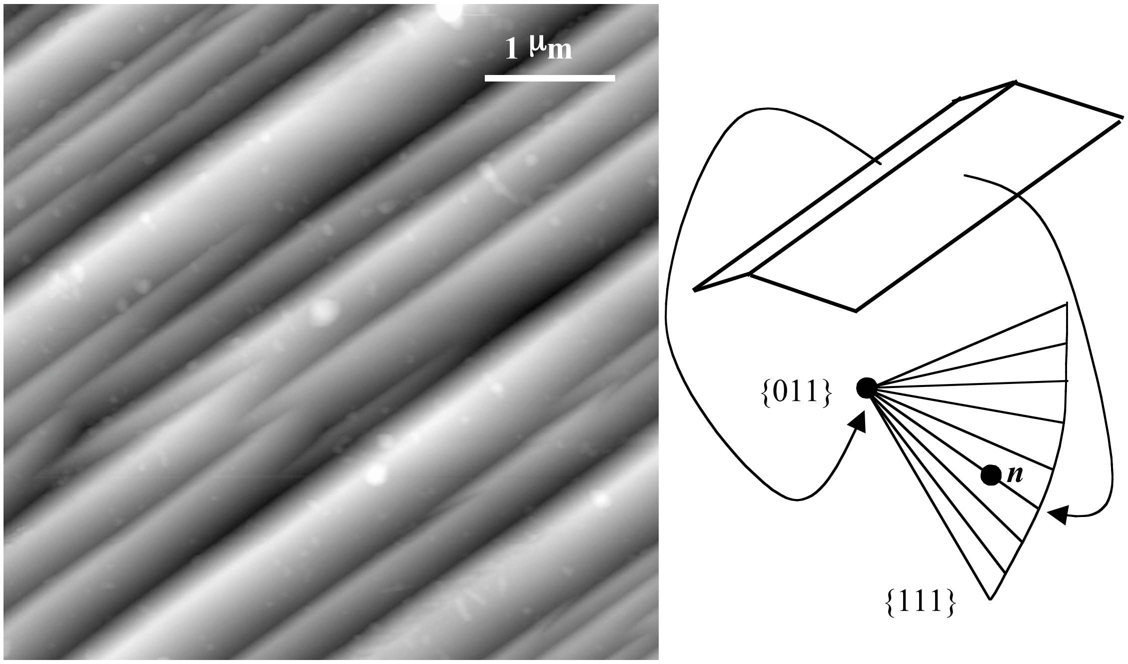

Figure 4.15—An AFM image of the surface with the orientation labeled **b** in Figure 4.12a. The black-to-white range is 1260 Å.

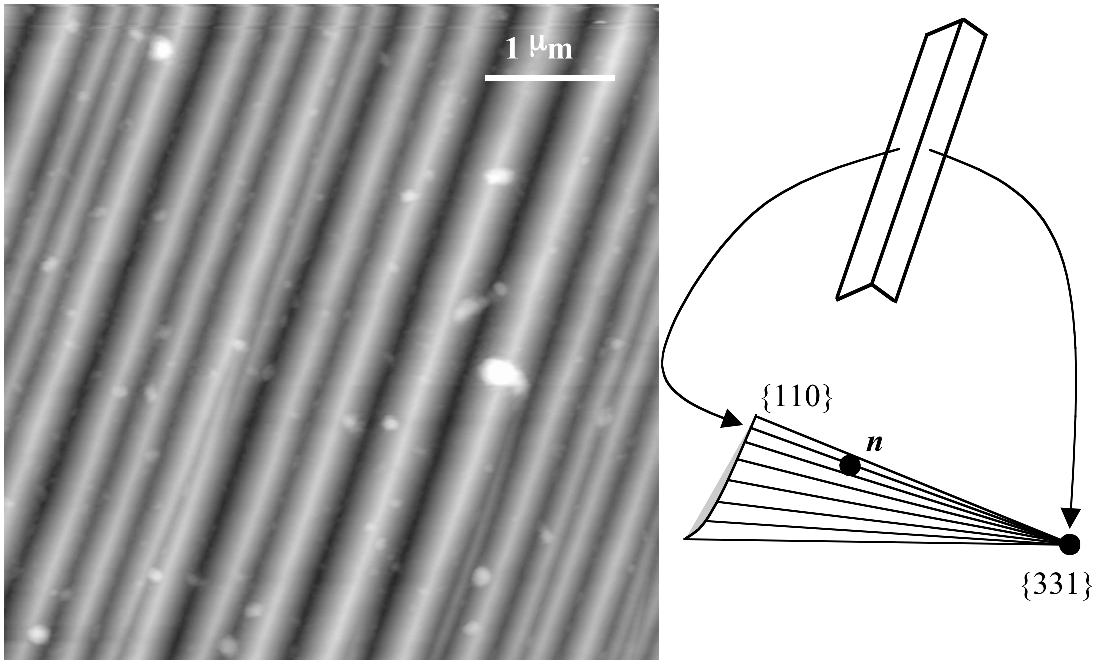

Figure 4.16—An AFM image of the surface with the orientation labeled **c** in Figure 4.12a. The black-to-white range is 630 Å.

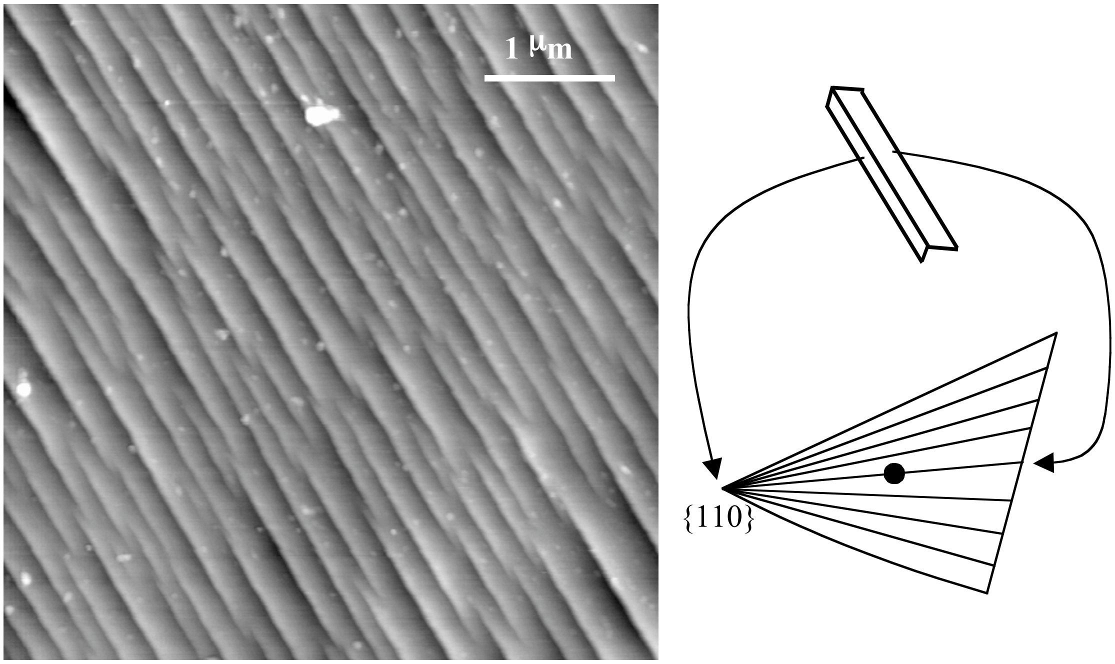

Figure 4.17—An AFM image of the surface with the orientation labeled **d** in Figure 4.12a. The black-to-white range is 310 Å.

is {011}. Figure 4.16 shows an AFM image of the surface structure of a crystallite with the orientation labeled **c** in Figure 4.12a. As the schematics by the AFM image show, the orientation of the majority facet, whose normal points toward the upper left of the image, is {110}, and the orientation of the minority facet is near {331}. Figure 4.17 shows an AFM image of the surface structure of a crystallite with the orientation labeled **d** in Figure 4.12a. The orientation of the facet whose normal points toward the upper left of the image is {110}, and the orientation of the second facet is along the line that defines the stability of the unfaceted region around the {110}.

As discussed in the §4.1, the area of each facet on the surface is determined by the overall orientation of the surface. Therefore, if a crystallite's orientation is nearer to the orientation of one of the stable facets than to the other, the area of the facet with the orientation nearest the overall orientation of the crystallite will be greater than the area of the other facet. For example, in Figure 4.14, the area of the complex facet near {001} is greater than the area of the {011} facet because the orientation of the surface is much closer to the orientation of the complex facet near {001} than to the {011}.

Table 4.2: Facet Widths at 1273K

area of orientation stability diagram	step width (μm)	number of observations
a	0.4±0.2	5
b	0.3±0.2	11
c	0.2±0.1	9
d	0.23±0.05	4

Table 4.2 lists the average facet width for the four regions on the orientation stability figure that are pictured in Figures 4.14–4.17. Unlike the average facet widths on crystallites at 1473 K, the average facet widths at 1273 K seem to change as the orientation changes. The average facet widths in the regions with orientations **c** and **d** seem to be smaller than the average facet widths in the regions with orientations **a** and **b**, possibly indicating that the surface diffusion rate decreases as the angle between the surface orientation and {001} increases.

Figures 4.18 and 4.19 show AFM images of typical surfaces with orientations in regions of the orientation stability figure where three facets are stable. Figure 4.18 shows an AFM image of the surface structure of a crystallite with the orientation labeled **e** in Figure 4.12a. The surface structure is composed of three distinct facets. The schematic

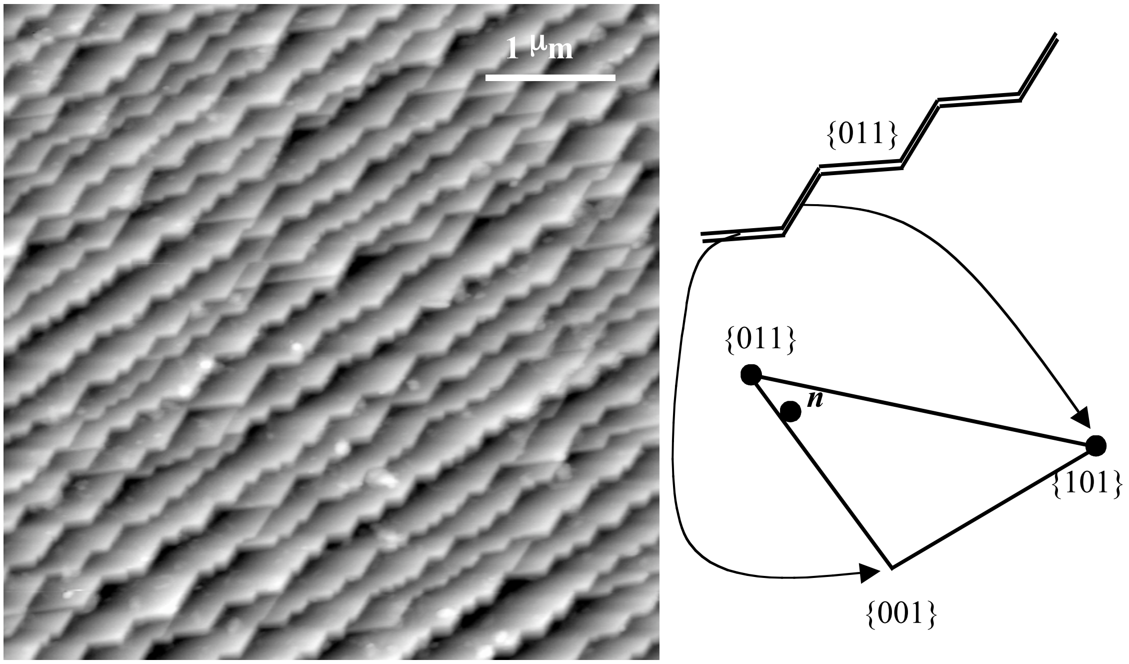

Figure 4.18—An AFM image of the surface with the orientation labeled **e** in Figure 4.12a. The black-to-white range is 695 Å.

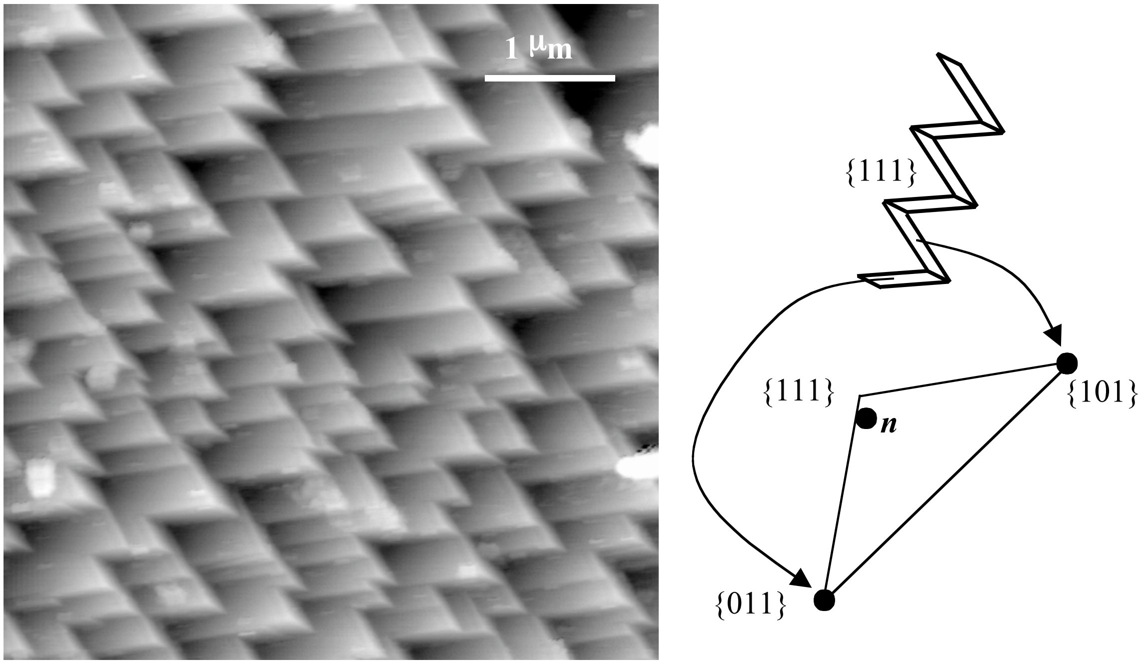

Figure 4.19—An AFM image of the surface with the orientation labeled **f** in Figure 4.12a. The black-to-white range is 1000 Å.

next to the AFM image reveals the orientations of the three facets. The orientation of the majority facet is {011}, the minority facet, whose normal points toward the bottom of the image, is a complex facet near {001}, and the orientation of the other minority facet is {101}. Because the orientation of the surface is only 7° from {011}, the area of the {011} facet is so much larger than the areas of the minority facets that the differences in area are clearly visible in the AFM image. Figure 4.19 shows an AFM image of the surface structure of a crystallite with the orientation labeled **f** in Figure 4.12a. The majority facet is a complex facet near {111}, and the orientations of the two minority facets are {011}.

Figure 4.20 shows an AFM image of the surface morphology of a crystallite with the orientation labeled **g** in Figure 4.12a. This orientation is partially composed of two facets. Like the surface shown in Figure 4.10 and the other three surfaces that were examined with orientations in this region of the orientation stability figure, this surface has not completely faceted. A careful examination of the figure shows that many of the facets are disjoint and appear to grow out of a continuous, flat background. This indicates that surfaces with orientations near {010} may need more time at 1273 K than

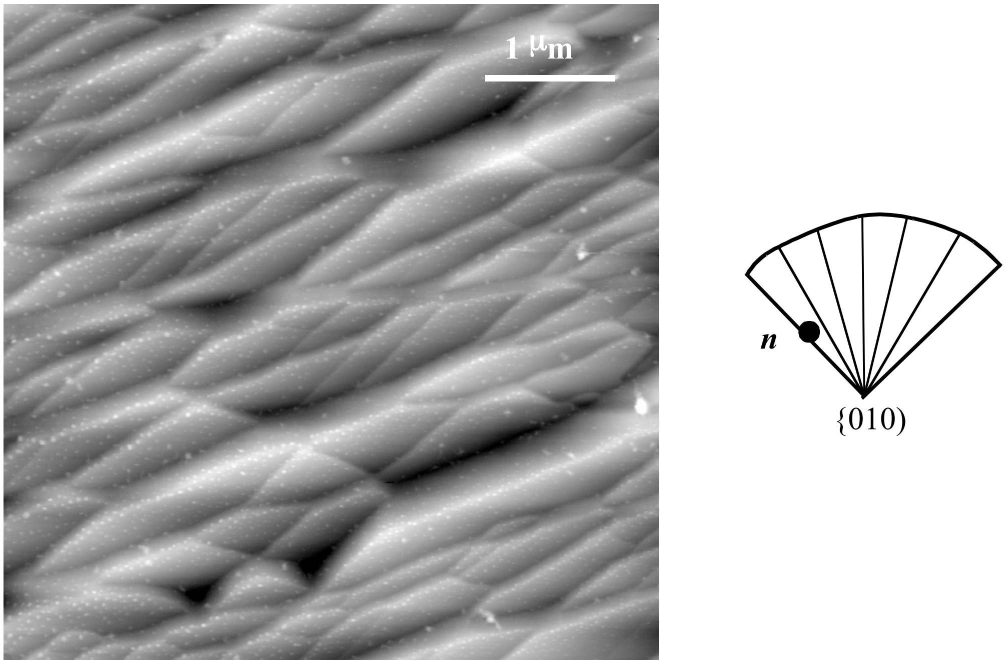

Figure 4.20—An AFM image of the surface with the orientation labeled **g** in Figure 4.12a. The black-to-white range is 335 Å.

surfaces with orientations near {110}, {111}, {011}, or {001} to reach an equilibrated state. The non-equilibrium state of the surface at 1273 K leads to questions about whether orientations near {010} are also in a non-equilibrium state and would facet at 1473 K if annealed for more than five hours. The orientation of the majority and minority facets are both near {010}, and because of the experimental errors discussed previously, it is impossible to determine which facet is the {010} facet and which facet is complex and lies on the line defining the stability of {010}.

The edges of many of the facets are rounded, indicative of the fact that the surface energy is nearly isotropic in this region. There is no one complex facet with lowest energy, so the surface consists of curved facets with orientations that vary depending on the local curvature of the surface.

4.3 Discussion

4.3.1 Surface Energy

In a material with isotropic surface energy, the total surface energy of the system increases as the surface area increases. However, this is not necessarily the case when the surface energy is anisotropic. Consider, for example, the one-dimensional case depicted in Figure 4.21. Here, the condition under which surface C decomposes by faceting to surfaces A and B is defined by the energy criterion:

$$E_0 l_C > E_A l_A + E_B l_B \tag{4.1}$$

where E_0 is the energy per unit length of the original orientation, E_A is the energy per unit length of the lower energy facet A, E_B is the energy per unit length of the lower energy facet B, l_C is the length of the original surface, l_A is the length of the lower energy facet A, and l_B is the length of the lower energy facet B.

The lengths of the two facets are related by the sine law to the angles the facets make with the surface and the length of the surface they are replacing. Using the fact that $\sin(\pi - (\alpha+\beta)) = \sin(\alpha+\beta)$, the relationships between the lengths become

$$l_A = \frac{l_C \sin\alpha}{\sin(\alpha+\beta)} \tag{4.2}$$

$$l_B = \frac{l_C \sin\beta}{\sin(\alpha+\beta)} \tag{4.3}$$

where α is the angle facet B makes with the flat surface and β is the angle facet A makes

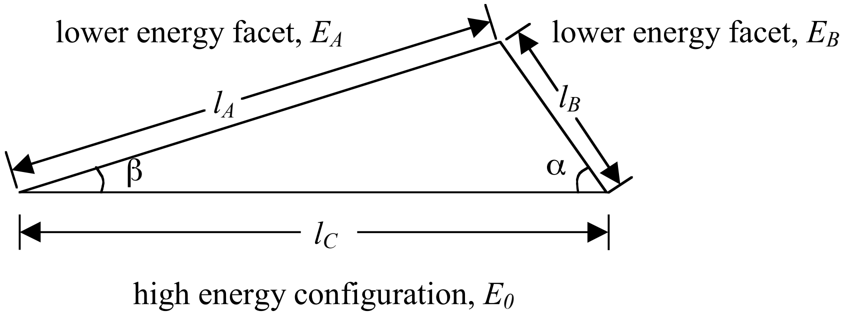

Figure 4.21—A schematic of a faceted surface.

the flat surface. Using Equations 4.2 and 4.3, Equation 4.1 simplifies to

$$E_0 > E_A \frac{\sin\alpha}{\sin(\alpha+\beta)} + E_B \frac{\sin\beta}{\sin(\alpha+\beta)} = E_{hkl} \tag{4.4}$$

For a surface with a random—but fixed—orientation, α and β are also fixed for each possible combination of facets. Therefore, if the energies of the facets on a surface are known, then the minimum energy of the original surface can be calculated using an equation similar to Equation 4.4 for two-dimensional surfaces.

In two dimensions, Equation 4.1 takes on the form

$$E_0\,A > \sum_{i=1}^{n} E_i\,A_i \tag{4.5}$$

where A is the original area of the surface, E_i is the energy of the i^{th} facet present on the surface, A_i is the area of the i^{th} facet present on the surface, and n is the number of distinct facets on the surface. Note that in Equation 4.5, the areas of the facets are fixed in order to maintain the overall orientation of the surface.

If, instead of a randomly-oriented surface, a single crystal that was allowed to reach equilibrium at the temperature of interest were examined, the areas of the facets would no longer be fixed because there would be no constraint on the overall orientation of any given surface. Therefore, the crystal would be able to reach the absolute lowest energy state, or Wulff shape. In this case, the relative areas of the facets on the Wulff form could be used to determine the relative energies of the facets.

However, the overall orientations of the surfaces studied here were constrained, and therefore, the areas of the facets on the surface give no information about the relative energies of the facets present. As discussed in §2.5.1, it is possible to use the angular separation between a stable singular facet and a stable complex facet to determine the relative surface energy of the complex facet, assuming that the intersections between the facets are in local equilibrium [1]. We believe, based on the stability of the angles between the facets, that the intersections between the facets have reached local equilibrium. The angles between the facets on most surfaces remained constant within experimental error after different annealing treatments. The only noticeable effect was the coarsening of the facets as the annealing time increased.

Using $E_{\{011\}} = 1$, the energies of the stable complex facets that can be calculated using the following equation derived from Herring's equation [1]:

$$\frac{\gamma_{\{hkl\}}}{\gamma_{\text{complex}}} = \cos\theta \tag{4.6}$$

where $\gamma_{\{hkl\}}$ is the energy of the singular facet, γ_{complex} is the energy of the complex facet, and θ is the angle between the singular facet and the complex facet. If we assume that the connected, regions that are stable with respect to faceting are isotropic, the energies of the other singular facets can be calculated as well. While this assumption is not strictly true, surface energy variations of more than a few percent would lead to additional faceting.

Table 4.3 lists the surface energies at both 1273 K and 1473 K as well as the number of observations made to calculate each energy using the assumption of isotropy. Somewhat surprising is the fact that the {011} surface is the most stable surface at both 1473 K and 1273 K, followed by the {110} surface. Considering the magnitude of the error in the calculated energy of the {110} surface and the assumption of isotropy for the unfaceted regions, the difference in energy between the {110} and the {011} may be smaller than that shown in Table 4.3. For example, if the energy of the unfaceted region labeled A in both Figures 4.3 and 4.11 decreases smoothly as the orientation moves away from {001}, the surface energy of the {110} surface, which was calculated assuming that the energy of the unfaceted region is isotropic, could be lower than the surface energy of the {011}.

Table 4.3: Surface Energies

	1473 K		**1273 K**	
	relative energy	**number of measurements**	**relative energy**	**number of measurements**
{011}	1	N/A	1	N/A
region A	1.10±0.03	19	1.09±0.02	14
stable region around {001}	1.10±0.03	12	1.13±0.02	21
I	1.07±0.02	8	not stable	N/A
stable region around {110}	1.05±0.05	4	1.05±0.05	7
stable region around {010}	in region A	N/A	1.09±0.03	3

With the exception of the surface energy of the {001}, the surface energies of the various surfaces do not vary with temperature between 1273 K and 1473 K. The {001} becomes rapidly less stable as temperature decreases, suggesting that the {001} will not be stable with respect to faceting at temperatures much lower than 1273 K. The energy of the {010} at 1273 K is only slightly less than the energy of the complex facets which border its stability region; this difference in energy is smaller than the accuracy of the data. The results indicate a maximum anisotropy of 13% at 1273 K. The magnitude of this anisotropy is similar to that observed for Al_2O_3 at 1873 K [6].

4.3.2 Surface Morphology

As mentioned in Chapter 2, Ramamoorthy et al. [7] calculated a probable equilibrium shape of rutile at 0 K based on the calculated energies of the {001}, {011}, {010} and {110} rutile surfaces. This shape is shown in Figure 2.9, with modifications based on experimental evidence showing that the {111} surface is stable. However, it is apparent by examining the orientation stability figures shown in Figures 4.4a and 4.12a that this shape is not valid at 1273 K or 1473 K. The first difference of note is that the shape calculated by Ramamoorthy et al. [7] assumes a completely faceted form, which is clearly not the case at 1273 K or 1473 K. There are large regions of orientation space where the differences in the surface energies of neighboring orientations are not great enough for the formation of facets to be energetically favorable, leading to large regions of orientation space where the stable surface morphology is flat.

The surface energies calculated by Ramamoorthy et al. [7] also predict that the {001} surface is not stable. However, at both 1273 K and 1473 K, the {001} surface is stable with respect to faceting, as is a small region of orientation space surrounding the {001}. At 1473 K, orientations within approximately 8° of the {001} are stable with respect to faceting, and facets with orientations approximately 8° from the {001} appear on surfaces with orientations tilted more than 25° away from the {001} toward the {011}. Facets with orientations approximately 3° from the {001} are stable over a similar region of orientation space at 1273 K. Ramamoorthy et al. [7] assumed that the {001} is terminated ideally, leaving the surface titanium ions attached to four oxygen ions. One possible explanation for the apparent discrepancy is that the {001} surface reconstructs to form a more stable surface structure that Ramamoorthy et al. [7] did not take into account when making their model. Another possible explanation is that the {001} surface is unstable with respect to faceting at 1273 K or 1473 K, but the surfaces with orientations in the regions that appear stable are faceted on a nanometer scale. Such nanoscale faceting has been seen on {001} single crystals using AFM [8], but the polycrystals were never examined with the resolution that would be required to observe such small features.

As mentioned previously, work by Firment [3] and Poirier et al. [4] determined that the {114} was stable at temperatures greater than 1300 K, while Wang et al. [5] determined that the {124} was stable after annealing at 1698 K in oxygen. The results of this study indicate that neither of these two orientations are stable at either 1298 K or 1498 K. As discussed in §4.1, the experimental evidence indicates that the orientation labeled I in Figure 4.4a is closest to {112}. We see no flat surfaces near this orientation, although there are at least 9 crystallites with surfaces partially composed of this facet. Because complex facets border regions of orientation space that are stable with respect to faceting, we conclude, based on the lack of stable surfaces near this orientation, that orientation I is {112} and not a complex facet near {112}.

The discrepancy between the current results and the results from Firment [3], Poirier et al. [4], and Wang et al. [5] could be due to differences in experimental techniques. In the work of Firment [3] and Poirier et al. [4], the faceting measurements were completed after prolonged annealing in vacuum, and although Wang et al. [5] annealed their experimental specimens in oxygen environments, the data were taken in vacuum and the annealing temperature was greater than that used in this thesis. As discussed in §2.2.2, annealing in vacuum is known to affect the surface structure of the {110}, and the vacuum induced reconstruction of the {010} has sometimes been characterized as microfaceting [9]. Therefore, it is not unlikely that the prolonged annealing and data collection in vacuum affected the stability of the various orientations.

Assuming that the facet intersections examined in this study were in local equilibrium, the surface energies calculated provide some information about the equilibrium shape of rutile crystallites at 1273 K and 1473 K. Although the theoretical work by Ramamoorthy et al. [7] was a valuable guide, the surface energies they calculated for rutile are more highly anisotropic than those calculated in this study. For example, Ramamoorthy et al. [7] calculated that the relative surface energy of the highest energy surface, {001}, is almost twice that of the lowest energy surface, {110}. The smaller surface energy anisotropy determined in this study leads to a more isotropic Wulff shape at both 1273 K and 1473 K than was calculated by Ramamoorthy et al. [7] and shown in Figures 2.8 and 2.9. The addition of regions that are stable with respect to faceting also creates rounded areas in the Wulff shape, and the {001} is added as a small, slightly curved surface that is larger at 1473 K that at 1273 K.

Figure 4.22 shows projections along (001), (100), and $(1\bar{1}0)$ of the Wulff shape for rutile at 1473 K. As seen in the projections along (001) and (100), the {010} does not exist as a facet on the Wulff shape. The {110} facets are significantly smaller than those calculated by Ramamoorthy et al. [7] and are connected by curved surfaces to both the {011} and to other {110} facets. The {011} facets are connected to each other along sharp edges along the ⟨111⟩, similar to that shown in Figure 2.8. As shown in the projection along (100), the {112} appears approximately 18° to the {001} along the ⟨111⟩ and connects to a curved surface approximately 35° to the {001}.

Figure 4.23 shows projections along (001), (100), and $(1\bar{1}0)$ of the Wulff shape for rutile at 1273 K. The Wulff shape at this temperature is slightly more elongated that the one at 1473 K. The {010} now exists as a small, distinct, equiaxed facet that is connected to {011} and {110} facets with curved surfaces. The curved surface around {001} is smaller, and the {112} facet no longer exists.

One last feature of note when comparing the two orientation stability figure is that a larger percentage of orientation space is stable with respect to faceting at 1473 K than at 1273 K. Because of the increased temperature, entropy plays a greater role in determining the minimum energy surface morphology at 1473 K than at 1273 K. These observations are consistent with the expectation that surface roughening increases as the temperature increases, as discussed in §2.4.

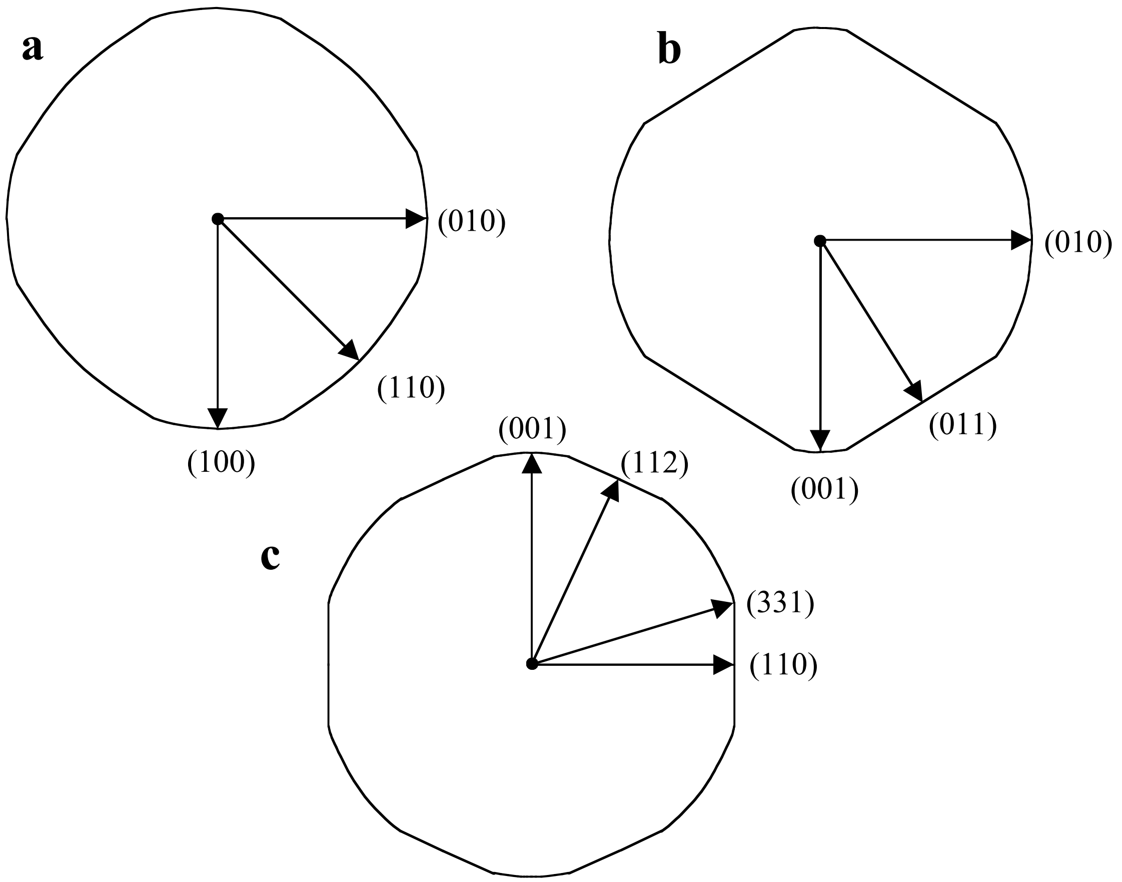

Figure 4.22—Projections of the Wulff shape of rutile at 1473 K along the a) (001), b) (100), and c) $(1\bar{1}0)$.

4.4 Summary

AFM and EBSD were used to determine the stable orientations of rutile at 1273 K and 1473 K. Orientation stability figures, shown in Figures 4.4 and 4.12, were determined for each temperature, and the relative surface energy of each facet was calculated by applying the Herring equation to the facet intersections [10]. The {011} is the most stable orientation at both temperatures followed by the {110}. The {112} was found to be stable at 1473 K, in contrast to the conclusions of other groups, which found that the {114} [3, 4] or the {124} [5] was stable. In addition, the {001} was found to be stable at 1273 K and 1473 K, contrary to previous research [3–5].

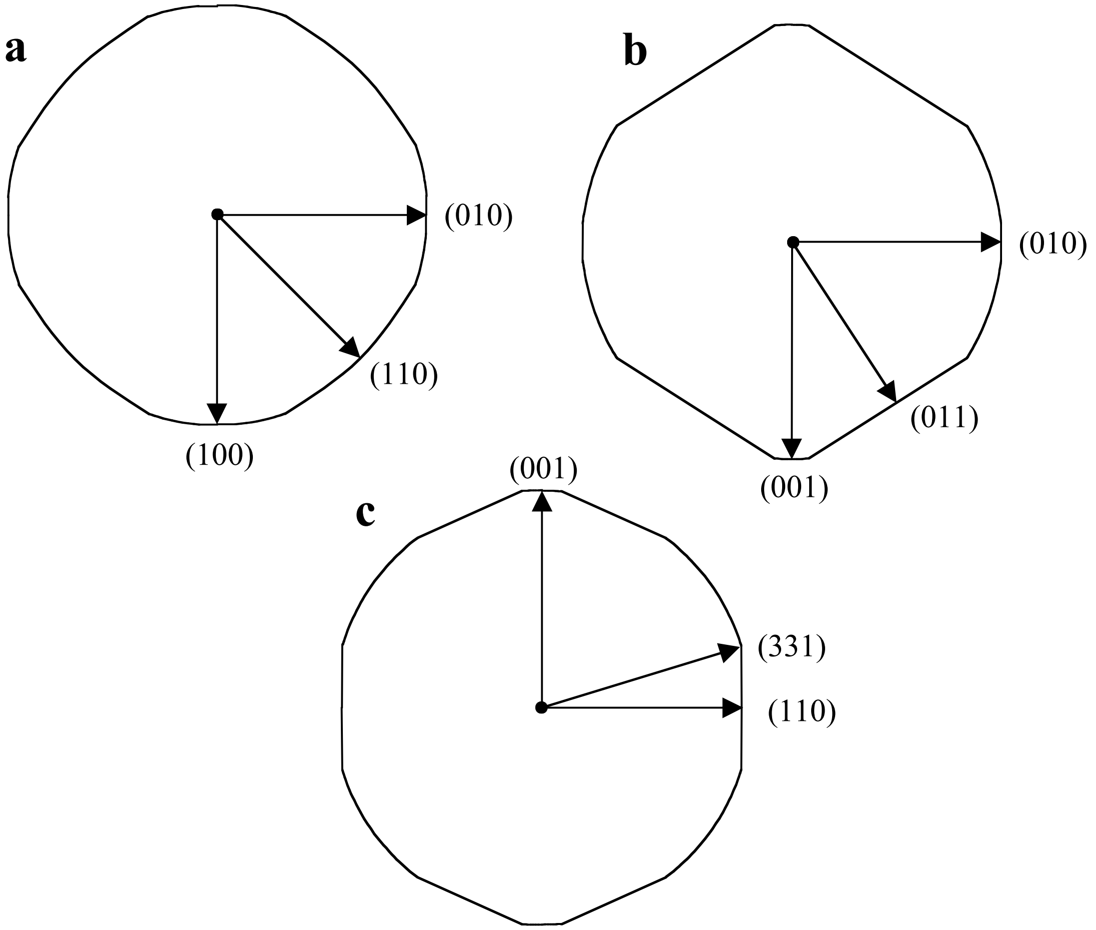

Figure 4.23—Projections of the Wulff shape of rutile at 1273 K along the a) (001), b) (100), and c) $(\bar{1}10)$.

4.5 References

[1] A. Moore *in* "Metal Surfaces: Structure, Energetics and Kinetics", (N. Gjostein and W. Robertson, Eds.), p155, American Society for Metals (1963).
[2] J. Cahn and C. Handwerker, *Mat. Sci. Eng. A* **162** (1993) 83.
[3] L. Firment, *Surf. Sci.* **149** (1982) 205.
[4] G. Poirier, B. Hance, and J. White, *J. Vac. Sci. Technol.* **10** (1992) 6.
[5] L. Wang, J. Liu, and J. Cowley, *Surf. Sci.* **302** (1994) 141.
[6] J.-H. Choi, D.-Y. Kim, B. Hockey, S Wiederhorn, C. Handwerker, J. Blendell, W. Carter, and A. Roosen, *J. Am. Ceram. Soc.* **80** (1997) 62.
[7] M. Ramamoorthy, D. Vanderbilt, and R. King-Smith, *Phys. Rev. B* **49** (1994) 16721.

[8] J. Giocondi, J. Lowekamp, G. Rohrer, and P. Morris Hotsenpiller, *in* “Integrated Thin Films and Applications”, (R. Pandey, P. Morris-Hotsenpiller, A. Roshko, U. Varshney, and D. Witter, Eds.), p233, *Ceram. Trans.* **86**, Westerville, OH (1998).

[9] P. Murray, F. Leibsle, H. Fischer, C. Flipse, C. Muryn, and G. Thornton, *Phys. Rev. B* **46** (1992) 12877.

[10] C. Herring *in* “Structure and Properties of Solid Surfaces”, (Gomer and Smith, Eds.), p5, Chicago University Press, Chicago (1953).

Chapter 5

Photochemical Activity of Polycrystals

In the previous chapter, orientation stability figures were developed for rutile for two annealing conditions: 8 hours at 1473 K and 24 hours at 1273 K. The orientation stability figures show the indices of the stable facets present on the surface of a crystallite of a given orientation. These stability figures will be used in this chapter to help determine the effects of surface structure and orientation on the photochemical activity of rutile polycrystals annealed under the same conditions. The polycrystals used in this series of experiments, with an average grain size of 50 μm, were fabricated as described in §3.1.2. The test reactions used to quantify the photochemical reactivity, as described in §3.2, use silver metal reduced from an aqueous solution of $AgNO_3$ under UV illumination. The amount of silver reduced by each surface is determined using AFM and is assumed to be a quantitative indicator of the surface's photocatalytic activity.

5.1 Photocatalytic Anisotropy

The amount of reduced silver on 188 randomly-oriented crystallites was determined using AFM. The crystallites are divided into two groups. Group A, composed of 92 crystallites annealed at 1473 K for 8 hours, was exposed to UV radiation in an aqueous $AgNO_3$ solution until the light reflected from the polycrystal surface was reduced by 8%. Group B, composed of 96 crystallites annealed at 1273 K for 24 hours, was exposed to UV radiation in an aqueous $AgNO_3$ solution until the light reflected from the polycrystal surface was reduced by 6%.

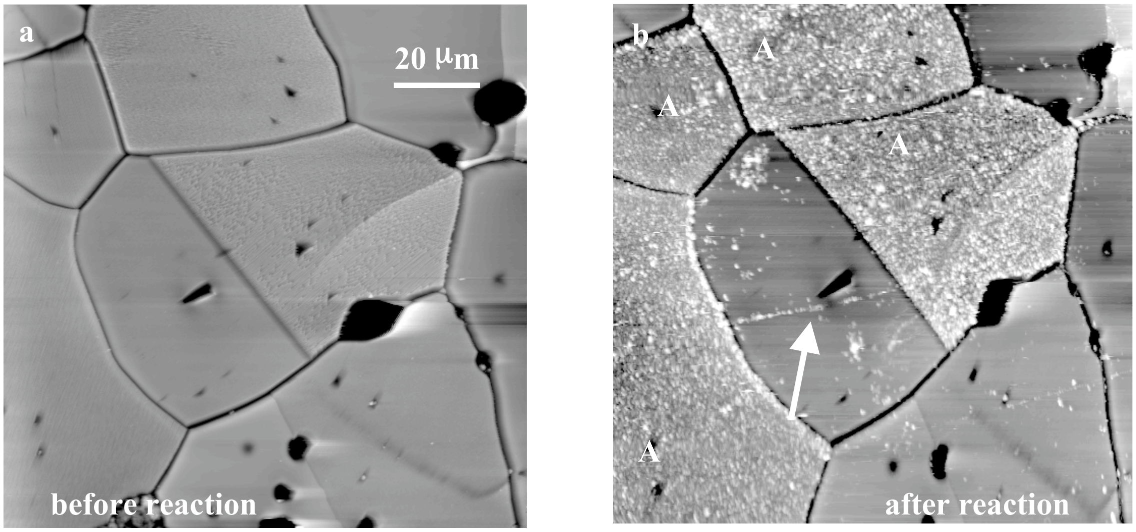

Figure 5.1—Anisotropic silver reduction on rutile polycrystal. The arrow points to a highly active scratch in an inactive crystallite.

In both sets of data, there is clear evidence of anisotropy in the photocatalytic activity of the crystallites, as shown in Figure 5.1. Figure 5.1a shows an 80×80 μm^2 AFM image of several group A crystallites before the silver reduction reaction, and Figure 5.1b shows the same region after the silver reduction reaction. The silver deposits appear as white spots on the AFM images because they are higher than the surrounding rutile surface. It is clear from a comparison of these images that several of the grains, those marked A in Figure 5.1b, have many more silver deposits than other grains in this region.

To verify that the deposits on the surface were silver and not surface contamination, EDX analysis was conducted, which showed that the crystallite surfaces with the most deposits as seen in the AFM had the greatest density of silver (see §3.3.5).

5.1.1 Distribution of Silver

To minimize the effect of noise caused by surface contamination, three categories of photochemical activity were defined based on the density of deposits on the surface. Crystallite surfaces with greater than 4 deposits/μm^2 were categorized as high-activity surfaces, while surfaces with 2 deposits/μm^2 or fewer were categorized as low-activity surface. Surfaces with greater than 2 Ag deposits/μm^2 but fewer than 4 Ag deposits/μm^2 were categorized as intermediate-activity surfaces.

The lower limit of 4 deposits/μm^2 for highly active surfaces was chosen because in general, deposits begin to impinge on surfaces containing more than 4 deposits/μm^2, making it difficult to determine the density of deposits. For example, Figure 5.2a shows an AFM image of a highly active crystallite before the silver reduction reaction. This surface is composed of three facets. The orientation of the majority facet on this surface is (011), while the orientations of the two minority facets are (101) and a complex facet near (001). Figure 5.2b shows an AFM image of the same crystallite after the silver reduction reaction. Although the surface is not completely covered—i.e. the facet structure is still apparent—it is impossible to clearly distinguish all of the silver deposits on the surface. However, although the exact number cannot be determined, there are clearly more than 100 silver deposits in the 25μm^2 area, leading to the decision that the surface is highly active.

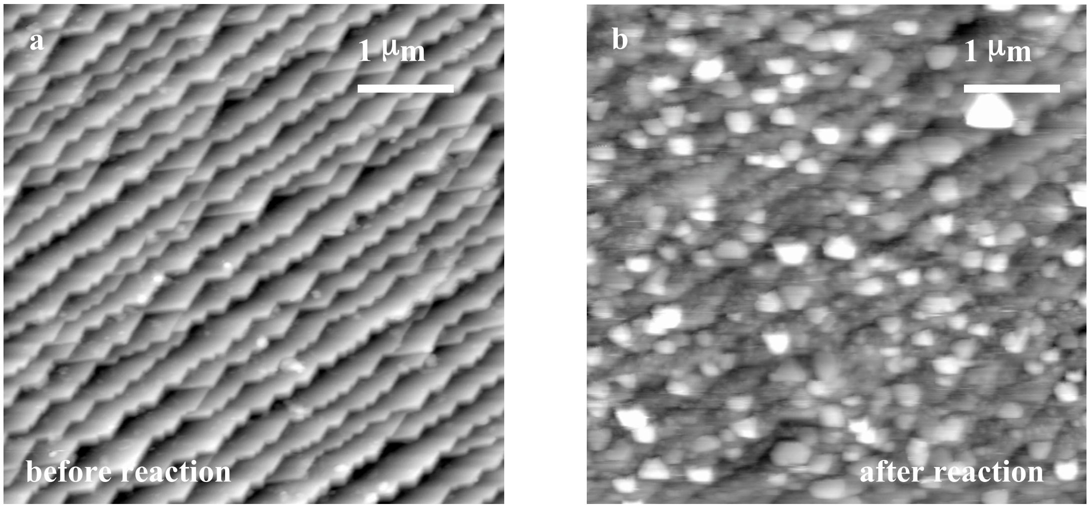

Figure 5.2—An AFM image of a highly active crystallite.
a) The facet structure of the crystallite before the silver is reduced. The black-to-white range is 695 Å.
b) The surface of the crystallite after the silver is reduced. The black-to-white range is 0.12 μm.

Silver deposits on surfaces having intermediate activity are easily enumerated and tend to lie along regular surface features, such as step edges. For example, Figure 5.3a shows an AFM image of an intermediate-activity crystallite before the silver reduction reaction. The surface is composed of two facets. The majority facet on this surface is a complex facet near {001}, and the minority facet is {011}. The white spots in Figure 5.3a, the highest of which is approximately 200 Å tall, are believed to be surface contamination. Figure 5.3b shows an AFM image of the same crystallite after the silver reduction reaction. The white spots in this image, the highest of which are approximately 0.14 μm tall, appear distinctly different from those present in Figure 5.3a, and it was concluded that they are mainly silver deposits. These silver deposits appear preferentially near the step edges between the complex facets near {001} and the {011} facets, which may indicate that the active sites for silver reduction lie along the intersections or on the minority facet. Because of the autocatalytic nature of silver reduction on rutile once a nucleus is formed, it is impossible to tell exactly where the active nucleation site is from these the AFM images.

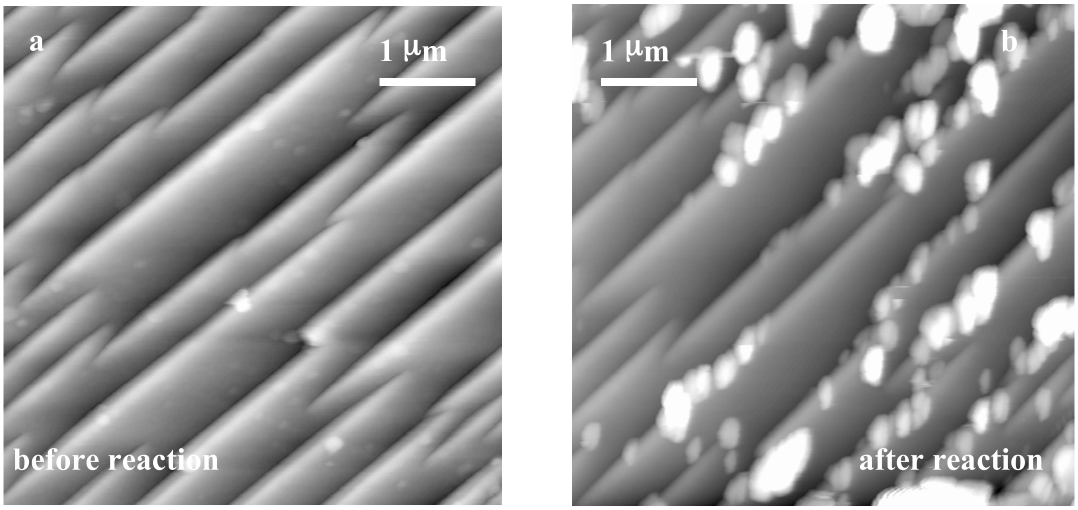

Figure 5.3—An AFM image of a crystallite with intermediate activity.
a) The facet structure of the crystallite before the silver is reduced. The black-to-white range is 600 Å.
b) The surface of the crystallite after the silver is reduced. The black-to-white range is 0.10 μm.

Deposits on surfaces with fewer than 2 deposits/μm^2 seem to be randomly distributed instead of due to a regular surface feature. For example, Figure 5.4a shows an AFM image of a low-activity, faceted surface before the silver reduction reaction, and Figure 5.4b shows an AFM of the same crystallite after the silver reduction reaction. As in Figure 5.3a, the white spots in Figure 5.4a, the highest of which are 0.13 μm tall, are believed to be surface contamination, while the white spots in Figure 5.4b, which are approximately 700 Å tall, could be either surface contamination or silver deposits. However, even if all of the white spots in Figure 5.4b are silver deposits, the crystallite's surface can be categorized as inactive since there are fewer than 50 white spots on the 25 μm^2 surface.

5.1.2 Effects of Non-planar Features

A variety of non-regular features that can affect rutile's photochemical activity appear on the surface of the polycrystals. For example, scratches remaining after the thermal anneal expose sites to the aqueous $AgNO_3$ solution that are different from those exposed on the remainder of the surface. In some cases, such as the scratch distinguished

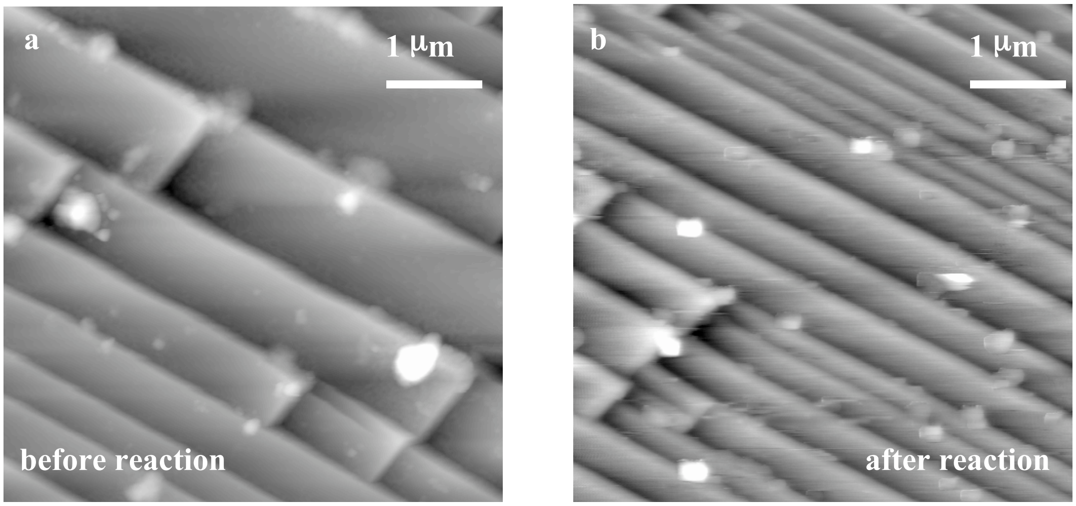

Figure 5.4—An AFM image of an inactive crystallite.
a) The facet structure of the crystallite before the silver is reduced. The black-to-white range is 0.15 μm.
b) The surface of the crystallite after the silver is reduced. The black-to-white range is 900 Å.

by the arrow in Figure 5.1, the activities of the sites exposed in the scratch are much greater than those on the remainder of the crystallite's surface.

Voids and grain boundary grooves also expose different sites to the aqueous $AgNO_3$ solution, which can lead to large differences between the photochemical activity of the grain boundaries and voids and the photochemical activity of the surrounding grains. Figure 5.5 shows one example of a highly active grain boundary groove surface between two inactive crystallites. Similarly, Figure 5.6 shows an example of a pore with a higher concentration of silver deposits along one edge of the pore than on the remaining surface of the crystallite. It is clear from the image that the sides of the pore expose sites which are more favorable to the photoreduction of silver than the flat surface of the remainder of the crystallite and that sites on the left side of the pore are more favorable to the photoreduction of silver than sites on the right side of the pore.

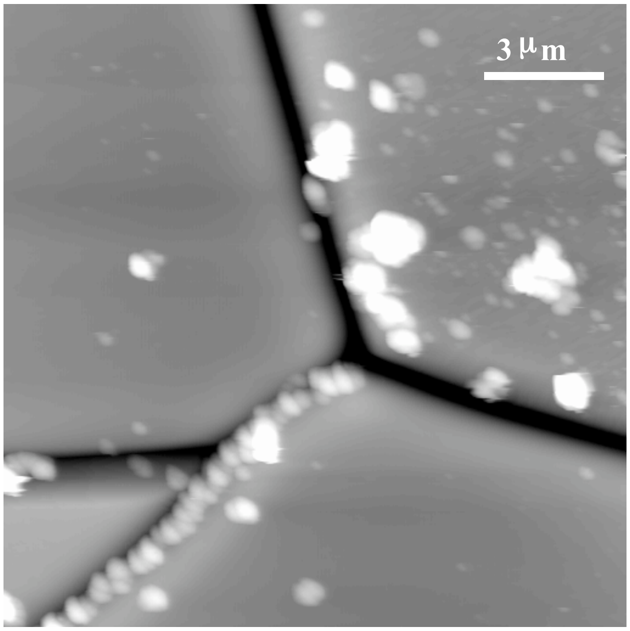

Figure 5.5—An active grain boundary separating two inactive grains.

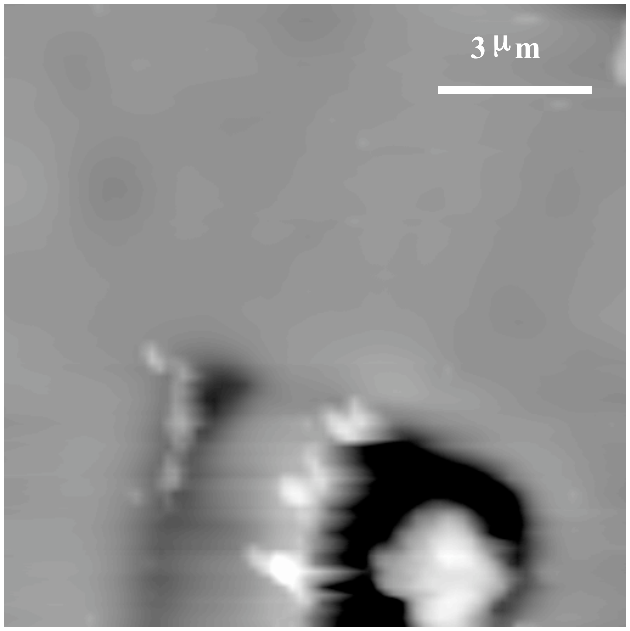

Figure 5.6—An active pore in an inactive grain.

5.2 The Effect of Surface Orientation

Figure 5.7 is an inverse pole figure showing a summary of the photocatalytic activity data for 188 rutile crystallites. For each crystallite whose activity was measured, a symbol is placed in the inverse pole figure at the crystallite's orientation indicating the extent to which the surface is covered with silver particles. Black-filled squares represent the highly-active orientations, gray-filled squares represent the intermediate-activity orientations, and hollow squares represent the low-activity orientations. The inverse pole figure clearly shows that the high-activity orientations are not distributed randomly but are concentrated in the region around {011}.

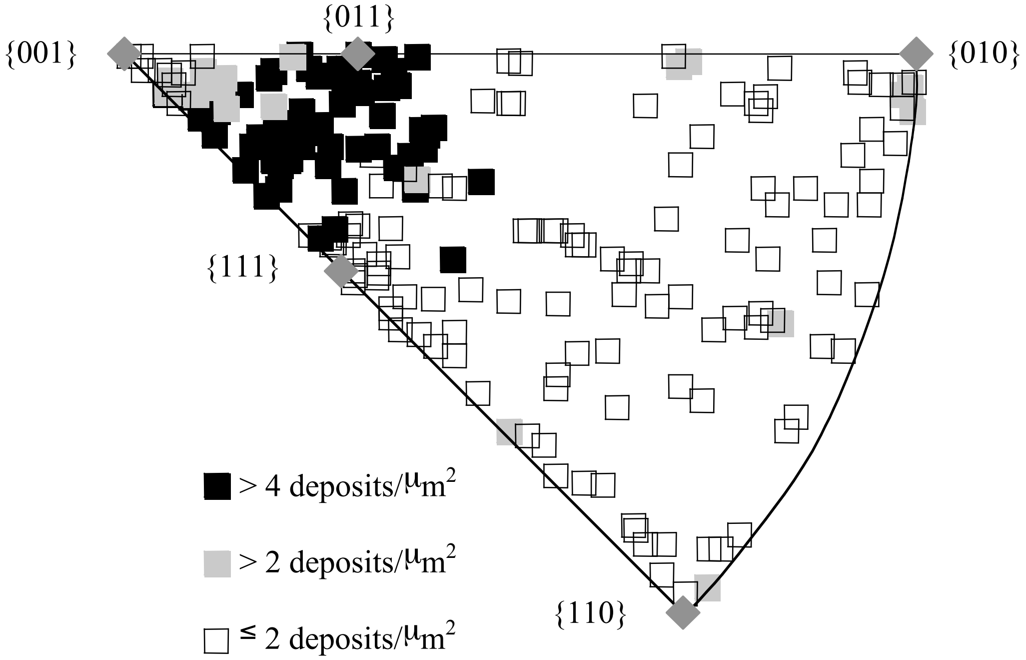

Figure 5.7—Photocatalytic activity versus orientation.

5.3 The Effect of Surface Faceting

5.3.1 Group A Crystallites

Figure 5.8 summarizes the activity data for the 92 group A crystallites with respect to the stability of the various facets. As in Figure 5.7, each symbol in Figure 5.8 represents the activity of a rutile crystallite. These symbols have been placed on one-half of the orientation stability figure for 1473 K, originally seen in Figure 4.4. As described in §2.4, the gray areas represent the orientations that are stable with respect to faceting. Orientations within the white regions that are filled with lines are unstable with respect to faceting into the two orientations at the ends of the tie lines on which they lie. Orientations within empty white triangles are unstable with respect to faceting into the orientations at the corners of the triangle. Using this information, an examination of Figure 5.8 indicates that nearly all of the highly active grains, represented by the solid black squares, lie in the region where {011} facets are stable.

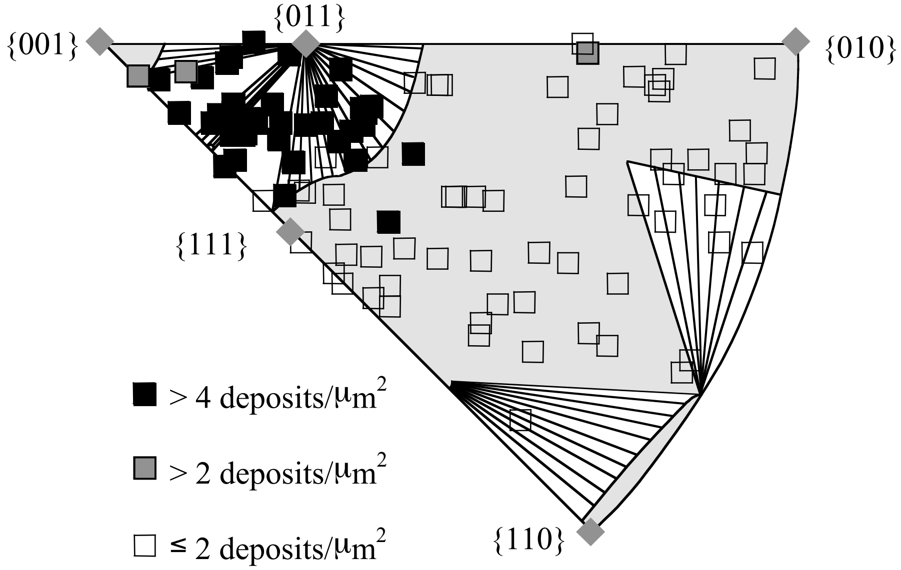

Figure 5.8—Photochemical activity versus orientation for group A crystallites. The data are plotted on the orientation stability figure from Figure 4.4b.

5.3.2 Group B Crystallites

Figure 5.9 summarizes the activity data for the 96 group B crystallites with respect to the stability of the various facets. The total amount of silver reduced by the polycrystal in this experiment is less than the total amount of silver reduced by the polycrystal from which the 92 group A crystallites were chosen. As in Figures 5.7 and 5.8, each symbol in Figure 5.9 represents the activity of a rutile crystallite. These symbols have been placed on one-half of the orientation stability figure for 1273K, originally seen in Figure 4.12. An examination of Figure 5.9 indicates that the highly active grains, represented by the solid black squares, lie in the region where {011} facets are stable, identical to the case where the silver reduction reaction was carried out to a 8% drop in reflectivity. More specifically, the orientations of the crystallites with the highest activity are clustered within a few degrees of the {011} and along the two phase region between {011} and {101}, indicating that the presence of {011} facets plays a key role in determining the total number of silver deposits reduced by rutile crystallites.

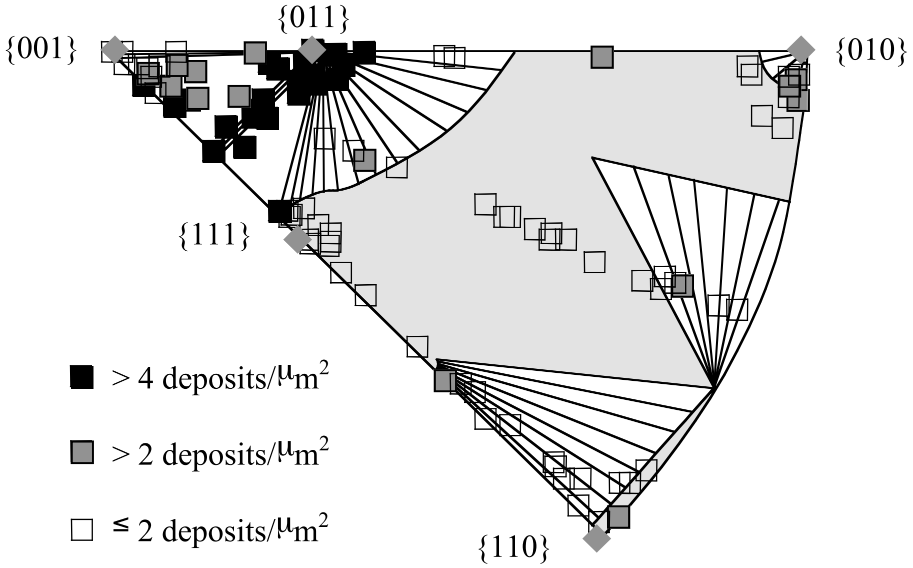

Figure 5.9—Photochemical activity versus orientation for group B crystallites. The data are plotted on the orientation stability figure from Figure 4.12b.

5.3.3 Importance of {011} facets

The activity of group A and group B crystallites was correlated to the presence of {011} facets, and the relationship is shown in Figures 5.10 and 5.11, respectively. Both Figures 5.10 and 5.11 are bar graphs displaying two categories: the first shows the number of crystallites of each activity level that have {011} facets, and the second shows the number of crystallites of each activity level that do not have {011} facets.

In Figure 5.10, the distribution appears almost binary, with all but two crystallites with {011} facets being highly active and all but one crystallite without {011} facets showing little activity. Therefore, the data clearly indicate that the presence of {011} facets is critical to high photocatalytic activity. However, the fact there are so few crystallites with intermediate activities makes it difficult to examine the transition region between the high- and low-activity states.

The results shown in Figure 5.11 agree well with the results shown in Figure 5.10. The graph clearly shows that all highly active crystallites have {011} facets and that most

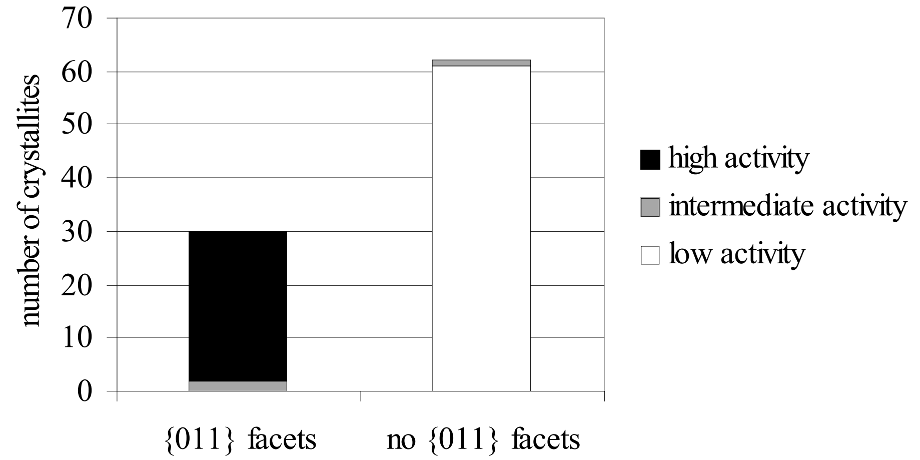

Figure 5.10—The relationship between photocatalytic activity and {011} facets for group A crystallites.

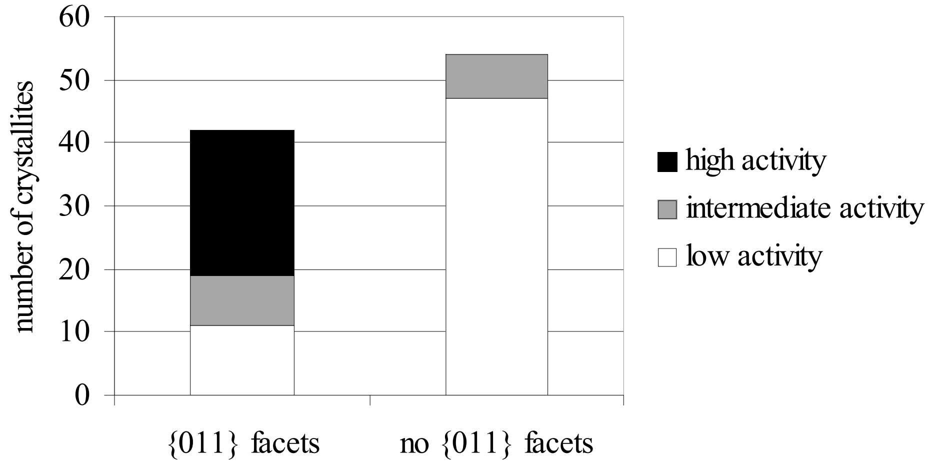

Figure 5.11—The relationship between photocatalytic activity and {011} facets for group B crystallites.

of the crystallites with low activity do not have {011} facets. Unlike the previously discussed results for group A crystallites, there are far more crystallites with intermediate activity in the group B data set, so it is possible to examine the results more carefully for the reasons behind the importance of the {011}.

5.4 Effect of Surface Properties on Photoactivity

If the anisotropic photochemical activity were due primarily to any property which depended on the overall orientation of the surface and not on specific surface structures, surface features such as scratches would have little effect on the reactivity of a crystallite's surface. However, this is not consistent with the observations. The scratch indicated by the arrow in Figure 5.1 crosses a relatively inactive grain and is completely covered with silver, indicating that something about the scratch has increased the local reaction rates. Because the bulk orientation of the crystallite is not changed by the scratch, the increased reaction rates must be caused by a surface structure or feature that is local to the area in or around the scratch.

The large change in photochemical activity that can occur in the region inside a scratch indicates that the photochemical activity of rutile depends strongly on some specific surface feature or features. Because the highly active orientations appear in the region of the orientation stability figure where {011} facets are stable, one hypothesis is that there is a special site on the {011} facet that is necessary for the photo-oxidation of water and/or the photoreduction of silver ions. If this hypothesis is true, the photocatalytic activity of the rutile crystallites should increase as the relative area of the {011} facets increases.

Another possibility is that there is a special site on the intersections between the {011} facets and neighboring facets that is necessary for one or both of the photocatalytic reactions to occur. If this hypothesis is true, the photocatalytic activity of the crystallites should increase as the linear step density, or number of facet intersections per micron, increases. The following sections will examine these two hypotheses.

5.4.1 Effect of the Area of {011} Facets

As mentioned previously, it is possible that the active site for one or both of the photocatalytic reactions is on the {011} surface. If this is true, the presence of the {011} facet would be the only surface feature necessary for high photocatalytic activity, and there should be a strong correlation between the fractional area of the {011} facet and the activity of a crystallite. Figure 5.12 shows the relationship between photocatalytic activity and the fractional area of {011} facets on those group B crystallites with {011} facets. It is clear from a cursory examination of Figure 5.12 that the crystallites with the lowest fractional area of {011} facets have a lower overall activity than the crystallites with the highest fractional area of {011} facets.

A more thorough examination of Figure 5.12 shows a critical point for this particular exposure somewhere between 40% and 60% {011} facets so that crystallites with a fractional area of {011} facets greater than this critical point are likely to be highly active while crystallites with a fractional area of {011} facets smaller than this critical point are relatively inactive. This agrees well with the results from the group A crystallites, where it can be inferred that the exposure time was great enough that this critical point for high activity decreased to nearly 0%, so that any {011} facets produced a highly active surface.

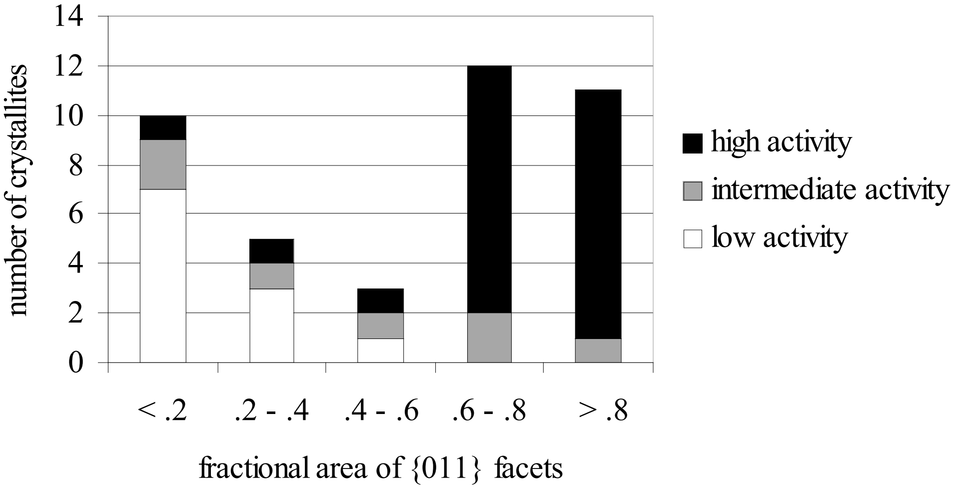

Figure 5.12—The photochemical activity of the group B crystallites with {011} facets versus the fractional area of {011} facets.

5.4.2 Effect of Step Density

The second hypothesis is that the active sites for either photoreduction, photo-oxidation, or both are on the intersections between the {011} facets and neighboring facets. If this were the case and all facet intersections were equivalent, the photocatalytic activity of the crystallites with {011} facets should depend strongly on the surface step density. Figure 5.13 shows the relationship between the photochemical activity of the group B crystallites with {011} facets and the surface step density. A cursory examination of Figure 5.13 indicates that the crystallites with the smallest step densities are generally less active than the crystallites with greater step densities. A more thorough examination of Figure 5.13 seems to indicate a critical point for this particular exposure somewhere between 3 and 5 intersections/μm so that crystallites with a step density greater than this critical point are relatively active while crystallites with a step density smaller than this critical point are relatively inactive. This result also agrees well with the results from the group A crystallites, where it can be inferred that the exposure time was great enough that this critical step density for high activity was decreased to nearly zero, so that a few facet intersections across a crystallite surface produced a highly active surface.

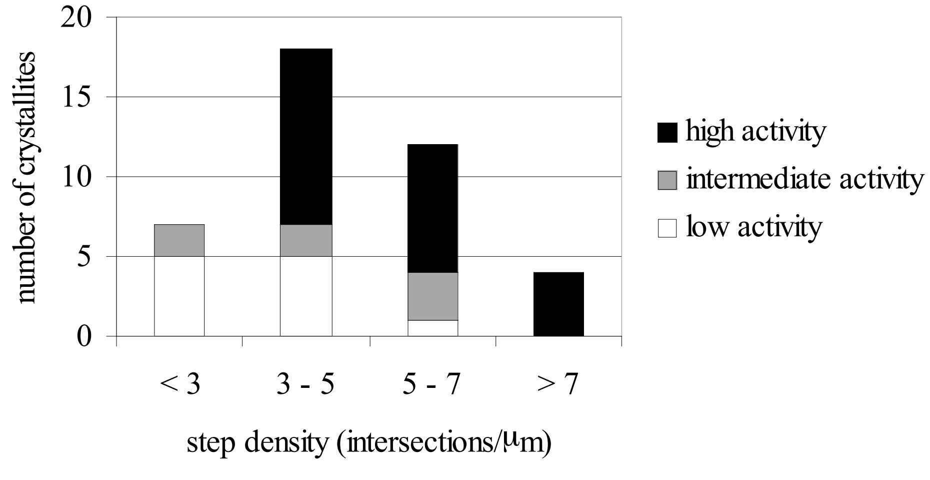

Figure 5.13—The photochemical activity of the group B crystallites with {011} facets versus the step density.

5.4.3 Comparison

Unfortunately, the previously discussed data cannot be used to distinguish between the two hypotheses. A close examination of the crystallites in group B showed that all of the crystallites with the lowest step densities also had the lowest fractional area of {011} facets, so the effects of step density and fractional {011} facet area cannot be separated. Counter to what might be expected, most of the crystallites that are a few degrees from {011} and have large fractional areas of {011} facets have intermediate step densities. The step densities of these crystallites range from 4.5 and 6 intersections/μm with two outliers: one with a step density of 3.3 intersections/μm, and another with a step density greater than 8 intersections/μm. Because the step density of the crystallites with the highest fractional area of {011} facets is also high, it is difficult to separate the possible effects of the changing step density from the possible effects of the changing fractional areas of the {011} facets. The only certain conclusion is that the presence of {011}facets, due to active sites either on the {011} plane itself or on the steps it forms with neighboring facets, is necessary to create a highly active rutile surface.

5.5 Discussion

The importance of the {011} surface to high photochemical activity is evident from the experimental observations. One possible explanation is that the silver ions are reduced on the {011} facets at a greater rate than on other facets, leading to the large number of silver deposits. In this case, the high photoreduction rate of the {011} could be due to factors such as adsorption anisotropy or surface energy anisotropy. These possibilities will be examined in §5.5.2.2.

It is possible, however, that the large amount of silver on surfaces with {011} facets is not the result of enhanced photochemical activity. We do not directly measure the active sites on the crystallite surfaces; we only measure the final location of the metallic silver. The AFM images might look the same if all crystallite surfaces had the same photochemical activity and neutral silver atoms were capable of diffusing long distances to deposit on {011} surfaces preferentially because of a reduced nucleation barrier. For example, if there were strong epitaxy between TiO_2 {011} and silver, the interfacial energy would be reduced, and the nucleation barrier would be lower. Section 5.5.2.1 will examine these possibilities and show that they are not consistent with experimental observations. Section 5.5.1 will examine the possibility that the high photocatalytic activity is due to anisotropic bulk properties, such as anisotropic electrical conductivity or light absorption.

5.5.1 Effect of Bulk Properties on Photochemical activity

5.5.1.1 Electrical conductivity

The photocatalytic anisotropy of the rutile crystallites could be due to several factors that primarily depend either on a crystallite's orientation or on the presence of specific surface features. While the observations strongly suggest that surface properties rather than bulk properties are responsible for rutile's anisotropic photochemical activity, it is important to consider the possibility that the bulk characteristics of rutile influence the mechanism. One such factor is rutile's anisotropic electrical conductivity. Higher electrical conductivity along certain directions means a greater mean-free path, or time between collisions, for electrons traveling in those directions. Since a collision can lead to recombination, a larger mean-free path means that on average, electrons travel farther before recombining. Therefore, if the electron or hole transport to the surface is the rate-limiting step in the photocatalytic reactions, higher conductivity normal to the surface should favor higher photochemical activity by permitting more electrons to reach the surface instead of recombining. The electrical conductivity is highest in the $\langle 001 \rangle$ direction [1], so if differences in the electron or hole transport to the surface were the cause behind the large anisotropy in the photocatalytic activity, surfaces whose normals include a large component in the $\langle 001 \rangle$ direction should have a higher photochemical activity than surfaces whose normals include a small or no component in the $\langle 001 \rangle$ direction. The results, however, do not support this conclusion. The photocatalytic activity is lower on surfaces with orientations within 5° of {001}—i.e., within 5° of $\langle 001 \rangle$—than on surfaces with orientations within 5° of {011}—i.e., more than 25° from

⟨001⟩. Therefore, we conclude that the anisotropic electrical conductivity is not the cause of the anisotropic photocatalytic activity.

5.5.1.2 Anisotropic light absorption

Anisotropic light absorption can also affect reaction rates on different surfaces. When light is adsorbed more efficiently along certain directions, more electron-hole pairs are created along the directions of greatest absorption efficiency. The ratios, {011}/{010} and {001}/{010}, of the absorption coefficients at 405 nm of rutile corrected for reflective losses are 1.0 and 1.3, respectively [2]. If the anisotropic light absorption were the largest factor determining the differences in photochemical activity—i.e., the quantum efficiencies for each orientation are approximately the same—surfaces near {011} and {010} would have similar photochemical activities, while surfaces near {001} would have higher photochemical activities. The results discussed previously do not support this conclusion. As shown in Figure 5.7, surfaces within approximately 5° of {010} and {001} are relatively inactive, while surfaces within 5° of {011} are highly active, which does not correspond to what is expected if light absorption is the rate limiting step of the surface oxidation and reduction reactions. Therefore, we conclude that differences in light absorption are not the main reason behind the photochemical anisotropy.

5.5.2 Surface Effects

5.5.2.1 Nucleation

Epitaxy between Silver and Rutile {011}

As mentioned earlier, one possibility for the large number of silver deposits on crystallites with {011} facets is that an epitaxial relationship exists between the close-packed plane of silver and the rutile {011} surface. Figure 5.14 shows the unreconstructed rutile {011} surface. Next to the image is a table of surface oxygen ion

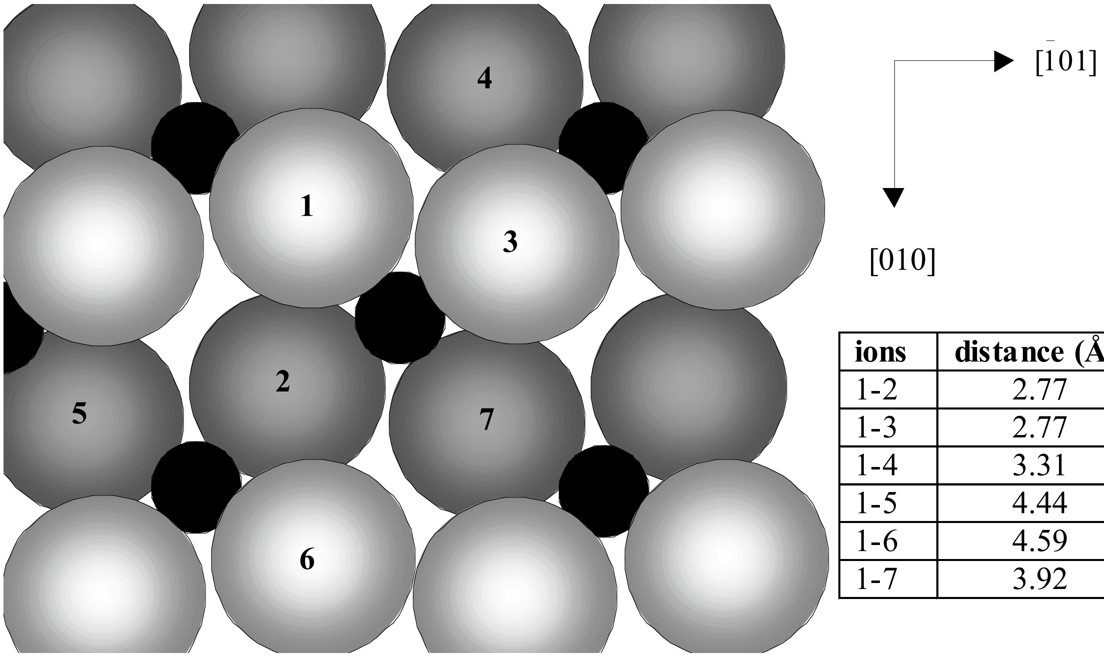

ions	distance (Å)
1-2	2.77
1-3	2.77
1-4	3.31
1-5	4.44
1-6	4.59
1-7	3.92

Figure 5.14—The distances between oxygen ions on the unreconstructed {011} surface.

distances for the seven numbered oxygen ions in the image. To determine epitaxy, these distances will be compared to the interatomic distances in metallic silver.

Metallic silver has a face-centered cubic unit cell with a cube length of 4.07 Å, and the {111} plane is close packed. The Ag-Ag distance is 2.88 Å along the ⟨110⟩, which is 3.8% larger than the distance between the oxygen ions in the 1-2 and 1-3 pairs. Therefore, silver ions that lie on neighboring oxygen ions will be close to their equilibrium distance in bulk silver.

However, the 2.77 Å distance between certain oxygen pairs on the rutile {011} surface is not unique; it also exists between certain pairs of oxygen ions on the rutile {010} surface. It is also clear from Figure 5.14 that the symmetry of the unreconstructed rutile {011} plane is not the same as the 6-fold symmetry of the silver {111} plane. The silver atoms will be surrounded by only four in-plane nearest neighbors, not the six in-plane nearest neighbors expected in the silver {111} plane.

When we examine other low-index rutile planes, we find that the rutile {010} plane is the close-packed plane for oxygen in rutile and therefore, may provide better epitaxy with the silver {111} plane. Figure 5.15 shows a model of the {010} plane

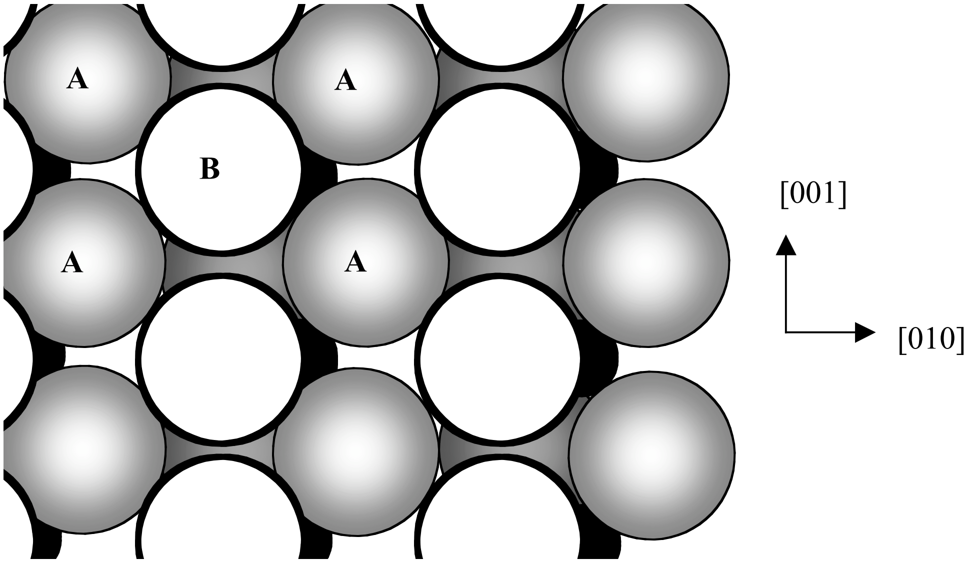

Figure 5.15—A schematic of the rutile {010} plane. The small black ions are Ti, and the large ions are O. The light gray O ions are slightly above the Ti plane, while the darker gray O ions are slightly below it. The fifth O ion coordinating the Ti from beneath is not shown. The white O ions are missing from the {010} surface, but they would be the sixth coordinating O ions in the bulk.

assuming that the sixth coordinating oxygen is present, which is present in the bulk and is depicted as large, white circles in Figure 5.15. The surface oxygen ions form a distorted hexagonal arrangement with an inter-ionic distance of 2.77 Å, which is 3.8% smaller than the interatomic distance in silver. If four silver atoms adsorbed onto the oxygen ions labeled A in Figure 5.15, we can envision a fifth silver atom bonding to them directly above the oxygen ion labeled B. Therefore, even though the oxygen ion labeled B in Figure 5.15 does not really exist on the {010} surface, a silver atom could bond to silver atoms already on the surface just as if the oxygen ion were there. Therefore, it seems likely that the epitaxy would be better between the rutile {010} surface and the silver {111} plane than between the rutile {011} surface and the silver {111} plane.

It is possible, however, that epitaxy would exist between the rutile {011} surface and another silver plane. For example, the presence of four in-plane nearest neighbors for the oxygen ions on the rutile {011} surface implies that it may have good epitaxy with the silver {100} plane because silver atoms in the {100} plane have only 4 in-plane nearest neighbors. The in-plane nearest neighbor distance for silver is 2.88 Å, and silver atoms in the {100} plane should form a centered square with side lengths of 4.07 Å. The

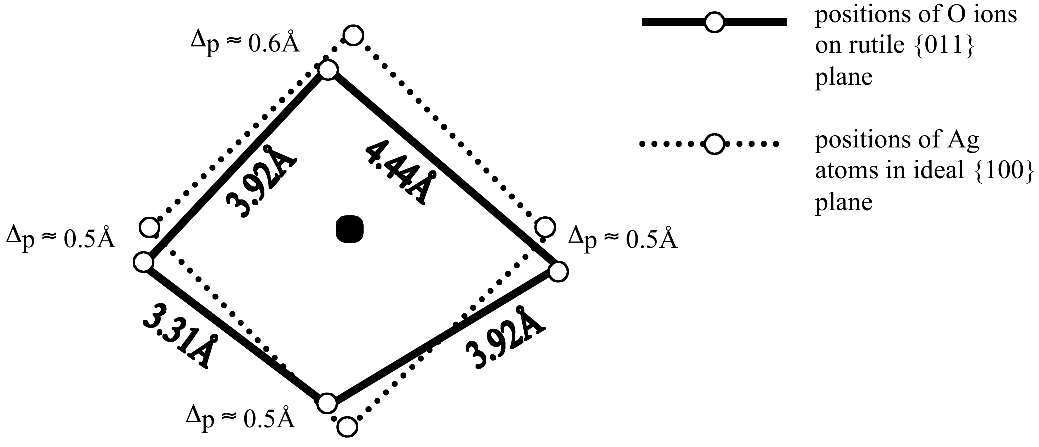

Figure 5.16—A schematic comparing the position of oxygen ions on the rutile {011} surface and the ideal silver {100} plane. The dark circle is a silver atom adsorbed on an oxygen ion. Distances between oxygen ions are listed along each connecting ligand. Δp is the distance between the ideal position of the silver atom in the {100} plane and the position of the silver atom if it remains directly above the oxygen ion.

distances between the appropriate oxygen atoms on the rutile {011} surface lead to a quadrilateral that is shown schematically as the black outline in Figure 5.17. The black circle in the center represents a silver atom bound to the oxygen ion labeled 1 in Figure 5.14. The dotted outline represents the ideal positions of the nearest neighbor silver atoms in the {100} plane. The displacements of the silver atoms attached to the surface oxygen ions are greater than 0.4 Å from their equilibrium positions on the {100} surface. We believe that these displacements, which are greater than 14% of the ideal Ag-Ag bond length, are too great to support epitaxy. Therefore, we conclude that epitaxy between the silver {100} plane and the unreconstructed rutile {011} surface is not favorable. Because epitaxy is not favorable on the rutile {011} surface, which is highly active, and may be favorable on the rutile {010} surface, an inactive surface, we conclude that the high photochemical activity of the rutile {011} surface is not due to an epitaxial relationship between the rutile {011}surface and silver.

Another possibility is that the silver is oxidized as it deposits on the rutile surface, forming Ag_2O. Although we do not believe that this is occurring, a close examination of the Ag_2O structure also shows that an epitaxial relationship does not exist between the unreconstructed rutile {011} surface and Ag_2O.

Effect of Silver Diffusion Across Rutile Surface

As mentioned previously, it is possible that the overall appearance of the crystallites would be identical if the silver ions were reduced on all crystallites equally well but then desorbed from crystallites without {011} facets and readsorbed onto crystallites with {011} facets. To do this, the silver atoms would have to diffuse through water or along the surface from the crystallite where they were reduced to the nearest crystallite with {011} facets within the time limit of the silver photoreduction experiments (approximately 300 s).

The average crystallite is approximately 50 μm across. In general, all crystallites are within four times this distance, or 200 μm, of a crystallite with {011} facets. Although we could not find data on the diffusion of silver metal atoms in water, we found data for the room temperature diffusivity of metallic silver in mercury, 1.05×10^{-5} cm^2/s [3]. This value has the same order of magnitude as the diffusivity of dilute organic compounds in water and various metals in other liquid metals, including molten metals at high temperature and mercury at room temperature [3]. Thus, it seems reasonable that the value of the diffusivity of metallic silver atoms in water will have the same order of magnitude. Using this value for diffusivity and the diffusion distance equation,

$$x = \sqrt{2Dt} \tag{5.1}$$

where x is the RMS distance that silver atoms move in t seconds assuming random-walk motion and D is the diffusivity of the silver atoms in water. We set $x = 200\times10^{-4}$ cm and solved for t:

$$t = \frac{x^2}{2D} = 19\,\mathrm{s} \tag{5.2}$$

The time required for the silver atoms to diffuse through the water to neighboring crystallites with {011} facets is an order of magnitude less than the time scale of the photoreduction experiment. The diffusivity of silver atoms across the rutile surface would be much smaller than this value, so if the diffusion is occurring across the surface and not through the water, the time required for the silver atoms to diffuse 200 μm would be much greater. However, using the above diffusivity value, the possibility exists that the anisotropic silver deposits are due to the anisotropic adsorption of metallic silver on crystallites with {011} facets instead of the anisotropic photoreduction of the silver ions.

However, other physical evidence makes this unlikely. First, because we see silver deposits only on those crystallites that have been illuminated, it is unlikely that the neutral silver atoms desorb from the rutile surface and then readsorb somewhere else on the surface. If the neutral silver atoms had completely desorbed and then readsorbed elsewhere, we would expect to see them on all of the crystallites with {011} facets within approximately 1 mm of the illuminated spot, not on just those crystallites that were illuminated. However, we only see silver on illuminated crystallites, which implies that the neutral silver atoms remain adsorbed on the surface.

Second, if we assume that the silver atoms diffuse along the surface, it is reasonable to expect that the silver atoms would attach to either the first crystallites with {011} facets or the first silver deposit that they reach. This would lead to a clustering of silver near the grain boundaries of crystallites with {011} facets that would be exacerbated by the ability of the metallic silver to act as an electron trap and to increase the photoreduction rate. If the diffusion of silver across the surface were occurring, we would expect to see more silver near the grain boundaries of these crystallites than near the center. However, as Figure 5.1 shows, there is no measurable difference in the number of silver deposits between the center of the heavily covered crystallites and the area near the grain boundaries. From this, we conclude that the silver on the crystallites with {011} facets is being reduced by these crystallites and not diffusing to them from the surrounding crystallites, although there may be enough time for the diffusion to occur.

5.5.2.2 Chemistry Effects

We conclude from the analysis in the previous section that the differences in the amounts of silver on crystallites with different orientations are due to differences in the photoreduction rates of silver ions. The following sections examine the changes in various surface properties, such as surface energy, water adsorption, titanium ion densities, and impurity concentrations, with orientation and how these changes might effect photochemical activity.

Surface Energy

As discussed in §2.6.3.2, adsorption on rutile is affected by the surface orientation, and the expectation is that the photocatalytic activity will be influenced by the same. Adsorption is the first step in the photocatalytic cycle. Because electron-hole recombination occurs so quickly in semiconductors, adsorbates or other traps must already exist on the surface for any reduction or oxidation to occur [4]. Therefore, surfaces that are covered with a higher density of adsorbates may have a greater chance for further reactions to occur than surfaces that are only sparsely covered with adsorbates. As discussed in §2.1.1, one theory explaining photocatalysis proposes that the adsorbate in most photocatalytic reactions is the hydroxyl group, OH^-. In this process, the hydroxyl group is oxidized to $^{\bullet}OH$, which then desorbs from the surface. The remaining electron is available to reduce Ag^+ to Ag^0. Once enough silver has been reduced, the silver acts as an electron sink, increasing the photoreduction rate [5, 6]. The promotion of continued reduction reactions at the initial site of the silver reaction leads to an island morphology.

For this process to begin, there must be sterically unhindered sites available at the surface that can bond to hydroxyl groups or to silver ions. Surfaces or facets with different orientations have different numbers of sites that are available for bonding to adsorbates. The undersaturation of surface titanium ions is one possible measure of the number of available adsorption sites on a surface. The undersaturation of titanium ions is also the prime determinant of the surface energy of a given orientation. For example, the 5-coordinate titanium density is 5.2 Ti^{4+}/nm^2 on the unreconstructed {110} surface, 7.4 Ti^{4+}/nm^2 on the unreconstructed {010} surface, and 8.0 Ti^{4+}/nm^2 on the unreconstructed {011}surface, so we would expect that the {110} surface would have the smallest surface energy, followed by the {010} and {011} surfaces in that order. We would also expect that if all undersaturated titanium ions on a surface were potential active sites for adsorption, more stable orientations, i.e., orientations with the lowest undersaturation or highest coordination, should be less catalytically, while less stable orientations should be more catalytically active.

This explanation, however, is not consistent with our observations about relative surface energies. Our observations indicate that {011} is the most stable orientation for rutile at the annealing temperatures used in this experiment (see Table 4.3). Therefore, the differences in surface energy as measured in this study do not correlate to differences in photochemical activity or to 5-coordinate titanium densities, so the simple assumption that the majority of the undersaturated titanium ions on the surface are adsorption sites does not appear to be true for the rate limiting reaction.

Adsorption anisotropy

The ability of a surface to adsorb molecules is not solely related to surface energy. For example, a high-energy rutile surface with titanium ions that are obstructed by oxygen ions will probably adsorb fewer water molecules than a low-energy surface with unobstructed titanium ions. Therefore, we need to look specifically at the adsorption behavior of the low-index surfaces rather than relying solely on the surface energy.

Several studies have been completed that examined the adsorption on water onto low-index surfaces of rutile. As discussed in §2.6.3.2, most studies have determined that molecularly adsorbed water on the rutile {110} surface desorbs below 300 K, but work by Hugenschmidt et al. [7] found that approximately one-quarter of a monolayer of water is stable on the rutile {110} surface as hydroxyl groups. The oxygen atom in each water molecule that adsorbs dissociatively initially bonds to a 5-fold coordinate Ti^{4+}. One of the hydrogen atoms then bonds to a bridging oxygen ion. Therefore, there are hydroxyl groups on the {110} surface available for the oxidation half of the photocatalytic cycle.

Work by Henderson [8] showed that approximately 0.3 monolayers of water remain dissociatively adsorbed on the stoichiometric rutile {010} surface until the temperature exceeds 350 K. Anything more than 0.3 monolayers is adsorbed molecularly on the stoichiometric rutile {010} surface and desorbs at 250 K. Henderson [8] also hypothesized that the initial adsorption occurs on 5-fold coordinate Ti^{4+} ions.

Although research has been done to examine the adsorption of water onto defective rutile surfaces [8–13] with both oxygen vacancies and Ti^{3+} sites, no research has examined the adsorption of water onto an illuminated rutile surface with Ti^{3+} sites and very few oxygen vacancies. Based on the adsorption behavior of the rutile {010}(1×3) surface, which contains a regular array of Ti^{3+} sites, Henderson [8] hypothesized that the presence of Ti^{3+} sites does not affect the adsorption behavior of water. If we extend his hypothesis to illuminated surfaces, we can assume that the illumination does not affect the water adsorption properties.

In addition, no one has examined the adsorption behavior of water on {011} surfaces, so we do not know if it is markedly different from the adsorption behavior of water on {110} or {010} surfaces. However, adsorption experiments on rutile powder composed of particles bound by {011}, {110}, and {010} facets in a 1:3:1 ratio found that the density of hydroxyls on the powder surface was much greater than the density on {110} or {010} single crystals surfaces [14]. Assuming that defects had a minimal effect on the adsorption properties of the powder, one possible reason for the greater adsorption is that the {011} has a much greater density of hydroxyl adsorption sites than either the {110} or the {010}.

However, assuming that all 4- and 5-coordinate titanium ions adsorb water equally well, there is no simple reason to expect the {011} surface to adsorb more hydroxyls. As discussed earlier, the titanium ion density on the {011} surface is 8.0 Ti^{4+}/nm^2, which is only slightly greater than that of the {010} surface—7.4 Ti^{4+}/nm^2—and less than twice as large as that of the {110} surface—5.2 Ti^{4+}/nm^2—or that of the {001} surface—4.7 Ti^{4+}/nm^2. This simple analysis indicates that the adsorption behavior of water on the {011} surface should be similar to that of the {010} surface and that slightly more than one-third of a monolayer of water exists on the {011} surface as hydroxyls.

However, even though the densities of titanium ions on the {010} and {011} surfaces are almost the same, the distance between nearest neighbor titanium ions on the {011} surface is 3.57 Å, while the distance between nearest neighbor ions on the {010} and {110} surfaces is 2.96 Å. It is possible that the additional space between the titanium ions on the {011} would allow a water molecule or hydroxyl ion to adsorb to neighboring titanium ions, while steric and electrostatic interactions between water molecules or hydroxyl ions would prevent adsorption on neighboring titanium ions on the {010} and {110} surfaces. This would effectively halve the number of adsorption sites on the {010} surface from 7.4 Ti^{4+}/nm^2 to 3.7 Ti^{4+}/nm^2 and on the {110} surface from 5.2 Ti^{4+}/nm^2 to 2.6 Ti^{4+}/nm^2. This could explain the enhanced hydroxyl adsorption on powders containing {011} facets [14] and partially explain the enhanced photochemical activity of the {011} surface.

Differences in Vacancy Environments

The analysis in the previous section was based on the assumption that the 4- and 5- coordinate titanium ions were equivalent. This may not be true in the area surrounding an oxygen vacancy. Although we made an effort to ensure that the rutile crystallites were fully oxidized, there are always oxygen vacancies on the surface and in the bulk at the annealing temperatures used in this thesis. The environment around oxygen vacancies can be different on each plane. Assuming equal vacancy concentrations on all surfaces, one possible reason for the differences in photochemical activity is that oxygen vacancies on the {011} surface provide an environment that is more favorable to water adsorption than on the less-active surfaces. Therefore, we will now examine the environment around the oxygen vacancies on unreconstructed surfaces to determine if they are substantially different on the various low-index planes.

Figure 5.17 shows a schematic of the unreconstructed {011} surface with an oxygen vacancy. The large gray square represents the oxygen vacancy. The coordination of the two white titanium ions has been reduced from five to four. The distance between the lighter oxygen ions on either side of the vacancy is 5.46 Å, and the distance between the darker oxygen ions on either side of the vacancy is 4.59 Å. The distance between the white titanium ions is 3.57 Å.

Figure 5.18 shows a schematic of the unreconstructed {010} surface with an oxygen vacancy. Again, the large gray square represents the oxygen vacancy. Like the {011} surface, the coordination of the two white titanium ions has been reduced from five to four. The distance between the lighter oxygen ions on either side of the vacancy is 5.92 Å, and the distance between the darker oxygen ions on either side of the vacancy is 4.59 Å. The distance between the white titanium ions is 2.96 Å.

Figure 5.19 shows a schematic of the unreconstructed {110} surface with two types of oxygen vacancies. The first oxygen vacancy type, labeled V1 in Figure 5.19, is a missing bridging oxygen ion. The coordination of the two white titanium ions on either

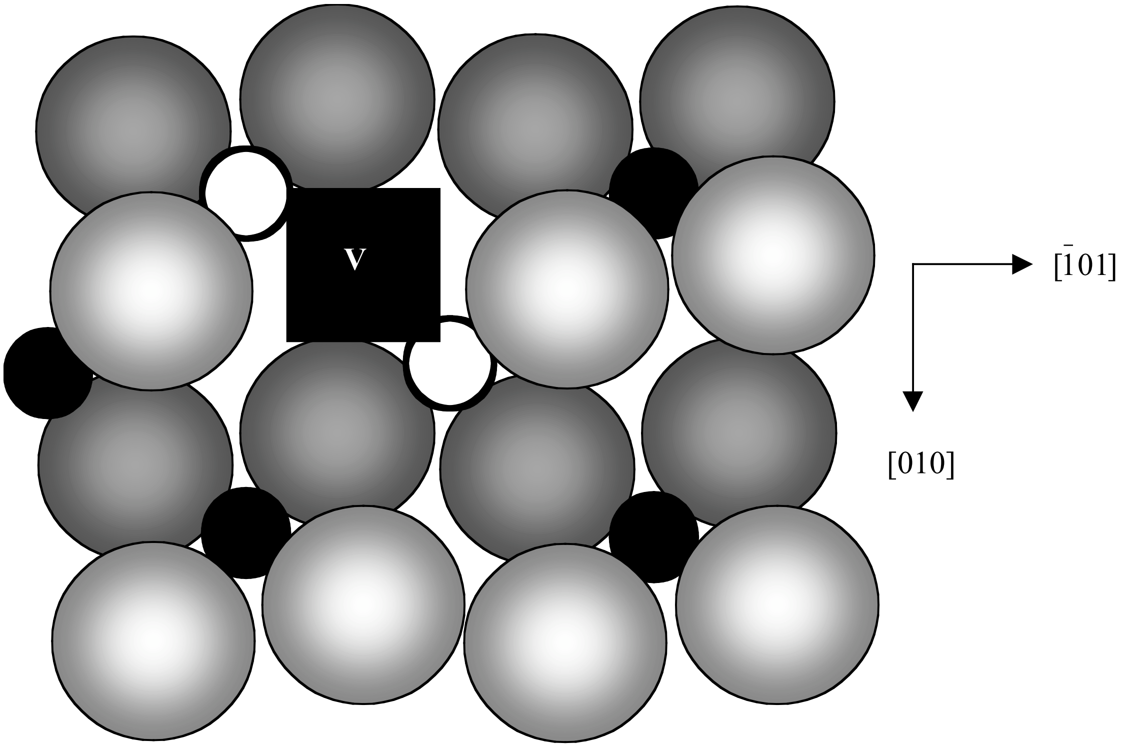

Figure 5.17—A schematic of the rutile {011} surface with an O vacancy. The small ions are Ti while the larger ones are O. Lighter O ions are slightly above the Ti plane, and darker O ions are slightly below the Ti plane. The black square is the vacancy.

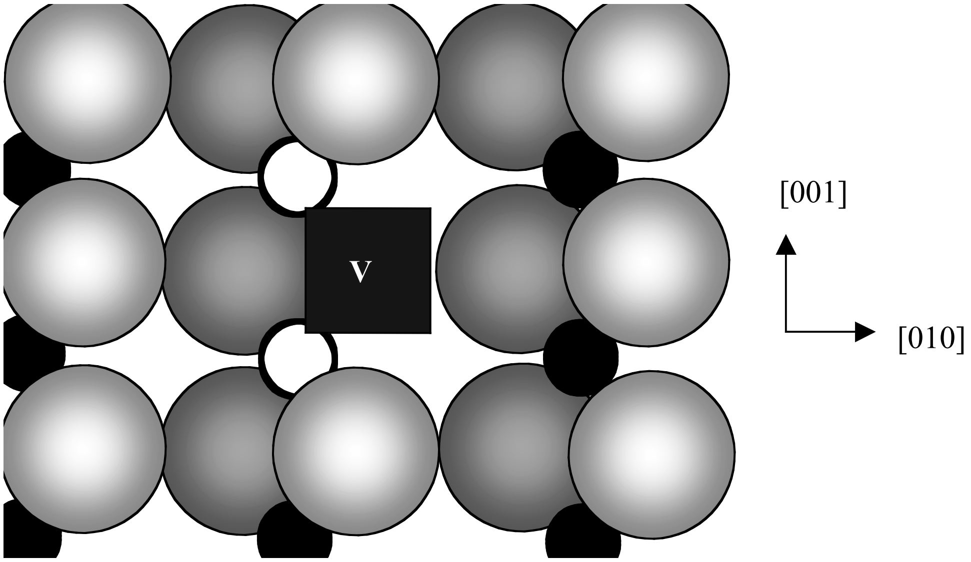

Figure 5.18—A schematic of the rutile {010} surface with an O vacancy. The lighter O ions are slightly above the Ti plane, while the darker O ions are slightly below it. The black square is the vacancy.

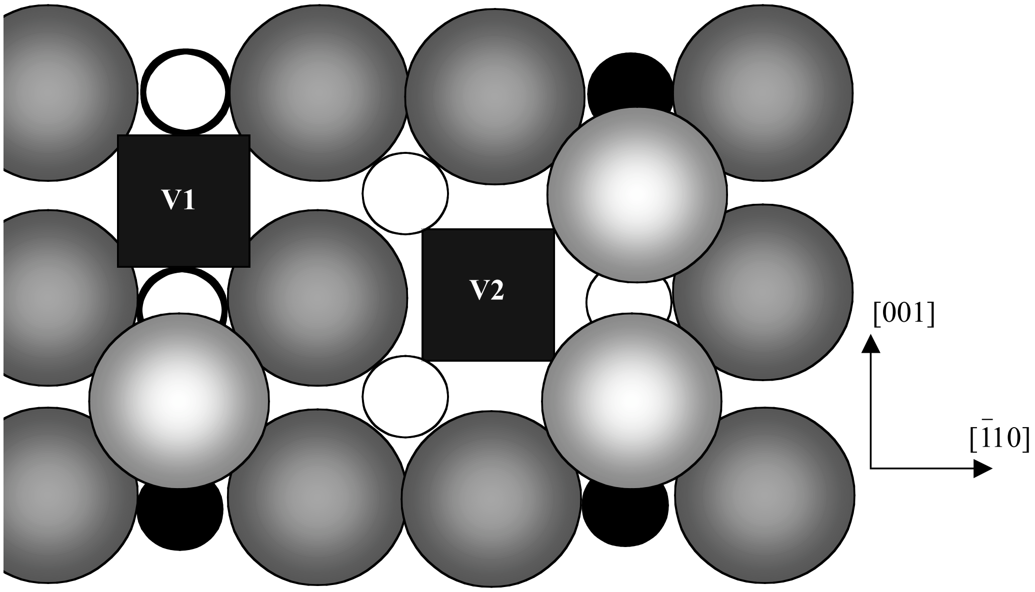

Figure 5.19—Schematic of rutile {110} with an O vacancy. The lighter O ions are the bridging O. The gray square labeled V1 is a vacancy in the bridging O, and the gray square labeled V2 is a vacancy in the non-bridging O.

side of the vacancy has been reduced from six to five. The second oxygen vacancy type is labeled V2 in Figure 5.19. The coordination of the two titanium ions filled with dots in Figure 5.19 has been reduced from five to four, and the coordination of the titanium ion filled with a grid has been reduced from six to five.

The coordination environment around the two oxygen vacancy types on the rutile {110} surface are different from the environment around the oxygen vacancy on the {011} surface. The local environments around oxygen vacancies on the unreconstructed {010} and {011} surfaces appear more similar. The coordination of the titanium ions surrounding the vacancy is identical in each case, and the distances between the surrounding oxygen ions are similar. However, the distances between the titanium ions are significantly different. The distance between the titanium ions around the oxygen vacancy on the unreconstructed {011} surface is more than 0.5 Å larger than the distance between the titanium ions around the oxygen vacancy on the unreconstructed {010} surface. As mentioned previously, it is possible that the additional space between the titanium ions would allow a water molecule or hydroxyl ion to bond to both titanium ions near the vacancy, while steric and electrostatic interactions would allow only one water molecule or hydroxyl ion to bond to the titanium ions near the vacancy on the {010}. Assuming equal numbers of oxygen vacancies on each surface, this would allow the {011} to adsorb more water molecules or hydroxyl ions than the {010}, which could lead to the higher activity. Therefore, assuming unreconstructed surfaces, it seems as though the oxygen vacancies on the {011} could be partially responsible for the large photocatalytic activity of the {011}.

Effect of Impurities

From the AES results, we know that there are silicon and calcium impurities on the surfaces of the crystallites. As discussed in §3.3.4.2, the results from AES also show that the impurity levels on the surfaces of the inactive crystallites were greater than the impurity levels on the surfaces of the active crystallites. To examine whether the impurity concentrations on the surfaces of the inactive crystallites were great enough to influence the photochemical activity, we compared the quantum yield of several crystallites near {010} to the quantum yield of several {010} oriented rutile thin films. We found that the quantum yield of the crystallites, 0.008 Ag^0/photon, was an order of magnitude smaller than the quantum yield of the thin films, 0.06 Ag^0/photon, indicating that the impurities are acting as recombination centers and lowering the photochemical activity of the crystallites. Because the surface impurity concentrations are greater on the inactive crystallites than on the active crystallites, their effect is greater on the inactive crystallites, lowering their photochemical activities more than they lower the photochemical activities of the active crystallites. However, there is more than an order of magnitude difference in the amount of silver on the most active crystallites, which are completely covered with silver, and the least active crystallites. Therefore, increasing the quantum yield of the least active crystallites by an order of magnitude would not increase their photochemical activity enough that they would be as active as the most active crystallites. Therefore, we conclude that the silicon and calcium impurities only accentuate an anisotropy that already exists and are not the sole reason behind the large differences in photochemical activity that are observed between crystallites with {011} facets and those without {011} facets.

5.6 Limitations of Polycrystals

Examining the photochemical activity of polycrystals has many advantages over examining the photochemical activity of single crystals and thin films. The biggest advantage is that the photochemical activity of many more orientations can be examined than would be feasible to create using single crystals. On the other hand, the orientations of the crystallites are random, so it is sometimes difficult or impossible to find a crystallite with a particular orientation. In addition, the compaction and sintering of polycrystals inevitably leads to the incorporation of impurities, such as silicon and calcium. Therefore, experiments on rutile thin films with low-index orientations and high purity were used to confirm the observations made on the polycrystals. These results will be discussed in the next chapter.

5.7 Summary

The photochemical activity of rutile is strongly dependent on the presence of {011} facets on the surface of the crystallite and is not due to bulk processes such as anisotropic electrical conductivity or light adsorption. The photochemical activity depends on special sites on the {011} surface or on special sites on the intersections between {011} and neighboring facets. The data support both models and leave open the possibility that the photochemical properties depend on both surface features.

The appearance of large numbers of silver deposits on crystallites with {011} facets is due to photochemical processes and not to the surface diffusion of silver from other crystallites. Assuming that the {011} facets do not reconstruct at the annealing temperatures used in this study, the high photochemical activity of the {011} surface is also not due to an epitaxial relationship with either Ag_2O or metallic silver. The high photochemical activity may be partially due to the increased distance between neighboring titanium ions on the {011} surface. The high relative activity of the surfaces with {011} facets may also be partially due to the enrichment of the inactive surfaces with silicon and calcium. The main conclusion is that the {011} is important to the high photochemical activity of rutile.

5.8 References

[1] P. Kofstad, "Nonstoichiometry, Diffusion, and Electrical Conductivity in Binary Metal Oxides," Robert E. Krieger Publishing Company, Malabar (1983).

[2] J. Goodenough, A. Hamnett, G. Huber, F. Hulliger, M. Lieb, S. Ramasesha, and H. Werheit, *in* "Landolt-Bornstein, Numerical Data and Functional Relationships in Science and Technology" Vol. 17, Subvol. g, Chap. 9.15.2.1, (K.-H. Hellwege and O. Madelung, Eds.), p133, Springer-Verlag, New York (1984).

[3] R. Chabra *in* "CRC Handbook of Chemistry and Physics, 70th ed.", (R. Weast, D. Lide, M. Astle, and W. Beyer, Eds.), pF51, CRC Press, Boca Raton (1989).

[4] G. Rothenberger, J. Moser, M. Grätzel, N. Serpone, and D. Sharma, *J. Am. Chem. Soc.* **107** (1985) 8054.

[5] H. Gerischer and A. Heller, *J. Phys. Chem.* **95** (1991) 5161.

[6] J. Kesselman, G. Shreve, M. Hoffman, and N. Lewis, *J. Phys. Chem.* **98** (1994) 13385.

[7] M. Hugenschmidt, L. Gamble, and C. Campbell, *Surf. Sci.* **302** (1994) 329.

[8] M. Henderson, *Surf. Sci.* **319** (1994) 315.

[9] V. Henrich, G. Dresselhaus, and H. Zeiger, *Solid State Commun.* **24** (1977) 623.

[10] R. Kurtz, R. Stockbauer, T. Madey, E. Román and J. de Segovia, *Surf. Sci.* **218** (1989) 178.

[11] G. Lu, A. Linsebigler, and J. Yates, Jr., *J. Phys. Chem.* **98** (1994) 11733.

[12] L. Wang, D. Baer, and M. Engelhard, *in* "Materials Research Society Symposium Proceedings Volume 357: Structure and Properties of Interfaces in Ceramics", (D. Bonnell, M. Rühle, and U. Chowdhry, Eds.), p97, Materials Research Society, Pittsburgh (1995).

[13] J. Pan, B. Maschhoff, U Diebold, and T. Madey, *J. Vac. Sci. Technol. A* **10** (1992) 2470.

[14] D. Beck, J. White, and C. Ratcliffe, *J. Phys. Chem.* **90** (1986) 3123.

Chapter 6

Thin Films

The previous two chapters discussed the orientation stability and photocatalytic activity of rutile polycrystals annealed at 1473 K and 1273 K. The biggest advantage of using randomly-oriented polycrystals over oriented thin films or single crystals in this study is that a much larger percentage of orientation space can be examined efficiently. However, the use of polycrystals has its disadvantages, such as the difficulty of controlling impurities. The thin films used in these experiments were grown from the purest available starting materials, allowing us to examine a limited number of orientations where the impurity concentration was minimized.

The research presented in Chapters 5 and 6 was motivated by experiments originally conducted at DuPont. Using the procedures outlined in §3.2.1 and §3.2.3, Hotsenpiller et al. [1] measured the change in optical density with respect to time as silver was reduced on the surface of {010}, {011} and {001} oriented thin films. Their results indicated that the {001} oriented thin film was more active than the {011} oriented thin film, which was more active than the {010} oriented thin film. These observations are apparently inconsistent with the results presented for the polycrystals. These results motivated the microscopic studies presented in this chapter.

6.1 Morphology of Thin Films

6.1.1 {011} Rutile

Various {011} oriented thin films of three thicknesses—700 Å, 2100 Å, and 4500 Å—were examined. A representative image of a 4500 Å thick {011} oriented rutile thin film grown on $Al_2O_3\{11\bar{2}0\}$ taken with contact AFM is shown in Figure 6.1. The

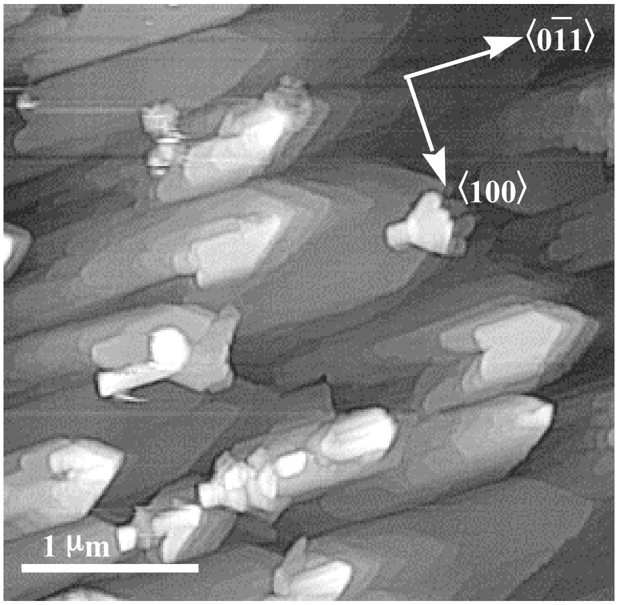

Figure 6.1—An AFM image of a 4500 Å thick {011} oriented rutile thin film grown on Al_2O_3 $\{11\bar{2}0\}$.

surfaces of the films are composed of elongated, faceted islands with apparent vertical heights of 50–80 Å. Backscattered Laue diffraction was used to determine that the direction of elongation is parallel to $\langle\bar{1}100\rangle_{Al_2O_3}$, which is assumed to be parallel to $\langle\bar{1}01\rangle_{TiO_2}$ based on previous studies of the epitaxy [2]. While the aspect ratios of the faceted islands remain approximately constant over any given thin film, they do not remain constant over a group of thin films with the same nominal thickness.

A schematic of the facets on the {011} oriented rutile thin films is shown in Figure 6.2. The predominant facet present on the {011} oriented rutile film is the {011} facet. The {011} facet is stable and within a very small angle of the surface, assuming a small substrate miscut. The two facets whose intersections with the surface are inclined to both the ⟨100⟩ and the $\langle 0\bar{1}1\rangle$ are probably also {011} planes. {011} planes should intersect the surface along $\langle 1\bar{1}1\rangle$ directions, and the intersection angle of the appropriate $\langle 1\bar{1}1\rangle$ directions is 80º, approximately the same as that measured with the AFM. The long side facets that intersect the surface along the $\langle 0\bar{1}1\rangle$ are probably {111} facets.

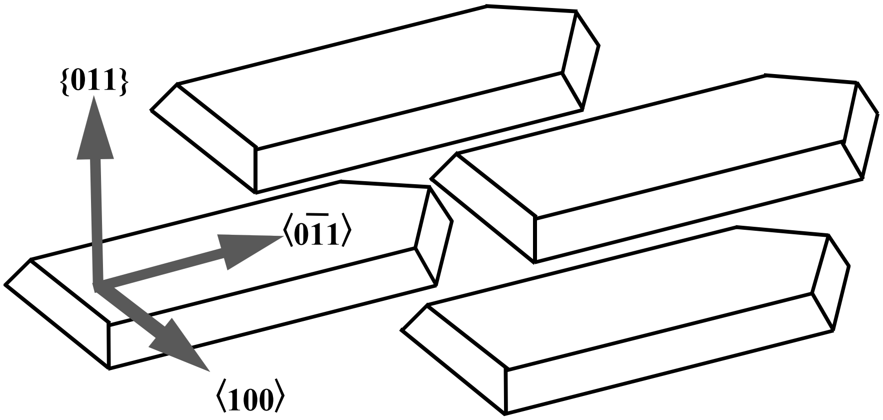

Figure 6.2—A schematic of the facets on the {011} oriented rutile thin film.

6.1.2 {010} Rutile

Three {010} oriented thin films of different thicknesses—700 Å, 2100 Å, and 4500 Å—were examined. A representative image of a 2100 Å thick {010} oriented rutile thin film grown on Al_2O_3{0001} taken with contact AFM is shown in Figure 6.3. The surfaces of the films are composed of elongated islands. Backscattered Laue diffraction was used to determine that the long axis is oriented parallel to $\langle 1\bar{2}10\rangle_{Al_2O_3}$, which is

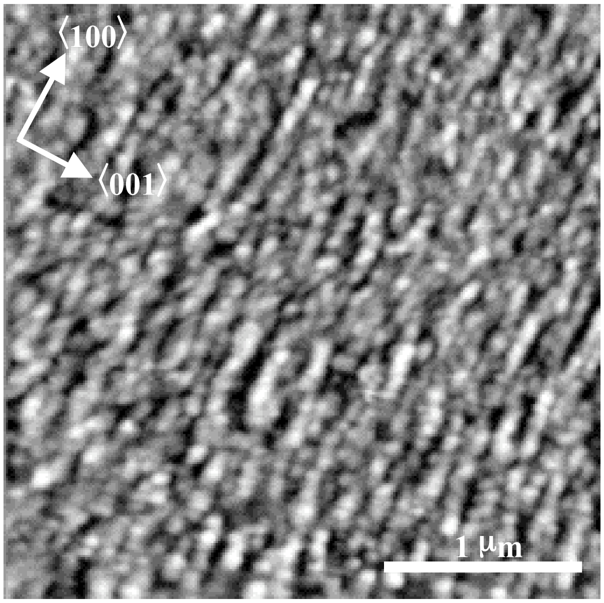

Figure 6.3—An AFM image of a 2100 Å thick {010} oriented rutile thin film grown on Al_2O_3{0001}.

assumed to be parallel to $\langle 100\rangle_{\mathrm{TiO_2}}$ based on previous studies of the epitaxy [2]. The elongation becomes more pronounced as the thickness of the films increases. All of the thin films are flat and have RMS roughnesses of 5–7 Å. The heights of most surface features are approximately 10 Å.

Unlike the {011} oriented thin film, the {010} oriented thin film does not appear to be composed of sharp facets but of rounded features, similar to, but smaller than, the rounded facets seen in Figure 4.20. On the other hand, the presence of the rounded features in the AFM images may be due to the inability of the AFM probe to accurately image sharp features with dimensions on the order of the probe's radius. Based on this observation, it was assumed that the rounded texture visible in the AFM images is caused by small facets. Figure 6.4 shows one possible configuration of facets that could produce an AFM image similar to that shown in Figure 6.3. In this schematic, it is assumed that the edges between the facets are straight. However, from Figure 4.20, we know that this need not be true.

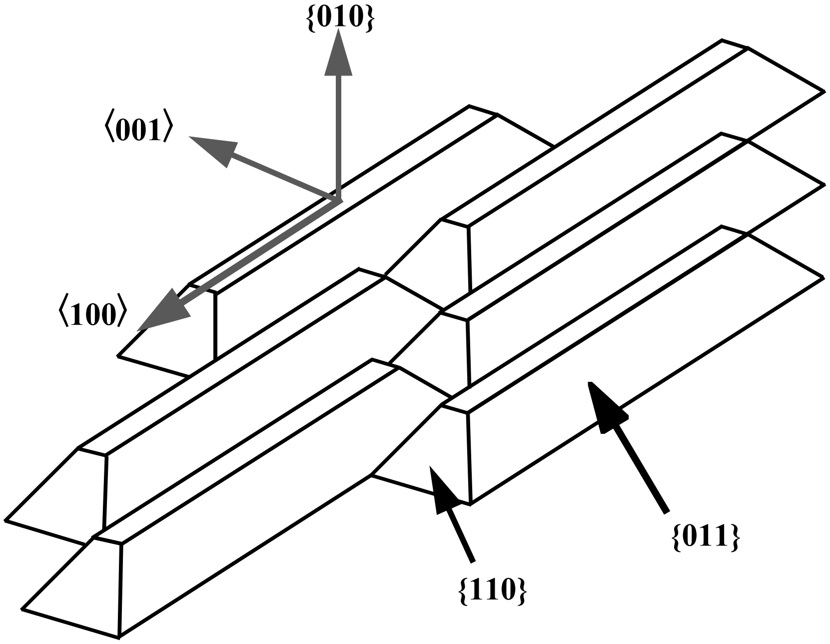

Figure 6.4—A schematic of the facets on the {010} oriented rutile thin film.

Assuming that the miscut of the substrate is small, the orientation of the predominant facet is {010}, which is stable at 998 K. If the region labeled A in the orientation stability figures at 1273 K and 1473 K does not exist at the 998 K, the orientations of the facets that intersect the surface along the ⟨100⟩ are probably {011}, and the orientations of the facets that intersect the surface along the ⟨001⟩ are probably {110}. However, if a region equivalent to that labeled A does exist at 998 K, the side steps have complex orientations. Because the {010} oriented thin film is smooth and has an RMS roughness less than 10 Å, the side facets are more accurately labeled steps.

6.1.3 {001} Rutile

Various {001} oriented thin films of two thicknesses—700 Å and 2100 Å—were examined. A representative image of a 2100 Å thick {001} oriented rutile thin film grown on $Al_2O_3\{10\bar{1}0\}$ taken with contact AFM is shown in Figure 6.5. The surface of the 2100 Å thick film is composed of equiaxed, faceted pits. Backscattered Laue

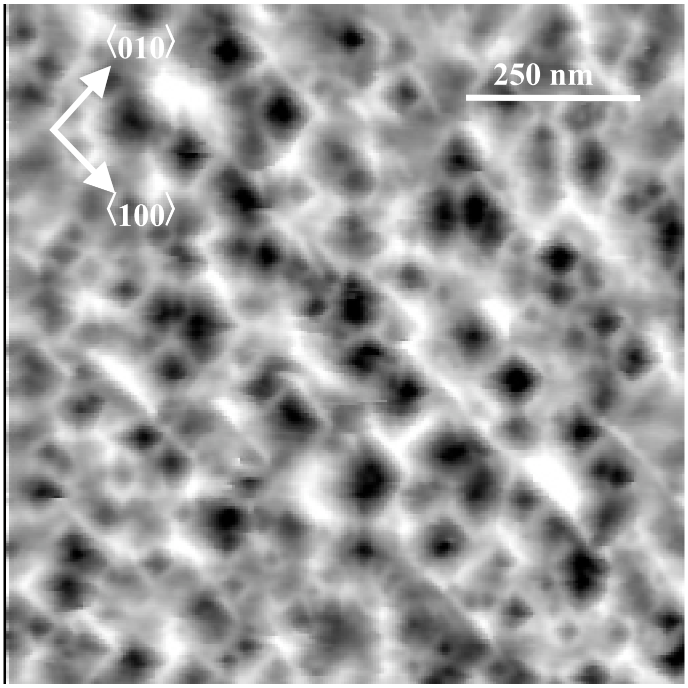

Figure 6.5—An AFM image of a 2100 Å thick {001} oriented rutile thin film grown on $Al_2O_3\{10\bar{1}0\}$.

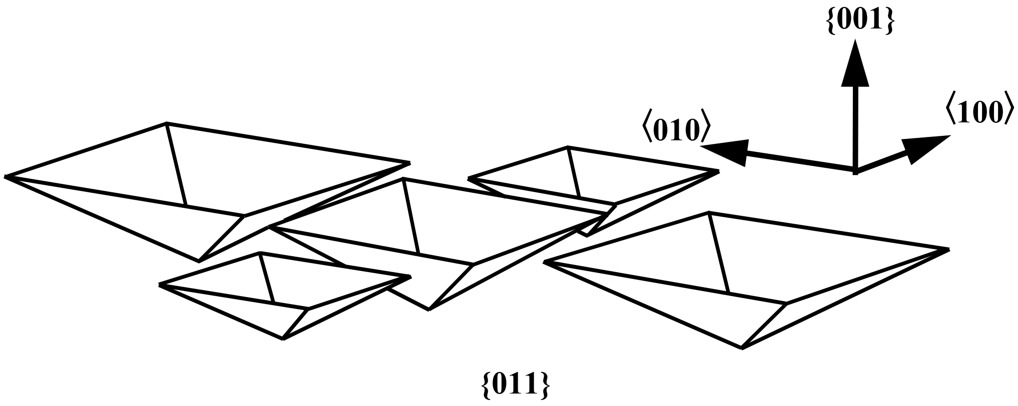

Figure 6.6—A schematic of the facets on the {001} oriented rutile thin film.

diffraction was used to determine that the pit edges are oriented along $\langle 1\bar{2}10\rangle_{Al_2O_3}$ and $\langle 0001\rangle_{Al_2O_3}$, which are assumed to be parallel to $\langle 100\rangle_{TiO_2}$ based on previous studies of the epitaxy [2]

Previous experimental results in vacuum [3] and theoretical calculations at 0 K [4] indicate that the {001} surface is unstable and should facet completely. Although the experimental results discussed in Chapter 4 indicate that the {001} surface is stable with respect to faceting at 1273 K and 1473 K, the range of stability was decreasing as the temperature decreased, and it is not unreasonable that the {001} surface would facet at 998 K. The {001} oriented rutile thin film appears to be completely faceted; a schematic of the facets is shown in Figure 6.6. The orientations of the facets on the sides of the square pyramidal pits are {011} whose intersections with the surface are along ⟨100⟩.

6.1.4 Discussion

The morphology of the thin film surfaces is different from that expected based on the morphology of the polycrystalline grains with similar orientations. The {001} oriented rutile thin film is faceted while crystallites with orientations near {001} are flat. The facets present on the {010} oriented thin film are much smaller than the facets imaged on crystallites with orientations near {010} at 1273 K. The facets on both the {011} and {010} films are characteristically elongated, and the facets on the {011} film appear almost island-like. These differences between the films and the polycrystalline surfaces could be due to misfit between the substrate and film or differences in the growth temperatures of the films and the annealing temperatures of the polycrystal. Finally, we should consider the fact that the polycrystalline surfaces are near equilibrium while the film surfaces are growth forms.

6.1.4.1 Effect of Misfit

The misfit between the substrates and the films is probably the primary reason behind the island-like appearance of the films. The strains are too great to support two-dimensional growth. The experimental evidence suggests that the misfit between the substrate and the film affects the morphologies of the film surfaces even for 2000 Å thick films because the facets are elongated in the direction of lowest misfit. For example, the $\{011\}$ oriented rutile thin film grown on $Al_2O_3\{11\bar{2}0\}$ has a mismatch in the $\langle 100\rangle$ direction, 5.78%, that is much higher than the misfit in the $\langle 0\bar{1}1\rangle$ direction, 0.91% [2]. The anisotropic misfit correlates well with the AFM images showing facets elongated along $\langle 0\bar{1}1\rangle$. In this case, however, misfit is probably not the only factor affecting the elongation of the facets, or the aspect ratio of the facets would remain approximately constant for films of the same thickness. Since films with the same thickness do not necessarily have facets with the same aspect ratios, the miscut of the substrate probably plays a role in determining the morphology of the surface as well.

The results are similar for the $\{010\}$ oriented thin film grown on $Al_2O_3\{0001\}$. For this system, however, the aspect ratio of the facets appears to depend only on the thickness of the film, so the anisotropic misfit is probably the primary reason for the elongated facets.

6.1.4.2 Effect of Temperature

In Chapter 4, we determined the orientations of the stable rutile surfaces at 1273 K and 1473 K. As the temperature decreased from 1473 K to 1273 K, the stable shape of rutile became more sharply faceted, as evidenced by the decreasing range of orientations over which the rutile surface remains flat. We expect that this trend has continued and that the stable shape at the temperature of film growth, 998 K, is more sharply faceted than at either 1273 K or 1473 K. We can speculate that the correct orientation stability figure at 998 K is similar to those at 1273 K and 1473 K, although the region labeled A in Figures 4.3 and 4.11 is probably smaller.

6.1.4.3 Growth Form versus Equilibrium

We must also consider the possibility that the facets on the rutile thin films represent growth forms rather than equilibrium shapes. Typically, growth processes favor the appearance of slow-growing facets in the final morphology, not necessarily those facets with the lowest energy. The faster growing facets simply grow until they reach the edge of the island or film and disappear. Therefore, growth surfaces can give a misleading picture of facet stability. However, the growth rate for these films was slow enough (between 3 Å/min and 7 Å/min [5]) that it is a reasonable assumption that atoms could move to low-energy facets during growth and that the surface is close to equilibrium.

6.2 Photocatalytic Activity

The photocatalytic activity of the thin films was tested by a variety of methods. In addition to the experiments mentioned in the introduction to this chapter, the quantum yield was also measured by the DuPont group. In these experiments, films were exposed to a known photon flux, and the volume of the silver reduced on the surface was then determined using AFM. The quantum yields and photoreduction rates, calculated as the rate of change of the optical density, of the films are listed in Table 6.1 [1]. These results clearly show that the {001} and {011} oriented thin films are much more active than the {010} oriented thin films.

In order to ensure that the deposits on the surface were silver and not residue from the $AgNO_3$ solution, two additional experiments with controls were completed. In the first experiment, {011} and {010} oriented rutile thin films were broken into several

Table 6.1: Quantum Yield Measurements and Photoreduction Rates for Rutile Thin Films

	quantum yield		**photoreduction rates (10^5/s) 365 nm light**
	405 nm light (OD = 0.0022)	**365 nm light (OD = 0.0044)**	
{010}	0.06 (OD = 0.0044)	0.03	0.74
{011}	0.6	0.4	2.1
{001}	1	1	7.4

pieces. A piece of each film acted as a control and was submerged in 0.115 M $AgNO_3$ with no illumination, while another piece of each film was submerged in 0.115 M $AgNO_3$ with illumination. In the second experiment, part of a {001} oriented rutile thin film was masked. The film was then put in 0.115 M $AgNO_3$ and illuminated for 47 minutes. The results and discussion in the next three sections pertain to these two control experiments.

6.2.1 {011} Rutile

A representative image of the illuminated {011} oriented thin film taken with contact AFM is shown in Figure 6.7. Most of the silver islands appear in clusters across the surface, with many of the clusters adjoining the edges of the facets. Each 9 μm^2 area contains 80–100 islands and clusters. Although several apparent surface-screw dislocation intersections were imaged, no silver nucleated in the area surrounding the dislocation. Single silver islands range in size from approximately 500–1300 Å in diameter and from approximately 50–200 Å high. The total amount of silver reduced by the surface is approximately 800 $\mu mol/cm^2$.

6.2.2 {010} Rutile

A representative image of the illuminated {010} oriented thin film taken with contact AFM is shown in Figure 6.8. All of the 9 μm^2 areas that were imaged show fewer than ten silver islands and clusters across the surface. Single island diameters range from approximately 1000–1500 Å, the heights of most islands are approximately

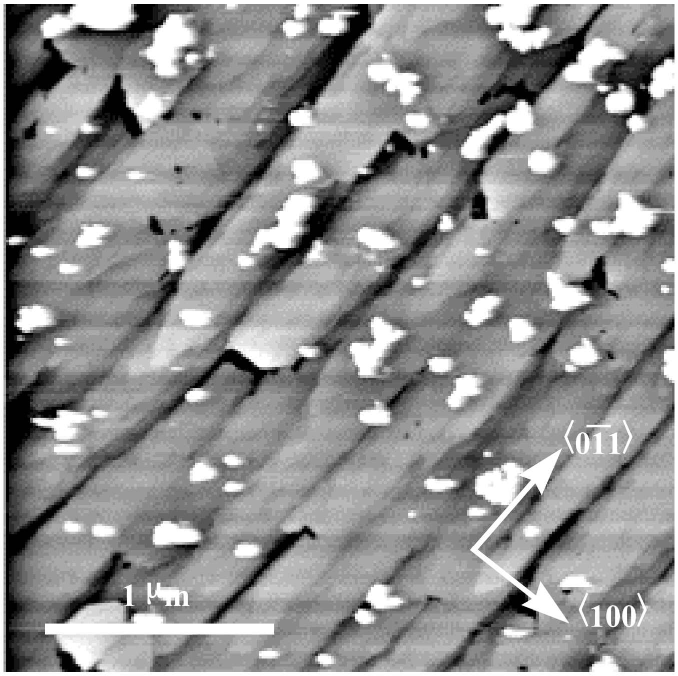

Figure 6.7—The {011} oriented rutile thin film after the silver reduction experiment.

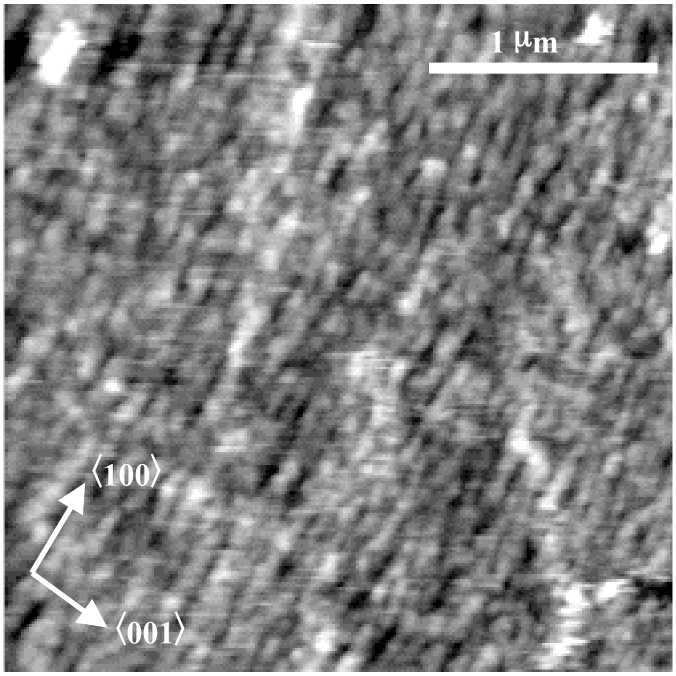

Figure 6.8—The {010} oriented rutile thin film after the silver reduction experiment.

50 Å, and the total amount of silver reduced by the surface is approximately 50 μmol/cm^2.

6.2.3 {001} Rutile

A representative image of the illuminated part of the {001} oriented thin film taken with contact AFM is shown in Figure 6.9. Single island diameters range from approximately 600–1800 Å, and the island heights range from approximately 100–400 Å. Because of the rough surface morphology, the amount of silver on this surface was difficult to determine precisely. It was estimated that the amount of silver is approximately 660 μmol/cm^2.

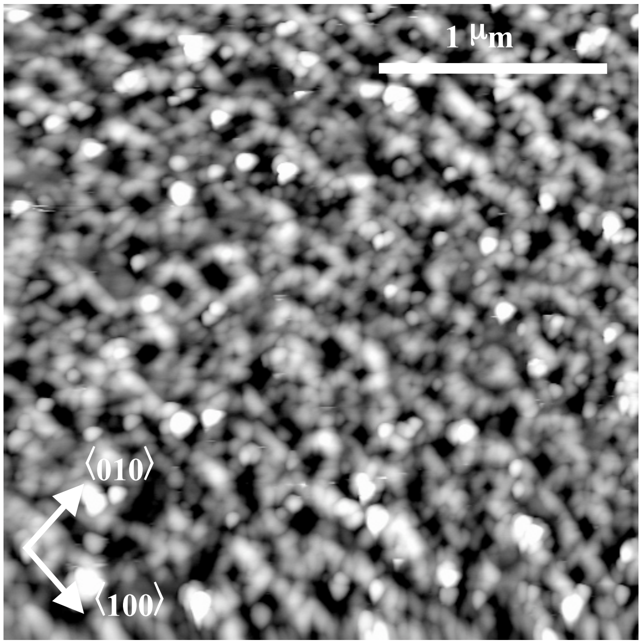

Figure 6.9—The {001} oriented rutile thin film after the silver reduction experiment.

6.2.4 Discussion

6.2.4.1 Effect of Measurement Technique

In general, the dimensions of the silver islands on the surfaces of the films are overestimated because of their small sizes. The overestimation of size is worse for islands with steeper sides because the side of the probe contacts the particle before the probe's tip does, causing the tip to lift prematurely. This creates the appearance of a larger, rounded island. The effects could differ slightly from film to film and probably had the least effect on the silver islands on the {010} oriented thin film because of the small slopes of their sides.

On the {001} orientated thin film, the amount of silver was more difficult to measure because of the surface morphology. It is possible that silver reduced preferentially on the intersections between the {011} facets, causing them to appear rounded in the AFM images, but not producing easily recognizable particles. Because it is difficult to tell the difference between images taken by a sharp tip on a rounded surface and images taken by a dull tip on a sharply faceted surface, it is impossible to tell whether silver exists at any or all of the facet intersections. Therefore, it is possible that the amount of silver on the {001} oriented thin film was underestimated compared with the other two films.

6.2.4.2 Comparison to Polycrystalline Results

At first glance, the surfaces of the rutile thin films after the photoreduction of silver appear different from the surfaces of the crystallites discussed in Chapter 5. The heights and diameters of the silver deposits on the thin films were smaller than the heights and diameters of the silver deposits on the crystallites, and the number of deposits on the {011} and {001} oriented thin films would have characterized them as having intermediate activity. We believe that the main reason for these discrepancies in spite of the longer exposure times is that the thin film experiments at CMU were conducted under a much weaker source of UV radiation, a tungsten fiber-optic light, than were the experiments at DuPont. In addition, the number of non-planar features, such as scratches and voids, that can act as nucleation sites is much smaller on the thin films than on the polycrystals.

Another discrepancy is the high photochemical activity of the {001} oriented thin film. We know from the polycrystalline results that the {011} surface is active, and we know that the {001} oriented thin film surface is composed of {011} facets. The quantum yield results also tell us that the {001} oriented thin film is more active than the {011} oriented thin film. One possibility is that the active sites for the photoreduction of silver is on the edges between {011} facets. This possibility was discussed in §5.4 and is consistent with the polycrystalline results. The second possibility, also discussed in §5.4, is that the number of active sites is dependent on the area of the {011} facets. Because of the morphology of the {001} oriented thin film, the surface area of {011} facets on the {001} oriented thin film is greater than the surface area of {011} facets on the {011} oriented thin films. However, the photochemical activity of the {001} oriented thin films was 3.5 times greater than the activity of the {011} oriented thin films, according to the change in optical density measurements shown in Table 6.1, while the area of {011} facets on the {001} oriented thin film is only approximately twice that of the {011} oriented thin film. Therefore, the difference in the area of the {011} facets cannot fully explain the difference in photochemical activity between the two films. This adds support to the hypothesis that the intersections between {011} facets play a role in the large photochemical activity of the {001} oriented thin film.

One final difference between the thin films and the polycrystals that should be discussed is the difference in surface defect populations and impurity levels. Because the growth temperatures of the thin films are lower than the processing temperatures of the polycrystals, the thin films are probably more highly oxidized than the polycrystals. The thin films also have a much lower surface impurity concentration than the polycrystals. If either the oxygen vacancy concentration or the impurity concentration played a large role in determining the anisotropy of rutile's photochemistry, the results from the thin films would be noticeably different than the results from the polycrystals. However, the qualitative results are similar. Although the quantum yield of the inactive {010} oriented thin film is higher than the quantum yields of crystallites with orientations near {010}, the overall trends in photochemical activity with surface structure remain the same, allowing us to meaningfully compare the results from the thin films to the results from the polycrystals.

So overall, the thin film results support the polycrystalline results. The two thin films with predominantly {011} facets—the {011} and {001}—reduced an order of magnitude more silver than the {010} oriented thin film, supporting the conclusion that the {011} is necessary for high photocatalytic activity on rutile. However, the higher photochemical activity of the {001} oriented thin film cannot be explained by the increase in the area of {011} facets, adding support to the hypothesis that the active sites for at least one photochemical reaction are on the intersections between {011} facets.

6.3 References

[1] P. Morris Hotsenpiller, J. Bolt, W. Farneth, J. Lowekamp, and G. Rohrer, *J. Phys. Chem. B* **102** (1998) 3216.
[2] P. Morris Hotsenpiller, A. Roshko, J. Lowekamp, and G. Rohrer, *J. Crystal Growth* **174** (1997) 424.
[3] L. Firment, *Surf. Sci.* **116** (1982) 205.
[4] M. Ramamoorthy, D. Vanderbilt, and R. King-Smith, *Phys. Rev. B* **49** (1994) 16721.
[5] P. Morris Hotsenpiller, G. Wilson, A. Roshko, J. Rothman, and G. Rohrer, *J. Crystal Growth* **166** (1996) 779.

Chapter 7

Summary, Conclusions and Future Work

7.1 Effect of Rutile Surface Structure on Photoactivity

The research in this thesis has led to a description of how the surface structure of rutile affects its ability to photoreduce silver ions in solution. This was accomplished through two complementary experiments. The first measured the amount of silver photoreduced by a wide range of irrational orientations on thermally faceted rutile polycrystals, and the second measured the amount of silver photoreduced by several low-index rutile thin films. The primary conclusion drawn from these experiments is that the high photochemical activity of rutile is due primarily to the presence of {011} facets.

In accomplishing our primary goal, we created orientation stability figures for rutile at 1273 K and 1473 K, seen in Figures 4.4 and 4.12, and calculated the surface energies of the stable surfaces. The {011} surface has the highest stability, followed by the {110}surface.

7.2 Conclusions

7.2.1 Orientation Stability Figures

AFM and EBSD were used to identify the orientations of the stable facets on the surfaces of more than 200 crystallites. The identities of the stable surfaces at 1473 K and 1273 K are summarized in two orientation stability figures, repeated here as Figures 7.1

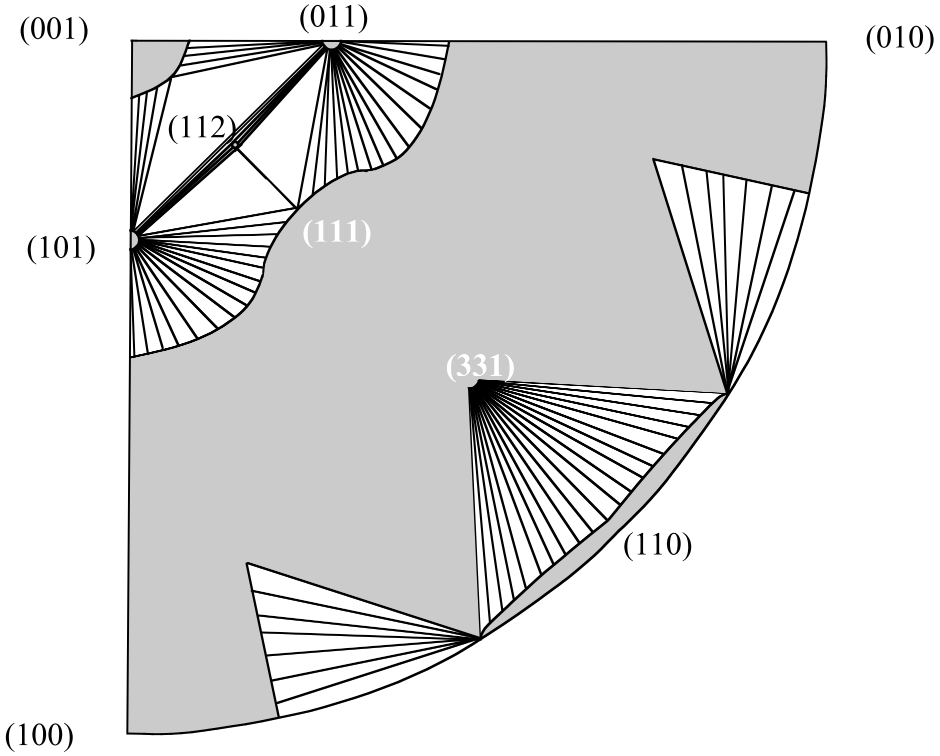

Figure 7.1—The orientation stability figure at 1473 K.

and 7.2. One feature of note on both figures is the appearance of {001} facets, long thought to be unstable with respect to faceting at high temperatures [1, 2, 3]. Also of interest is the appearance of {112} facets. This is in contrast to previous work, which found that the {114} [1, 2] or the {124} [3] is stable at high temperatures.

7.2.2 High stability of {011} and {110}

The relative surface energies of the stable facets were calculated using an equation derived from the Herring equation [4] and are reprinted here as Table 7.1. The results indicate that {011} is the most stable orientation at 1273 K and 1473 K followed by {110}. This is in contradiction to commonly held beliefs that {110} is the most stable orientation of rutile due to the higher average coordination of its surface titanium ions.

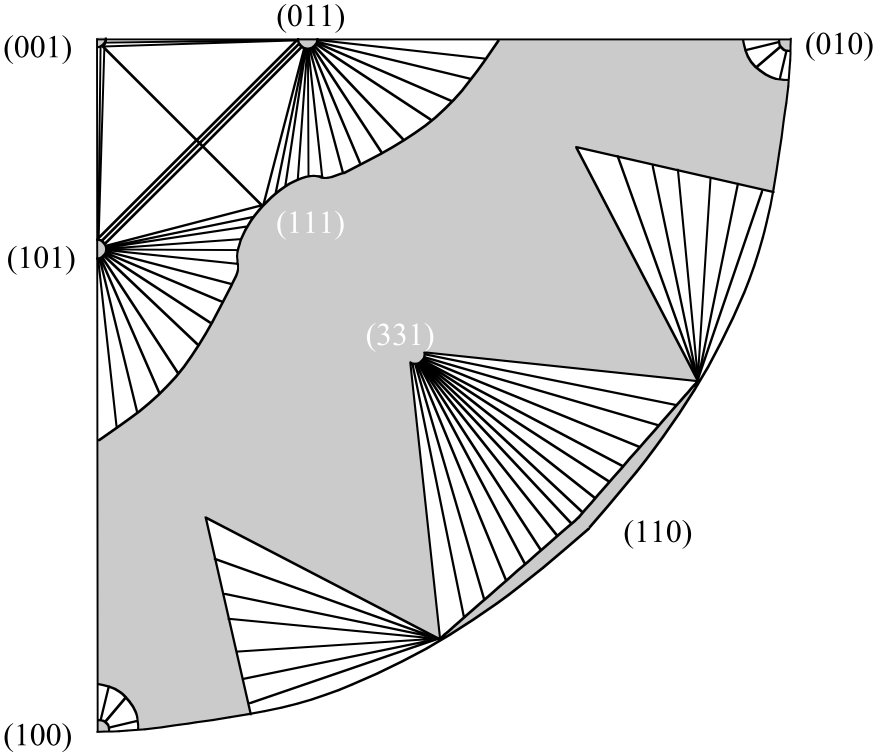

Figure 7.2—The orientation stability figure at 1273 K.

Table 7.1: Surface Energies

	1473 K		**1273 K**	
	relative energy	**number of measurements**	**relative energy**	**number of measurements**
{011}	1	N/A	1	N/A
region A	1.10±0.03	19	1.09±0.02	14
stable region around {001}	1.10±0.03	12	1.13±0.02	21
I/{112}	1.07±0.02	8	not stable	N/A
stable region around {110}	1.05±0.05	4	1.05±0.05	7
stable region around {010}	in region A	N/A	1.09±0.03	3

7.2.3 Effects of Temperature on Surface Stability

As the temperature decreases, the stable shape of rutile becomes more sharply faceted, so a smaller percentage of orientation space is stable with respect to faceting at 1273 K than at 1473 K. As the temperature decreases, entropy plays a smaller role in determining the minimum energy surface morphology. This increased faceting as temperature decreases is most evident with the faceting of the {001} oriented thin films grown at 998 K into {011} facets.

7.2.4 High Photochemical Activity of {011}

The photochemical activity of rutile is strongly dependent on the presence of {011} facets on the surface and not on anisotropic bulk processes. The polycrystalline results leave open the possibility that the photochemical activity depends on special sites on the {011} surface, on the intersections between {011} and neighboring facets, or on both surface features, while the thin film results suggest that the active sites for one or both photochemical reactions are on the intersections between {011} facets. Assuming unreconstructed surfaces, one possible reason for enhanced photo-oxidation on the {011} surface is the increased distance between neighboring titanium ions. The 20% increase in distance may allow for a more efficient use of all titanium ions as adsorption sites for water or hydroxyl ions because of a reduction in the electrostatic and steric interactions between water or hydroxyl groups on neighboring titanium ions. The polycrystalline results may be influenced by the greater presence of impurities on the surfaces of the inactive crystallites.

7.2.5 The Ideal Photocatalyst Microstructure

As stated in the introduction, this work was motivated by the desire to define the ideal, highly photoactive microstructure for rutile, which is demonstrated by the {001} oriented thin films. Both the area of the {011} facets and the number of intersections between {011} facets on the {001} oriented thin films are high. No crystallite surface on the polycrystal was composed of the fine scale faceting on the {001} oriented thin films that led to the high number of {011} intersections. However, surfaces with orientations lying between (011) and (101) on the orientation stability figure in Figure 7.2 are composed of only {011} facets, maximizing the number of active sites if they are on the {011} surface. If orientations near the middle of this region were chosen, it is possible that shorter annealing times would result in surfaces that are fully faceted into {011} facets but have a finer facet structure with more {011} facet intersections, leading to a higher photochemical activity if the active sites are on the intersections between {011} facets.

7.3 Future Work

7.3.1 Creating Ideal Microstructures

As mentioned previously, the {001} oriented thin films demonstrate the ideal microstructure for high photochemical activity, but the thermal annealing conditions we chose did not result in similar microstructures on the polycrystals. It may be possible to obtain this microstructure by annealing crystallites oriented near {001} at 998 K, the growth temperature of the films. If the faceting behavior under ambient pressure is similar to the surface formed while growing in near-vacuum, a microstructure similar to that of the {001} oriented thin films will result, possibly leading to higher photochemical activity. In addition, if this microstructure is achievable, its photochemical activity could be compared to that of surfaces annealed at higher temperatures that are composed of the {011} facets but fewer intersections. This could provide an answer to the question of whether the active sites are on the {011} facets or the intersections between {011} facets.

7.3.2 Verification of {112}

As discussed in §4.1, the orientation labeled I in Figure 4.4a is closer to {112} than to {114}, {113}, or {124}. However, the difference between the orientation labeled I and {112}, 6±2°, is slightly larger than the error associated with our methods, approximately 5°. Although we did not see flat surfaces near the orientation labeled I, the 6±2° difference in the orientation between I and {112} could be due to a region around {112} that is stable with respect to faceting. If this were the case, we would measure orientations along the line that defines the stability of the unfaceted region around {112}. The facet labeled I could also be due to stable regions around {114} or {124} that extend 15° or 10° away from the appropriate low-index plane, respectively.

Only 9 crystallites were examined with facets that were clearly identifiable as having orientation I. More data are required to verify which of the previous possibilities is the correct one. To get these data, EBSD can be used to identify crystallites with orientations near I. AFM can then be used to identify the facets on the surface. With enough data, it should be clear whether orientation I represents a single, complex facet or the stability limits of another, low-index facet.

7.3.3 Kinetics of Faceting

As discussed in §4.1, all surfaces did not completely in the time-scale of the thermal annealing. A series of experiments that annealed a polished polycrystal for increasing amounts of time would allow us to ensure that the surface was composed of its equilibrium facets. Since little is known about the mechanisms by which the facets coarsen, the kinetic data from such a study would be valuable for the formulation of a realistic model.

7.3.4 Examination of Surfaces Vicinal to {011}

We observed no flat or vicinal surfaces near {011} even though our definition of a flat surface seemed to indicate that these vicinal surfaces should exist. The lack of vicinal surfaces made it impossible to determine if the high photochemical activity of surfaces with {011} facets is due to the facets themselves or the intersections between the {011} facets and facets with neighboring orientations.

Vicinal surfaces could be created by examining an {011} oriented rutile single crystal surface and then introducing steps by polishing the surface at a slight angle to {011}. After thermally annealing the surface, the number of steps or the height of the steps would increase as the misorientation between {011}and the surface normal increases. The morphology of these surfaces could be studied as they evolved with annealing time, providing us with surface diffusion rates, and the photochemical activity could be studied as a function of facet width for surfaces with similar fractional areas of {011} facets, answering the question of where the active sites are.

7.3.5 Thin Film Growth on Polycrystalline Rutile

The photochemical activity of the high-purity, rutile thin films was examined to confirm that the photochemical anisotropy of the polycrystals was not due solely to the presence of impurities. However, we could not rule out the influence of impurities completely. If we could grow a rutile thin film using the methods outlined in §3.1 on a randomly textured, thermally annealed rutile polycrystal, we could create surfaces with the purity of the thin films and the orientation distribution of the polycrystals. However, because of the different growth rates along different directions and the lower thin film growth temperatures, the facet structure would change, resembling that of a growth surface at 998 K. The photochemical activity could be tested on the pure rutile surfaces, eliminating the effects of impurities on the photochemical activity over a wide range of orientations.

7.4 References

[1] L. Firment, *Surf. Sci.* **149** (1982) 205.
[2] G. Poirier, B. Hance, and J. White, *J. Vac. Sci. Technol.* **10** (1992) 6.
[3] L. Wang, J. Liu, and J. Cowley, *Surf. Sci.* **302** (1994) 141.
[4] C. Herring *in* "Structure and Properties of Solid Surfaces", (Gomer and Smith, Eds.), p5, Chicago University Press, Chicago (1953).

Appendix A

Determining Facet Slope with Linear Regression

Using the following equation for a plane (Eq. A.1),

$$z = mx + py + q \tag{A.1}$$

multiple linear regression can be used to calculate m, p, and q. In multiple linear regression, the square of the residual, or the difference between the predicted value and the experimental value, is minimized. In equation form (Eq. A.2),

$$R^2 = \sum (z - z_{pred})^2 \tag{A.2}$$

where z is the experimentally measured value of the height and z_{pred} is the predicted value of the height using the equation for the plane.

Equation A.3 is derived by substituting Equation A.1 into Equation A.2,

$$R^2 = \sum (z - mx - py - q)^2 \tag{A.3}$$

The next step to determining the slope of the plane is to minimize R^2 with respect to a and b by taking the appropriate derivatives and setting them equal to zero.

$$\frac{\partial R^2}{\partial m} = -2\sum_i x_i(z_i - mx_i - py_i - q) = -2\sum_i (x_i z_i) + 2m\sum_i (x_i^2) + 2p\sum_i (x_i y_i) + 2q\sum_i (x_i) = 0 \tag{A.4}$$

$$\frac{\partial R^2}{\partial p} = -2\sum_i y_i(z_i - mx_i - py_i - q) = -2\sum_i (y_i z_i) + 2m\sum_i (x_i y_i) + 2p\sum_i (y_i^2) + 2q\sum_i (y_i) = 0 \tag{A.5}$$

The next step is to define a geometry for solving the problem. In the AFM, the distance between data points in the x- and y-directions is constant and equal to the distance along which the scan is taken divided by the resolution, or number of pixels

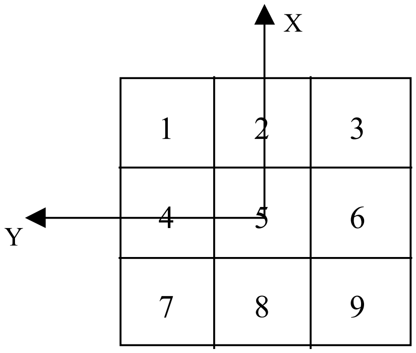

Figure A.1—The geometry chosen to calculate the slope of a facet. The slope is calculated for the center point of the grid, labeled 5.

across the image. Because the images are square, the distance between data points in the x-direction is equal to the distance between the data points in the y-direction.

The geometry chosen is a square grid with a side length of three pixels, shown in Figure A.1. By defining the step size in the x- and y-direction to be *S*, the sums in Equations A.4 and A.5 reduce to

$$\sum_{i=1}^{9} x_i^2 = S^2 + S^2 + S^2 + 0 + 0 + 0 + (-S)^2 + (-S)^2 + (-S)^2 = 6S^2 \tag{A.6}$$

$$\sum_{i=1}^{9} x_i y_i = (S)(S) + (S)(0) + (S)(-S) + (0)(S) + (0)(0) + (0)(-S) + (-S)(S) + (-S)(0) + (-S)(-S) = 0 \tag{A.7}$$

$$\sum_{i=1}^{9} x_i = S + S + S + 0 + 0 + 0 + (-S) + (-S) + (-S) = 0 \tag{A.8}$$

$$\sum_{i=1}^{9} y_i^2 = S^2 + 0 + (-S)^2 + S^2 + 0 + (-S)^2 + S^2 + 0 + (-S)^2 = 6S^2 \tag{A.9}$$

$$\sum_{i=1}^{9} y_i = S + 0 + (-S) + S + 0 + (-S) + S + 0 + (-S) = 0 \tag{A.10}$$

The coefficients *m* and *p* are solved for by inserting these sums back into Equations A.4 and A.5 (Eq. A.11 and A.12).

$$m = \frac{\sum_{i=1}^{9} x_i z_i}{6S^2} \tag{A.11}$$

$$p = \frac{\sum_{i=1}^{9} y_i z_i}{6S^2} \tag{A.12}$$

Appendix B

Java Program to Identify Orientations and Calculate Areas

B.1 ViewResults.java

ViewResults.java contains the main program that accepts command-line arguments and sets up the connections between the objects used to complete the calculations. The program assumes tetragonal symmetry. Method and class names are in bold print and comments are italicized.

```
package jpbl.slopes;

import java.awt.*;

public class ViewResults extends Frame {
  ImageViewer baseImage;
  ImageViewer slopeImage;
  ShowSlopeInfo showInfo;
  VariableShading slider;

  Slopes slopeData;


  public ViewResults(String fileName, double phi1, double capPhi, double phi2){
    super("AFM Image Analysis");
    setLocation(20,30);

    slopeData = new Slopes(fileName, phi1 * Math.PI / 180.0,
      capPhi * Math.PI / 180.0, phi2 * Math.PI / 180.0);

    baseImage = new ImageViewer(slopeData.rawData.createImage(), this);
    slopeImage = new ImageViewer(slopeData.createSlopeImage(),this);
    slider = new VariableShading(slopeData);
    showInfo = new ShowSlopeInfo(slopeData, baseImage, slopeImage);

    // The slope data listens to the slider to adjust greyscale when asked
    slider.addAdjustmentListener(slopeData);

    // each image listens to the others mouse events to move the crosshair
```

```
    baseImage.addMouseMotionListener(slopeImage);
    slopeImage.addMouseMotionListener(baseImage);
    baseImage.addMouseListener(slopeImage);
    slopeImage.addMouseListener(baseImage);

    // showinfo listens to both images mouse events to display the data
    baseImage.addMouseMotionListener(showInfo);
    slopeImage.addMouseMotionListener(showInfo);
    baseImage.addMouseListener(showInfo);
    slopeImage.addMouseListener(showInfo);

    GridBagLayout layout = new GridBagLayout();
    GridBagConstraints constraints = new GridBagConstraints();

    setLayout(layout);

    constraints.fill = GridBagConstraints.NONE;
    constraints.weightx = 1;
    constraints.weighty = 1;
    constraints.gridwidth = 1;

    layout.setConstraints(baseImage, constraints);
    add(baseImage);

    layout.setConstraints(slopeImage, constraints);
    add(slopeImage);

    constraints.fill = GridBagConstraints.VERTICAL;
    constraints.gridwidth = GridBagConstraints.REMAINDER;
    layout.setConstraints(slider, constraints);
    add(slider);

    constraints.fill = GridBagConstraints.HORIZONTAL;
    layout.setConstraints(showInfo, constraints);
    add(showInfo);

    pack();
    show();

  }


  public static void main(String argv[]){
    ViewResults me = new ViewResults(argv[0],
      Double.valueOf(argv[1]).doubleValue(),
      Double.valueOf(argv[2]).doubleValue(),
      Double.valueOf(argv[3]).doubleValue());
  }
}
```

B.2 CrossHatch.java

CrossHatch.java draws the crosshatch on the picture that marks where the mouse is.

```
package jpbl.slopes;
```

```
import java.awt.*;

public class CrossHatch extends Component{
  int x,y;

  boolean visible;

  public static final int Dim=2;


  public CrossHatch(){
    x=y=0;
    visible=false;
  }


  public void moveTo(int toX, int toY){
    visible = true;
    x=toX;
    y=toY;

    paint(getGraphics());
  }


  public void paint(Graphics g){
    if(visible){
      g.setColor(Color.red);
      g.drawLine(x-Dim,y,x+Dim,y);
      g.drawLine(x,y-Dim,x,y+Dim);
    }
  }
}
```

B.3 DialogPrompt.java

DialogPrompt.java creates a box that asks for the identifying facet name and returns the input to the calling program.

```
package jpbl.slopes;

import java.awt.*;
import java.awt.event.*;

/**
  * prompt user for single line input (filename, info, etc)
  */
public class DialogPrompt extends Dialog
implements ActionListener {
  public static final int ENTER = 1;
  public static final int CANCEL = 2;

  private Button enter=null, cancel=null;

  private TextField text=null;
```

```
  public int response;
  public String entered;

  private boolean haveResponse = false;


  public DialogPrompt(Frame parent, String title, String defText){
    super(parent, title, true);

    text = new TextField(defText, 30);
    add("North", text);

    enter = new Button("Enter");
    enter.addActionListener(this);
    enter.setActionCommand("Enter");
    add("West", enter);

    cancel = new Button("Cancel");
    cancel.addActionListener(this);
    cancel.setActionCommand("Cancel");
    add("East", cancel);

    pack();
  }


  public synchronized void doPrompt(){
    show();
  }


  public void actionPerformed(ActionEvent e){
    if(e.getActionCommand().equals("Enter")){
      response = ENTER;
      entered = text.getText();
    }
    else{
      response = CANCEL;
      entered = "";
    }

    setVisible(false);
  }
}
```

B.4 ImageCanvas.java

ImageCanvas.java is responsible for displaying images on the monitor. It is a modification of a class provided by Sun Microsystems.

```
package jpbl.slopes;

/* modified by lowekamp for ease of use */

/*
 * Copyright (c) 1995-1997 Sun Microsystems, Inc. All Rights Reserved.
```

```
 *
 * Permission to use, copy, modify, and distribute this software
 * and its documentation for NON-COMMERCIAL purposes and without
 * fee is hereby granted provided that this copyright notice
 * appears in all copies. Please refer to the file "copyright.html"
 * for further important copyright and licensing information.
 *
 * SUN MAKES NO REPRESENTATIONS OR WARRANTIES ABOUT THE SUITABILITY OF
 * THE SOFTWARE, EITHER EXPRESS OR IMPLIED, INCLUDING BUT NOT LIMITED
 * TO THE IMPLIED WARRANTIES OF MERCHANTABILITY, FITNESS FOR A
 * PARTICULAR PURPOSE, OR NON-INFRINGEMENT. SUN SHALL NOT BE LIABLE FOR
 * ANY DAMAGES SUFFERED BY LICENSEE AS A RESULT OF USING, MODIFYING OR
 * DISTRIBUTING THIS SOFTWARE OR ITS DERIVATIVES.
 */
/*
 * 1.1 version.
 */

import java.awt.*;
import java.applet.Applet;

class ImageCanvas extends Canvas {
  Container pappy;
  Image image;
  Dimension size;
  int w, h;
  boolean trueSizeKnown;
  MediaTracker tracker;


  public ImageCanvas(String filename, Container highestContainer){
    Toolkit toolkit = Toolkit.getDefaultToolkit();
    Image image = toolkit.getImage(filename);

    init(image, highestContainer);
  }


  public ImageCanvas(Image image, Container highestContainer) {
    init (image, highestContainer);
  }


  private void init (Image image, Container highestContainer) {
    if (image == null) {
      System.err.println("Canvas got invalid image object!");
      return;
    }

    this.image = image;
    this.pappy = highestContainer;

    tracker = new MediaTracker(this);
    tracker.addImage(image, 0);
    for(boolean isIn=false;!isIn;){
      try{
        tracker.waitForAll();
        isIn=true;
      }
      catch (java.lang.InterruptedException e){
      }
    }
```

```
    w = image.getWidth(null);
    h = image.getHeight(null);

    size = new Dimension(w,h);
  }


  public Dimension getPreferredSize() {
    return getMinimumSize();
  }


  public Dimension getMinimumSize() {
    return size;
  }


  public void paint (Graphics g) {
    if (image != null) {
      if (!trueSizeKnown) {
        int imageWidth = image.getWidth(this);
        int imageHeight = image.getHeight(this);

        if (tracker.checkAll(true)) {
          trueSizeKnown = true;
          if (tracker.isErrorAny()) {
            System.err.println("Error loading image: " + image);
          }
        }

        //Component-initiated resizing.
        if (((imageWidth > 0) && (w != imageWidth)) ||
            ((imageHeight > 0) && (h != imageHeight))) {
          w = imageWidth;
          h = imageHeight;
          size = new Dimension(w,h);
          setSize(w, h);
          pappy.validate();
        }
      }
    }

    g.drawImage(image, 0, 0, this);
    g.drawRect(0, 0, w - 1, h - 1);
  }
}
```

B.5 Normals.java

Normals.java stores triples of real numbers.

```
package jpbl.slopes;

public class Normals {
  double x1, x2, x3;
```

```
  public Normals() {
    x1 = 0;
    x2 = 0;
    x3 = 1;
  }


  public Normals(double x1, double x2, double x3) {

    this.x1 = x1;
    this.x2 = x2;
    this.x3 = x3;
  }
}
```

B.6 ReadHDF.java

ReadHDF.java converts *.hdf files created with Park ProScan version 1.5 (or previous) into image files and extracts necessary information from the *.hdf files, such as image size and height scaling factor.

```
package jpbl.slopes;

import java.io.*;

public class ReadHDF {
  short data[], max, min, DIM=512;
  double imageSize=0, zStep=0;
  BufferedInputStream HDFfile;
  String fileName;

  /**
    * each OFFSET parameter was determined with the PSI ProScan version 1.5
    * software.  The data format is HDF, but most of the info is in a
    * block of type UNKNOWN and appears to be raw data stuffed in by
    * Park.  hdp list -d will show the offsets of the major fields.
    * The image is listed as
    *    11     Scientific Data     702       2           0       16384
524288
    * and the PSI custom field is listed as
    *    19             Unknown   32777       2           0         928
202
    */

  private static final int Z_SCALE_OFFSET = 1042;
  private static final int XY_DIM_OFFSET = 994;
  private static final int MIN_OFFSET = 1054;
  private static final int DATA_OFFSET = 16384;

  // should be greater than the largest seek which will be done
  private static final int MARK_OFFSET_LIMIT = 20000;


  public ReadHDF(String fileName)
    throws java.io.IOException {
```

```
    this.fileName = fileName;

    // open file in here
    readDataFromFile();
  }


  public void readDataFromFile( )
    throws java.io.IOException {

      BufferedInputStream infile =
        new BufferedInputStream(new FileInputStream(fileName));

      System.err.println("skipped"+infile.skip(XY_DIM_OFFSET));
      imageSize = readFloat(infile);

      System.err.println("imageSize="+imageSize);

      infile.skip(Z_SCALE_OFFSET-XY_DIM_OFFSET-4);
      zStep = readFloat(infile);

      System.err.println("zStep="+zStep);

      infile.skip(MIN_OFFSET-Z_SCALE_OFFSET-4);
      min = readShort(infile);
      max = readShort(infile);

      System.err.println("max = "+max+" min="+min);

      infile.skip(DATA_OFFSET-MIN_OFFSET-4);

      // read in max, min, imageSize, zStep

      data = new short[DIM * DIM];

      // skip header in file
      for (int i = 0; i < data.length; i++) {
        data[i] = readShort(infile);
      }
  }


  public short readShort(InputStream in)
    throws java.io.IOException {
      short result;
      int a,b;

      a=in.read();
      b=in.read();

      result = (short)(a|(b<<8));

      return result;
  }


  public float readFloat(InputStream in)
    throws java.io.IOException {
      int intermediate;
      byte[] vals = new byte[4];

      in.read(vals);
```

```
      intermediate = (vals[0]&0x000000ff)|
        ((vals[1]<<8)&0x0000ff00)|
        ((vals[2]<<16)&0x00ff0000)|
        ((vals[3]<<24)&0xff000000);

      return Float.intBitsToFloat(intermediate);
  }


  public short dataMin() {
    short minimum = 32767;

    for (int i = 0; i < data.length; i++) {
      if (minimum > data[i]) {
        minimum = data[i];
      }
    }

    return minimum;
  }


  public java.awt.Image createImage() {
    int pixels[] = new int[DIM*DIM];
    int addTo = (int)(-min);
    double multfact = 255.0 / (double)((int)max + addTo);
    double grey;
    int thisPix;
    for (int r = DIM - 1; r >= 0; r--) {
      for (int c = 0; c < DIM; c++) {
        grey = (double)((int)data[r * DIM + c] + addTo) * multfact;
        if (grey < 0.0) {
          grey = 0.0;
        } else if (grey > 255.0) {
          grey = 255.0;
        }
        thisPix = (int)grey;

        // opaque, equal RGB for grey
        pixels[(DIM-1-r)*DIM+c] = 255<<24|(thisPix<<16)|(thisPix<<8)|thisPix;
      }
    }

    return java.awt.Toolkit.getDefaultToolkit().createImage
      (new java.awt.image.MemoryImageSource(DIM, DIM, pixels, 0, DIM));
  }
}
```

B.7 ShowSlopeInfo.java

ShowSlopeInfo.java is responsible for following the mouse, detecting right and left mouseclicks, displaying information at the bottom of the image about the slope of the surface, and returning information about the Euler angles of facets or the area of facets to the screen or a file.

```
package jpbl.slopes;

import java.awt.*;
import java.awt.event.MouseMotionListener;
import java.awt.event.MouseListener;
import java.awt.event.MouseEvent;

public class ShowSlopeInfo extends TextArea
implements MouseMotionListener, MouseListener {
  private Slopes slopeInfo;
  private ImageViewer image, slopeImage;

  private java.text.DecimalFormat slopeFormat =
    new java.text.DecimalFormat("0.00000");

  private boolean frozen = false;


  public ShowSlopeInfo(Slopes slopeInfo, ImageViewer image, ImageViewer
slopeImage){
    super("",4,100,TextArea.SCROLLBARS_NONE);

    this.slopeInfo = slopeInfo;
    this.image = image;
    this.slopeImage = slopeImage;

    setEditable(false);
  }


  public void mouseMoved(MouseEvent e) {
    int x = e.getX();
    int y = e.getY();
    if(!frozen)
      setText("("+x+" , "+(slopeInfo.rawData.DIM - y - 1)+")\n"+
        slopeFormat.format(slopeInfo.slopes3D[slopeInfo.rawData.DIM -
                                               y - 1][x].x1)+" / "+
        slopeFormat.format(slopeInfo.slopes3D[slopeInfo.rawData.DIM -
                                               y - 1][x].x2)+" / "+
        slopeFormat.format(slopeInfo.slopes3D[slopeInfo.rawData.DIM -
                                               y - 1][x].x3));
  }


  public void mouseDragged(MouseEvent e) {
    mouseMoved(e);
  }


  public void mousePressed(MouseEvent e) {}


  public void mouseReleased(MouseEvent e) {}


  public void mouseEntered(MouseEvent e) {
    mouseMoved(e);
  }


  public void mouseExited(MouseEvent e) {
    if(!frozen)
      setText("");
```

```
  }


  public void mouseClicked(MouseEvent e) {
    DialogPrompt prompt;
    int x= e.getX();
    int y= e.getY();
    mouseMoved(e);
    System.err.println("Mouse is "+(e.getModifiers()&e.BUTTON3_MASK));
    frozen = true;
    prompt = new DialogPrompt((Frame)getParent(), "Facet index", "");

    // x and y are relative to each image viewer, but we might need
    // to translate if clicked in the righthand viewer
    Component originatingWindow = e.getComponent();
    Point target = originatingWindow.getLocationOnScreen();
    target.translate(x+15,y+15);

    prompt.setLocation(target);
    image.freeze();
    slopeImage.freeze();

    prompt.doPrompt();

    frozen = false;
    image.unfreeze();
    slopeImage.unfreeze();
    if(prompt.response == prompt.ENTER) {
      if ((e.getModifiers()&e.BUTTON3_MASK) == 0) {
        Normals aveSlope =
          slopeInfo.calculateAverageSlope(slopeInfo.rawData.DIM - y - 1, x);

        Normals facetEulerAngles = slopeInfo.calculateFacetEulerAngles
          (aveSlope);
        Normals planeHKL = slopeInfo.calculatePlaneCoeff(aveSlope);

        System.out.println
          (slopeInfo.rawData.fileName+": (facet "+ prompt.entered +")\n "+
            "Euler angles: (" + slopeFormat.format(facetEulerAngles.x1) +
            ", " + slopeFormat.format(facetEulerAngles.x2) + ", " +
            slopeFormat.format(facetEulerAngles.x3) + ")\n" +
            "(h k l): (" + slopeFormat.format(planeHKL.x1) + "  " +
            slopeFormat.format(planeHKL.x2) + "  " +
            slopeFormat.format(planeHKL.x3) + ")\n");
      }
      else {
        System.out.println
          (slopeInfo.rawData.fileName+": (facet "+ prompt.entered +")\n "+
          "facet area = " +
          slopeInfo.calculateFacetArea(slopeInfo.rawData.DIM - y - 1, x));
      }
    }
  }
}
```

B.8 Slopes.java

Slopes.java calculates the slope image, the slopes of the facet with respect to the surface, the Euler angles and (hkl) of any selected point on the surface, and the total area of the surface composed of a chosen facet.

```
package jpbl.slopes;

import java.io.*;

public class Slopes implements java.awt.event.AdjustmentListener {
  ReadHDF rawData;
  Normals slopes3D[][];
  double rotMatrix[][];
  int pixels[]; // keep around for animation
  private static final int redColor = 0xffff0000; // red

  java.awt.image.MemoryImageSource source;


  public Slopes(String fileName, double phi1, double capPhi, double phi2) {

    rotMatrix = createRotationMatrix(phi1, capPhi, phi2);

    try {
      rawData = new ReadHDF(fileName);
    }
    catch (IOException e){
      System.err.println("unable to open hdf file "+fileName+":"+e);
      System.exit(1);
    }

    // x1 is x dir. cos, x2 is y dir. cos, x3 is z dir. cos
    slopes3D = new Normals[rawData.DIM][rawData.DIM];

    calculateSlopes();
  }


  public double[][] calculateHeights(){
    double heights[][] = new double[rawData.DIM][rawData.DIM];
    int addTo = -(int)rawData.dataMin();
    int DIM = rawData.DIM;

    for (int r = 0; r < DIM; r++) {
      for (int c = 0; c < DIM; c++) {
        heights[r][c] = (double)((int)rawData.data[r * DIM + c] + addTo) *
          rawData.zStep;
      }
    }

  return heights;
  }


  public void calculateSlopes() {
    double heights[][];
    int DIM = rawData.DIM;
```

```
    double xyStep = rawData.imageSize / (double)DIM;
    double xcoeff, ycoeff, length;

    heights = calculateHeights();

    for (int c = 0; c < DIM; c++) {
      slopes3D[0][c] = new Normals();
      slopes3D[DIM - 1][c] = new Normals();
    }

    for (int r = 1; r < DIM - 1; r++) {
      for (int c = 0; c < DIM; c++) {
        if (c != 0 && c != DIM - 1) {
          xcoeff = 0;
          ycoeff = 0;
          for (int i = -1; i <= 1; i++) {
            for (int j = -1; j <= 1; j++) {
              xcoeff += (heights[r + i][c + j] * (double)j);
              ycoeff += (heights[r + i][c + j] * (double)i);
            }
          }
          xcoeff = xcoeff / (6.0 * xyStep);
          ycoeff = ycoeff / (6.0 * xyStep);
          length = Math.sqrt(xcoeff * xcoeff + ycoeff * ycoeff + 1.0);

          slopes3D[r][c] = new Normals(-xcoeff / length, -ycoeff / length,
                                 1.0 / length);
        } else {
          slopes3D[r][c] = new Normals();
        }
      }
    }
  }


  public double findMaxAngleWithSurface() {
    double max = -1.0;

    for(int r = 1; r < rawData.DIM - 1; r++){
      for (int c = 1; c < rawData.DIM - 1; c++) {
        if (slopes3D[r][c].x3 > max)
          max = slopes3D[r][c].x3;
      }
    }

    return max;
  }


  public double findMinAngleWithSurface() {
    double min = 1.0;

    for(int r = 1; r < rawData.DIM - 1; r++){
      for (int c = 1; c < rawData.DIM - 1; c++) {
        if (slopes3D[r][c].x3 < min)
          min = slopes3D[r][c].x3;
      }
    }

    return min;
  }
```

```
private void updateSlopeImage(double max, double min){
  double multfact, color;
  System.err.println("image with max,min="+max+","+min);
  if (pixels==null)
    pixels = new int[rawData.DIM*rawData.DIM];

  multfact = 255.0 / (max - min) / (max - min) / (max - min) / (max - min)
             / (max - min);

  // sets edges to white
  for (int c = 0; c < rawData.DIM; c++) {
    pixels[0 * rawData.DIM+c] = 255;
  }
  for (int r = rawData.DIM - 2; r > 0; r--) {
    for (int c = 0; c < rawData.DIM - 1; c++) {
      if (c == 0 || c == rawData.DIM - 1) {
        pixels[r*rawData.DIM+c] = 255;
      } else {           // color is skewed toward low slope range
        color = (slopes3D[r][c].x3 - min) * (slopes3D[r][c].x3 - min) *
          (slopes3D[r][c].x3 - min) * (slopes3D[r][c].x3 - min) *
          (slopes3D[r][c].x3 - min) * multfact;
        if (color < 0.0) {
          color = 0.0;
        } else if (color > 255.0) {
          color = 255.0;
        }
        pixels[(rawData.DIM - r - 1)*rawData.DIM+c] = (int)color;
      }
    }
  }
  for (int c = 0; c < rawData.DIM; c++) {
    pixels[(rawData.DIM - 1)*rawData.DIM+c] = 255;
  }

  for(int i=0;i<rawData.DIM*rawData.DIM;i++) {
    pixels[i]= 255<<24|(pixels[i]<<16)|(pixels[i]<<8)|pixels[i];
  }

}


public java.awt.Image createSlopeImage() {
  double max, min;

  max = findMaxAngleWithSurface();
  min = findMinAngleWithSurface();

  updateSlopeImage(max,min);

  source = new java.awt.image.MemoryImageSource(rawData.DIM, rawData.DIM,
                                               pixels, 0, rawData.DIM);
  source.setAnimated(true);

  // may want to flag as animated if planning changes
  return java.awt.Toolkit.getDefaultToolkit().createImage(source);
}

public void adjustmentValueChanged(java.awt.event.AdjustmentEvent e){
  double min = ((double)e.getValue())/VariableShading.TICKS;
  double max = findMaxAngleWithSurface();

  updateSlopeImage(max, min);
  source.newPixels();
```

```
}


public double calculateFacetArea(int index1, int index2) {
  Normals DirCos = slopes3D[index1][index2];
  int numPixels = 0;

  for (int r = 1; r < rawData.DIM - 1; r++) {
    for (int c = 1; c < rawData.DIM - 1; c++) {
      if (slopes3D[r][c].x1 * DirCos.x1 > 0 &&
          slopes3D[r][c].x2 * DirCos.x2 > 0 &&
          Math.abs(slopes3D[r][c].x3 - DirCos.x3) < 0.05 &&
          DirCos.x3 - slopes3D[r][c].x3 < 0.1) {
        numPixels += (1 / slopes3D[r][c].x3);
        pixels[(rawData.DIM - r - 1)*rawData.DIM+c] = (int)redColor;
      }
    }
  }

  source.newPixels();

  System.err.println("numPixels = "+numPixels);

  return ((double)numPixels / ((double)rawData.DIM * (double)rawData.DIM) *
          (rawData.imageSize * rawData.imageSize));
}


public Normals calculateFacetEulerAngles(Normals DirCos) {
  Normals facetEulerAngles;  // x1 is phi1, x2 is PHI, x3 is phi2
                             // phi1 (x1) cannot be calculated from normals
  Normals planeNormals;
  double a = 4.593, c = 2.959;   // lattice constants for rutile

  planeNormals = calculatePlaneCoeff(DirCos);

  facetEulerAngles = new Normals();

  facetEulerAngles.x2 = Math.acos(planeNormals.x3 / c);
  facetEulerAngles.x3 = Math.acos(planeNormals.x2 / a /
                        Math.sin(facetEulerAngles.x2));

  if (facetEulerAngles.x2 > Math.PI / 2) {
    facetEulerAngles.x2 = Math.PI - facetEulerAngles.x2;
  }
  if (facetEulerAngles.x3 > Math.PI / 2) {
    facetEulerAngles.x3 = facetEulerAngles.x3 - Math.PI / 2;
  }
  if (facetEulerAngles.x3 > Math.PI / 4) {
    facetEulerAngles.x3 = Math.PI / 2 - facetEulerAngles.x3;
  }

  facetEulerAngles.x2 = 180.0 * facetEulerAngles.x2 / Math.PI;
  facetEulerAngles.x3 = 180.0 * facetEulerAngles.x3 / Math.PI;

  return facetEulerAngles;
}


public Normals calculatePlaneCoeff(Normals DirCos) {
  Normals planeNormals;          // x1 is h, x2 is k, x3 is l
  double a = 4.593, c = 2.959;   // lattice constants for rutile
```

```
    planeNormals = new Normals();

    planeNormals.x1 = Math.abs(rotMatrix[0][0] * DirCos.x2 - rotMatrix[0][1]
                               * DirCos.x1 + rotMatrix[0][2] * DirCos.x3) * a;
    planeNormals.x2 = Math.abs(rotMatrix[1][0] * DirCos.x2 - rotMatrix[1][1]
                               * DirCos.x1 + rotMatrix[1][2] * DirCos.x3) * a;
    planeNormals.x3 = Math.abs(rotMatrix[2][0] * DirCos.x2 - rotMatrix[2][1]
                               * DirCos.x1 + rotMatrix[2][2] * DirCos.x3) * c;

    return planeNormals;
  }


  public double[][] createRotationMatrix(double phi1, double capPhi, double
phi2) {
    double a[][] = new double [3][3];

    a[0][0] = Math.cos(phi1) * Math.cos(phi2) - Math.sin(phi1) * Math.sin(phi2)
*
              Math.cos(capPhi);
    a[0][1] = Math.sin(phi1) * Math.cos(phi2) + Math.cos(phi1) * Math.sin(phi2)
*
              Math.cos(capPhi);
    a[0][2] = Math.sin(phi2) * Math.sin(capPhi);
    a[1][0] = - Math.cos(phi1) * Math.sin(phi2) - Math.sin(phi1) *
              Math.cos(phi2) * Math.cos(capPhi);
    a[1][1] = - Math.sin(phi1) * Math.sin(phi2) + Math.cos(phi1) *
              Math.cos(phi2) * Math.cos(capPhi);
    a[1][2] = Math.cos(phi2) * Math.sin(capPhi);
    a[2][0] = Math.sin(phi1) * Math.sin(capPhi);
    a[2][1] = - Math.cos(phi1) * Math.sin(capPhi);
    a[2][2] = Math.cos(capPhi);

    return a;
  }


  public Normals calculateAverageSlope(int index1, int index2) {
    Normals aveSlope;
    double xSlope = 0, ySlope = 0, zSlope = 0;
    int count = 0;
    int size = 3, xLowerBound, xUpperBound, yLowerBound, yUpperBound;

    xLowerBound = index1 - size;
    xUpperBound = index1 + size;
    yLowerBound = index2 - size;
    yUpperBound = index2 + size;

    if (xLowerBound < 1) {
      xLowerBound = 1;
    }
    if (xUpperBound > rawData.DIM - 2) {
      xUpperBound = rawData.DIM - 2;
    }
    if (yLowerBound < 1) {
      yLowerBound = 1;
    }
    if (yUpperBound > rawData.DIM - 2) {
      yUpperBound = rawData.DIM - 2;
    }

    for (int i = xLowerBound; i <= xUpperBound; i++) {
      for (int j = yLowerBound; j <= yUpperBound; j++) {
```

```
        xSlope += slopes3D[i][j].x1;
        ySlope += slopes3D[i][j].x2;
        zSlope += slopes3D[i][j].x3;
        count++;
      }
    }

    aveSlope = new Normals(xSlope / (double)count, ySlope / (double)count,
                           zSlope / (double)count);

    return aveSlope;
  }
}
```

B.9 VariableShading.java

VariableShading.java allows the user to control the contrast of the image on the monitor.

```
package jpbl.slopes;

import java.awt.*;

public class VariableShading extends Scrollbar {

  public static final int TICKS = 150;


  public VariableShading(Slopes slopeInfo){
    super(Scrollbar.VERTICAL);

    setValues((int)(slopeInfo.findMinAngleWithSurface()*TICKS), 8, 0, TICKS);
  }
}
```